Fall 2016

Heavy rainfall and flooding associated with atmospheric rivers over the central United States

Munir Ahmad Nayak
University of Iowa

HEAVY RAINFALL AND FLOODING ASSOCIATED WITH ATMOSPHERIC RIVERS OVER THE CENTRAL UNITED STATES

by

Munir Ahmad Nayak

A thesis submitted in partial fulfillment
of the requirements for the Doctor of Philosophy
degree in Civil and Environmental Engineering in the
Graduate College of
The University of Iowa

December 2016

Thesis Supervisor: Associate Professor Gabriele Villarini

Graduate College
The University of Iowa
Iowa City, Iowa

CERTIFICATE OF APPROVAL

_____

PH.D. THESIS

_____

This is to certify that the Ph.D. thesis of

Munir Ahmad Nayak

has been approved by the Examining Committee for
the thesis requirement for the Doctor of Philosophy degree
in Civil and Environmental Engineering at the December 2016 graduation.

Thesis Committee: _____
Gabriele Villarini, Thesis Supervisor

_____
A Allen Bradley

_____
Kate Cowles

_____
Witold Krajewski

_____
Gabriel Vecchi

IN THE NAME OF ALLAH, THE MOST GRACIOUS, THE MOST MERCIFUL.

I dedicate this thesis

to my parents Ali Mohammad Nayak and Jameela Akhter, my sister Rifat Ali, my grandparents Dada Jee and Dadi Jee, my wife Masarat Nabi, my adorable daughter Aieshia bint Munir, and all my relatives.

I love you all!

By Al-'Asr(the time). Verily! Man is in loss, except for those who believe and do righteous good deeds, and recommend one another to the truth, and recommend one another to patience.

Allah (subhanahu wa ta'ala)
Al-Quran (103)

ACKNOWLEDGEMENTS

First of all, I would like to thank Almighty Allah (SAW) for everything He has bestowed on me, including the help to complete this thesis.

I would like to sincerely thank my advisor Professor Gabriele Villarini for his support during my Ph.D. degree. Besides teaching me so many important things related to my academic life, personal life and social life, he helped me in perhaps the most difficult time of my life. This was the time when my thesis was due soon, my wife and I were expecting our first baby, my parents did not get a US Visa to help us, my health was not good and I had to go for two procedures and frequent visits to hospital, in addition to some more personal issues—God, so much pain. During this time, with the help from Allah(SAW), and with Professor Villarini's advices and support to allow me to work from home to take care of my Ph.D. work and my wife, I kept on moving along, and here I am with my complete thesis right on time. From the deepest part of my heart, I thank you dear Professor Villarini, and I pray that you and your family have great life ahead.

I thank my wife Masarat Nabi for the comfort she has provided me in my difficult times, I want to thank her for being patient with me; I know that living with me is not easy, and you have done more than what one would expect from a good wife. I am seeing the world with an entirely new perspective, you have made my life so much more meaningful. I want to thank you my beloved for giving me the most adorable gift, my little Aieshia! Masarat, please hold on to me forever and do not give up on me ever.

I would like to thank my parents, Jameela Akhter and Ali Mohammad Nayak, and my little sister Rifat Ali for bearing without me during the years I have been separated from them. I wish the time comes soon when I meet you and stay with you forever.

I would like to thank Professor Kate Cowles for acting as my M.S. Statistics adviser. Professor Cowles, you are such a wonderful person, I wish everybody was like you. I thank Professor Witold Krajewski for helping me get into the Ph.D. program here at the University of Iowa. I thank my committee members for serving in my committee.

I want to thank IIHR-Hydroscience and Engineering, the University of Iowa, for providing me space and facilities for my Ph.D. work. I would also like to thank all the people who have reviewed my manuscript for publications.

This work was supported by the National Aeronautics and Space Administration (NASA) Headquarters under the NASA Earth and Space Science Fellowship Program, Grant NNX14AK78H. I would also like to thank R, Enthought Canopy, and Matlab teams, and the agencies that have provided all the data I used in this thesis.

Thank you all

ABSTRACT

Atmospheric rivers (ARs) are long and narrow river-like features in the lower troposphere that carry most of the atmospheric water vapor fluxes from the tropics to the midlatitudes. Because of the large amount of moisture transported by these storms, they can cause heavy rainfall and major flooding events, such as the Midwest floods of 1993 and 2008. The overarching theme of this thesis is to understand the impacts of ARs on extreme precipitation and floods over the central United States.

First, to improve the understanding of the mechanisms leading to the development of these storms, three ARs that happened during the summer of 2013 are studied in detail. The work provided insight into the synoptic conditions associated with these storms. Moreover, I found that the source of moisture for ARs over the central United States can be located both in the tropics and subtropics, and evaporation over land can also add water vapor along the AR trajectory.

To understand the characteristics of precipitation during these storms, I focused on a 12-year period and used different high spatial and temporal resolution remote sensing-based precipitation products. These analyses showed that most of the AR-related precipitation is located in a narrow region (approximately 150km) within the area where the strongest moisture transport occurs.

The analysis of multiple long-term atmospheric reanalysis products has led to the development of the climatology of ARs over the central United States. This climatology is used to understand the AR characteristics, their long-term impacts on annual precipitation, precipitation extremes, and flooding over the central United States. AR characteristics (e.g., frequency, duration) are generally robust across the different reanalysis products. These

storms exhibit a marked seasonality, with the largest activity in winter (more than ten ARs per season on average), and the lowest in summer (less than two ARs per season on average). Overall, ARs generally last less than three days, but exceptionally persistent ARs (more than six days) are also observed. In terms of their impacts on precipitation, AR-related precipitation is able to explain a large portion of the year-to-year variations in the total annual precipitation over the central United States. Moreover, 40% of the top 1% daily precipitation extremes are associated with ARs, and more than 70% of the annual instantaneous peak discharges and peaks-over-threshold floods are associated with these storms, in particular during winter and spring.

The relationship between the frequency of ARs and three prominent large-scale atmospheric modes [Pacific-North American (PNA) teleconnection, Artic Oscillation (AO), and North Atlantic Oscillation (NAO)] is investigated, and the results are used to statistically model the frequency of ARs at the seasonal scale. PNA and AO indices play a significant role in the winter season, when the AR frequency is the highest. Building on these insights, different spatio-temporal Bayesian hierarchical models are developed to describe the frequency of winter heavy precipitation events based on ARs and the large-scale atmospheric modes. The results suggest that over much of the central United States, PNA and AO can be helpful in describing the frequency of ARs in winter, which in turn can be useful to characterize the frequency of heavy rainfall events over the central United States.

Because of the large impacts that these storms have, their short-term predictability is examined by using outputs from five numerical weather prediction (NWP) models with a lead-time up to 15 days. While there are differences among the five NWP models, the

results show that the skill in forecasting the occurrence and location of ARs over the central United States decreases with increasing lead time, and the models have positive skills up to the seven-day lead time.

PUBLIC ABSTRACT

Atmospheric rivers (ARs) are long and narrow river-like features in the lower atmosphere that carry most of the water vapor from the tropical regions to the midlatitudes. Because of the large amount of moisture transported by these storms, they can cause heavy rainfall and major flooding events, such as the Midwest floods of 1993 and 2008. The overarching theme of this thesis is to understand the impacts of ARs on extreme precipitation and floods over the central United States.

ARs exhibit a marked seasonality, with the largest activity in winter and the lowest in summer. Overall, the duration of most ARs is less than three days, but exceptionally persistent ARs (more than six days) have been observed. Over the central United States, ARs contribute up to 30% of the average annual rainfall, and play an even larger role in terms of heavy rainfall and flooding: more than 40% of the heavy rainfall events and more than 70% of the flood events over the region are associated with ARs, in particular during winter and spring.

Furthermore, the results of this dissertation show that the frequency of ARs over the central United States, and the associated precipitation, are related to large-scale climate conditions, with the Pacific North American teleconnection pattern and the Artic Oscillation playing a significant role. By leveraging this physical insight, statistical models are developed to capture the connection between climate and ARs, paving the way to improved modeling and prediction of these storms and the associated impacts.

TABLE OF CONTENTS

LIST OF TABLES

LIST OF FIGURES

CHAPTER 1

INTRODUCTION

1.1 Atmospheric rivers

The balance of energy, moisture and momentum is an important feature that assists the earth in maintaining its natural climatic variability. This balance is retained through the transport of moisture, energy, and momentum from the equator to the poles, which occurs as a result of the equator-to-pole temperature gradient due to the differential heating of the earth by the sun. Newell et al. (1992) provided evidence that most of this transport takes place in narrow (width ~ 500km) and long (length > 1000km, depending on the region) river-like features in the lower troposphere. They also observed that four to five of these features are present in the atmosphere of both hemispheres on any given day. Newell and Zhu (1994) found that these features are prevalent in almost all the ocean basins, and can occur both in winter and summer. These features are estimated to be responsible for more than 90% of the meridional fluxes while occupying only 10% of the earth's circumference at a given latitude (Zhu and Newell 1998). Because of their long and narrow structure, and the fact that large water vapor fluxes occur with them, Zhu and Newell (1994) termed these features as atmospheric rivers (ARs).

Although the term *atmospheric river* was coined by Zhu and Newell (1994), previous key studies provide significant understanding of the structure and dynamics of features that could well be documented as ARs. For example, in describing the widespread precipitation systems in the midlatitudes, Browning (1986, 1990), Carlson (1980) and Harrold (1973) used the term warm *conveyor belt*—an elongated band of cloud transporting large quantities of heat, moisture and momentum. Other terms such as *cloud bursts* (McGuirk et al. 1987), *tropical-extratropical cloud bands* (Kuhnel 1989) and *Tropical Moisture Exports* (TME, Knippertz and Wernli 2010), which have strictly tropical origins, have also been used. In the development of the climatology of TMEs, Knippertz et al. (2013) found that 90% of ARs (i.e., features that do not require tropical moisture sources) affecting the west coast of the United States during winters were connected to TMEs. The definitions used for these terms resemble the AR criteria set forth by several authors (e.g, Ralph et al. 2004;

Ralph et al. 2006; Neiman et al. 2008; Lavers et al. 2012). Before the advent of weather satellites, studies documenting features akin to ARs can be found in the references of Harrold (1973), McGuirk et al. (1987) and Kuhnel (1989). Although the exact genesis and dynamics of ARs is still the topic of research, some earlier studies (e.g., Harrold 1973; Browning 1986, 1990) and more recent ones (Bao et al. 2006; Ralph et al. 2006; Neiman et al. 2008) have provided significant contributions in laying out the general structure of these storms.

Generally, ARs are located parallel to and ahead of the surface cold front as part of low-level jet (LLJ) within the warm conveyor belt of extratropical cyclone systems (Browning and Pardoe 1973; Browning 1986; Ralph et al. 2004). Most of the high moisture content present in ARs is located within the first few kilometers from the surface, and is transported quickly by LLJ before being lifted up slantwise in the presence of denser cold front, or by other convection mechanisms (e.g., by orographic lifting). ARs have moisture sources in the tropics and subtropics, although extratropical sources, including the local convergence of moisture on landmasses, are not rare (Bao et al. 2006; Dacre et al. 2015). Over the central United States, ARs are observed frequently owing to the presence of extratropical cyclones and the southerly Great Plains low-level jet (GPLLJ). GPLLJs, originating from the Gulf of Mexico and the Caribbean, occur primarily in April–September (Bonner 1968; Mitchell et al. 1995; Higgins et al. 2000), with the highest frequency in August and September. Extratropical cyclones over the Atlantic, on the other hand, occur frequently in November–April due to increased meridional thermal gradient that leads to stronger baroclinic instability (or baroclinicity). The Gulf of Mexico and the Caribbean Sea are the primary sources of moisture for the central United States precipitation (Dirmeyer and Kinter 2010; Dirmeyer et al. 2014) and ARs (Dirmeyer and Kinter 2009), but in certain cases, moisture along ARs can also be advected from the eastern Pacific Ocean (Moore et al. 2012).

1.2 Impacts of ARs on water resources

Because of the presence of warm, moist air and strong winds, under suitable lifting mechanisms (e.g., orographic, frontal, convective, dynamic) ARs can lead to heavy rainfall and flood events. The extreme rainfall associated with ARs can result in fatalities,

widespread flooding and mudslides, and hundreds of millions of dollars in damages (http://www.esrl.noaa.gov/psd/atmrivers/events/). For this reason, in recent years there has been a growing body of literature linking ARs to heavy rainfall and flooding in the mid-latitudes. In this section, I review some studies that demonstrate the role ARs play in regulating available water and in shaping extreme hydrologic events in different regions of the globe, including the central United States.

The impact of ARs is felt widely around the world, including the western United States (Ralph et al. 2006), Europe (e.g., Lavers and Villarini 2013a), central United States (e.g., Lavers and Villarini 2013b) and South America (e.g., Viale and Nuñez 2011). A number of studies have focused on the impacts of ARs on the U.S. West Coast. Over this region during 1998–2005 period, Neiman et al. (2008) found that precipitation magnitudes in winter were twice as large in events that were associated with ARs compared to the storms that did not exhibit AR characteristics. In relating Snow Water Equivalent (SWE) to ARs, they also found that ARs generally increase SWE during winter and decrease it during spring. Over the 2004–2010 period, Guan et al. (2010) estimated that 20–30% of annual SWE was contributed by only a few ARs over the Sierra Nevada. Dettinger et al. (2011) showed that relatively few storms (mostly ARs) brought on average 20–50% of the California's precipitation during 1951–2008, highlighting the major role ARs have in California's water resources. They also showed that ARs contribute more than 50% to the annual streamflow in the coastal areas, and 34–54% as one moves further inland. Over the coastal areas of Northern California, Ralph et al. (2013) studied the effect of duration of ARs on precipitation totals and soil moisture, and found that the average-duration ARs (20-hour long) increase the soil moisture from 29% to 35% volumetric water content. The authors also estimated that the water vapor transport over the coastal mountains explained 74% and 61% of the variability in precipitation totals and streamflow in the region, respectively, between November 2004 and August 2010.

Recently, Lavers and Villarini (2015a) used data from 1979 to 2012 to estimate the fraction of precipitation associated with ARs over the United States and Europe. Their results showed a significant contribution from ARs to precipitation. In particular, the authors found that the fractional contribution to the average monthly precipitation reached more than 30% over certain parts the continental United States and Europe. They also

observed a marked seasonality in AR contribution, with the highest contribution in winter (DJF) and the lowest in summer (JJA); in December, the monthly fractional contributions at some locations were more than 50%. Steinschneider and Lall (2016) estimated the contribution of TMEs to annual and seasonal precipitation. TME-based precipitation was defined on the basis of changes in specific humidity along the tracks of TMEs. The authors showed that, depending on the location, TME-based precipitation accounts for 10% to 30% of the annual precipitation for the period 1979–2006, although higher contributions ranging from 30%–50% were observed in spring, for instance over the Ohio River basin. The seasonality of TME-based precipitation matched with what was observed in Lavers and Villarini (2015a). These results were corroborated by Steinschneider and Lall (2015b) who introduced Archetypical Analysis (AA) to compare the modes of variability of total precipitation and TME-based precipitation, both of which were obtained from a reanalysis product for the period 1979–2013. AA is similar to Empirical Orthogonal Functions (EOFs) but with additional advantages of better capturing the modes of variability of extreme events, such as heavy rainfall events often prevalent in TMEs. With AA, the spatial characteristics of the architypes of TME-based precipitation resembled well with those of the total precipitation, and the authors concluded that TMEs can be helpful in understanding the modes of precipitation variability over the central United States. These studies highlight the major role ARs play in the water availability in the form of precipitation over different regions.

In addition to total precipitation, many studies have linked ARs to extreme hydrologic events such as heavy precipitation events, floods, and droughts. Over the western United States, ARs have caused a number of damaging floods (Ralph et al. 2006; Neiman et al. 2008; Leung and Qian 2009; Dettinger et al. 2011; Neiman et al. 2011; Ralph and Dettinger 2012). Ralph et al. (2006) studied the impact of ARs on seven two- to three-day duration flood events that exceeded the monitor-stage at the Guerneville station on the Russian river in California from 1997 to 2005 and found that all the seven floods were caused by ARs. The authors concluded that these floods occurred because of heavy precipitation that resulted when the moisture-laden winds in ARs were lifted upslope in the mountainous region. Recent studies have demonstrated that ARs penetrate well beyond coastal areas and deep into continental regions. For example, Neiman et al. (2013) and Hughes et al. (2014)

show that ARs from the Pacific affect large areas from the U.S. West Coast to central Arizona, and the impacts in terms of precipitation are large, comparable to the ARs landfalling along the U.S. West Coast (Neiman et al. 2013). Rutz et al. (2015) provide a detailed description of ARs penetrating inland over the Western North America.

Many parts of Europe have also been widely affected by heavy precipitation and floods resulting from ARs (Stohl et al. 2008; Lavers et al. 2011; Lavers et al. 2012). Lavers et al. (2011) found that the ten largest winter floods in four British river basins over the 1970–2010 period occurred during the presence of ARs; they also pointed out that the smaller floods over the region had no major connection with ARs, indicating that ARs produce the most severe flooding events over the region. The authors also noted that ARs are critical in producing winter floods across the United Kingdom and Western Europe. Furthermore, (Lavers and Villarini 2013a) found that the impact of ARs over Europe can be felt as far inland as Germany and Poland.

Few studies have shown that ARs have significant impacts over the central United States as well (Moore et al. 2012; Nakamura et al. 2012; Lavers and Villarini 2013b). For instance, Lavers and Villarini (2013b) found that the upper tail of the annual flood peak distribution over a large portion of the central United States is mostly shaped by the floods occurring during the presence of ARs. They further noted that in their period of the study (1979–2011), the two most destructive flood events over the central United States—the great flood of 1993 (Kunkel et al. 1994) and the June 2008 flood in the Midwest (Dirmeyer and Kinter 2009; Budikova et al. 2010; Smith et al. 2013), both causing loss of billions of US dollars and claiming 48 and 24 lives (http://www.ncdc.noaa.gov/billions/), respectively—were preceded and accompanied by ARs. Lavers and Villarini (2013b) observed that more than 40% of the basins they studied had more than half of their annual maximum (AM) floods associated with ARs. About 60% of the 1105 river basins inspected had more than five out of the highest ten floods occurring during the presence of ARs. Recently, detailed analyses were performed by Moore et al. (2012) for the flood of May 2010 in Nashville and by Smith and Baeck (2015) for the flood of spring 1927 over the central United States. In these cases, heavy floods resulted following the high water vapor transport that occurred in ARs from the Gulf of Mexico into the central United States, and, given the definition of ARs, the expected extratropical cyclonic nature of precipitation

system was evident. The impact of mid-latitudinal cyclones over the central United States has also been noted by Villarini and Smith (2010). From the literature reviewed above, it is evident that ARs are critical agents in generating floods across many areas in the mid-latitudes, including the central United States.

Other than being responsible for producing deadly floods, ARs have been found to be a substantial source of water to the water resources. For example, Guan et al. (2010) estimated that ARs contributed 30–40% of the yearly seasonal SWE in Sierra Nevada, California over the 2004–2010 period. Dettinger et al. (2011) estimated that 20–50% of the total precipitation and streamflow in the state of California comes from ARs, making them an important source of soil moisture (Ralph et al. 2013). Lavers and Villarini (2015a) found that ARs contribute 20–30% of all the precipitation in Europe, western United States and over many parts of the central United States during the study period of 1979–2012. The importance of ARs is furthermore corroborated by their significant role in terminating droughts. Dettinger (2013) found that 60–74% of the droughts in the Pacific Northwest (Washington and Oregon) and 33–40% of the persistent droughts in California from 1950 to 2010 ended because of the precipitation from AR events.

1.3 Objectives and structure of thesis

Because of the major societal and economic impacts associated with these storms as described in this chapter, the overall objective of my thesis is to understand how ARs affect the precipitation and flooding over the central United States. Here is the structure of my thesis:

- In Chapter 2, I provide detailed analyses of three AR events that developed over and affected the central United States during the spring of 2013. I use these three storms as case study to understand the general physical mechanisms and synoptic settings responsible for the rainfall during ARs over the central United States.
- Chapter 3 focuses on the characterization of the rainfall associated with ARs over the central United States. Results are based on rainfall estimates from different remote sensing products, and allow the identification of regions within ARs in which most of the precipitation takes place.

- The results in Chapter 4 are based on a suite of reanalysis products and provide a long term perspective on the impacts of ARs on precipitation and flooding. Moreover, I also provide insights on the major climate processes driving the occurrence of ARs over the central United States.
- Chapter 5 builds on the physical insights on the climate processes from the previous chapter to develop a Bayesian hierarchical model to predict the frequency of extreme rainfall events across the central United States during the cold season.
- Chapter 7 examines the skill in short-term (from six hours to 2 weeks) forecasting the occurrence of AR events based on five state-of-the art Numerical Weather Prediction (NWP) models.
- Chapter 8 summarizes the main findings of my work and concludes it.

CHAPTER 2

ATMOSPHERIC RIVERS OVER THE CENTRAL UNITED STATES: ANALYSES DURING THE IFLOODS CAMPAIGN (SPRING 2013)[1]

The National Aeronautics and Space Administration (NASA) launched a field measurement campaign called Iowa Flood Studies (IFloodS) during April-June 2013 in eastern Iowa in collaboration with the Iowa Flood Center (IFC) at the University of Iowa. The goal of this field campaign was to evaluate satellite estimates of rainfall and other hydrometeorological quantities, particularly from the Ku/Ka radar similar to the one carried on board of the Global Precipitation Measurement (GPM; Hou et al. 2013) core satellite. The IFloodS campaign was set up to provide high quality satellite rainfall estimates that could help understand the physical characteristics including microphysics and vertical structure of rainfall during the period. This has the potential to help understand flooding mechanisms and to improve hydrologic modelling that ultimately could be used to improve the spatio-temporal predictions of floods.

This chapter aims at providing a synoptic and mesoscale analysis of the ARs that were present during some of the rainfall events during the IFloodS period, and thereby complements the IFloodS campaign objectives. Overall six intense rainfall events (24-h return period larger than 50 years) occurred during the IFloodS period in eastern Iowa, some of them causing flash floods in many parts of the region (e.g., 17 April flash flood in Iowa City, and May 30 flood in Des Moines). Because of these high rainfall amounts and potential strong link between ARs and heavy rainfall over the central United States, it is reasonable to assume that some of the heavy rainfall events during IFloodS may have been associated with ARs. In this regard, this chapter aims to answer the following questions:

1. What is the AR contribution to the total rainfall during the IFloodS period?
2. What are the physical mechanisms responsible for heavy rainfall during this period?

[1] Chapter adopted from Nayak, M. A., G. Villarini, and A. A. Bradley, 2016: Atmospheric rivers and rainfall during NASA's Iowa Flood Studies (IFloodS) Campaign. Journal of Hydrometeorology, 17, 257-271, doi: http://dx.doi.org/10.1175/JHM-D-14-0185.1

3. What are the characteristics (e.g., relationship between the strength of the AR and rainfall, distribution around AR's major axis, latitudinal and diurnal dependence) of rainfall during AR events in IFloodS?

2.1 Data and Methods

The first step is the identification of ARs during the IFloodS period (10 April–15 June 2013). Many previous studies employed column integrated water vapor (IWV) to identify ARs (see e.g., Ralph et al. 2006; Dettinger et al. 2011); here I use integrated vapor transport (IVT) to identify these events because it was found to better capture major AR features (for example, strong water vapor transport, narrow and elongated structure) than IWV (Lavers and Villarini 2015a). Moreover, IVT was also found to be more strongly related to rainfall during AR events (Rutz et al. 2014; Lavers and Villarini 2015a, 2015b). IVT magnitude ($kgm^{-1}s^{-1}$) is calculated from specific humidity and wind speed in the atmosphere as follows:

$$IVT = \sqrt{\left(\frac{1}{g}\int_{1000}^{300} qu\,dp\right)^2 + \left(\frac{1}{g}\int_{1000}^{300} qv\,dp\right)^2} \qquad 2.1$$

Here, q, u, and v are specific humidity ($kgkg^{-1}$), zonal and meridional wind components (ms^{-1}), respectively; g is the acceleration due to gravity (equal to $9.81ms^{-2}$), and p is pressure. I estimated IVT using a numerical approximation of the integrals with layer-averaged q, u, and v from the NASA's Modern-Era Retrospective Analysis for Research and Applications (MERRA, Rienecker et al. 2011) dataset for the period from 10 April to 15 June 2013 for pressure levels from 1000hPa to 300hPa. MERRA provides data with six-hour temporal resolution, 0.5º × 0.667º horizontal grid resolution and at 72 vertical levels from the surface to 0.01hPa. I used 28 vertical levels from surface to 300hPa.

To identify ARs using IVT, I used the methodology developed by Lavers and Villarini (2013b) with minor adjustments. In the first step, starting at 40ºN latitude, I determine the maximum IVT value between 85ºW to 100ºW. If the maximum is above a pre-specified threshold, the longitude of the maximum value is recorded, and the next latitude to south, i.e., 39.5ºN, is evaluated. The threshold used here is $550kgm^{-1}s^{-1}$ which is approximately the 85th percentile threshold by Lavers and Villarini (2013b) for the month of May over the central United States. At 39.5ºN, the maximum IVT value is identified. If its location

is within one grid point either to the east or to the west of the longitude of the location at 40ºN, I continue searching southward. This displacement condition is to enforce spatial continuity in the AR. If all the points from 40ºN to 30.5ºN have maximum IVT values exceeding the threshold and if they satisfy the displacement condition, then I consider this an AR step. The same procedure is repeated from south to north to confirm the correct latitude-longitude of the maximum IVTs. I refer to AR major axis as the collection of points with the maximum IVT values exceeding the threshold from 40ºN to 30.5ºN. Most of the AR time steps had the same major axis whether one starts from 40ºN or 30.5ºN to north, but four out of 17 AR time steps had differences due to the existence of secondary maxima. In each of these cases, I selected the AR major axis by visual examination of the IVT maps. The visual examination to select AR major axes and additional search from south to north were the two modifications that are made to the methodology by Lavers and Villarini (2013b). The 40ºN latitude is chosen to make sure that ARs travel deep into the central United States, and a length from 40ºN to 30.5ºN (approximately 950km) is chosen as minimum length requirement. A total of 17 six-hourly AR time steps are identified as ARs. The 17 AR steps make up three persistent (duration of more than 18 hours) ARs, two with six time steps (one from 0600UTC April 10 to 1200UTC April 11, and another from 0000UTC April 18 to 0600UTC April 19), and one with five (from 1200UTC May 29 to 1200UTC May 30).

The contribution of ARs to the total rainfall during IFloodS is estimated based on precipitation product Stage IV prepared at National Centers for Environmental Prediction (NCEP, Lin and Mitchell 2005). The data have a fine spatial resolution of approximately 4km × 4km and is available at 1 hour temporal resolution. The total rainfall and the contribution from ARs from Stage IV is compared and evaluated with respect to the NOAA CPC's Unified gage-based daily dataset (Higgins et al. 2000) which I use as the reference dataset. It is based on rain gage measurements from a number of networks and has a spatial resolution of 0.25º. Once the AR major axis is identified, I define rainfall associated with ARs as the rainfall within a 2 decimal-degree buffer (~200km) during the time periods 1200UTC April 10–1200UTC April 11, 1200UTC April 17–1200UTC April 19, and 1200UTC May 29–1200UTC May 31.

2.2 Physical mechanisms responsible for rainfall during ARs

Figure 2.1a shows the accumulated rainfall during the study period based on the CPC dataset, while Figures 2.1b and c show the AR contributions. This was a very wet period, with some of the largest rainfall accumulations over the 1948–2013 period. Figure 2.1d shows the rank of rainfall amount during this period as compared to the 66-year record from 1948–2013. Most of the regions in the central United States received anomalously high rainfall amounts (i.e., ranked in the top-5 wettest seasons) leading to flooding over the study area. ARs account more than 50% of the total rainfall in isolated areas as far north as Iowa and Illinois, to as far south as Oklahoma and Arkansas (Figure 2.1c). These results, and the ones in the next sections, provide empirical evidence that ARs are agents for heavy rainfall and flooding over the central United States.

The three ARs detected during IFloodS were associated with high rainfall amounts over much of the central United States. Figure 2.2 shows the rainfall maps during the ARs (3 hours before the first time step of AR to 3 hours after the last time step). The rainfall fields in these maps can be compared with Figure 2.1a, suggesting that a substantial amount of rainfall during IFloodS was due to the three ARs. At some locations, about 30% of the IFloodS rainfall was during the presence of one AR. The first two ARs (Figure 2.2, panels a and b) have a rainfall pattern which can be related to the pattern of mesoscale rain bands observed in extratropical cyclones (McMurdie and Houze 2006; Houze 2014). MCSs resulted in high rainfall amounts over Kansas and northern Oklahoma during the third AR. Of the three ARs that developed over the central United States during the IFloodS campaign, the weather systems of two (0600UTC April 10 to 1200UTC April 11 and 0000UTC April 18 to 0600UTC April 19) were similar to each other both featuring an extratropical cyclone weather system. I first briefly describe the weather systems corresponding to these ARs. The weather system corresponding to the third AR is described later in this section. Figures 2.3 and 2.4 show snapshots of the weather systems at 1800UTC on 10th April and 1800UTC on 18th April, respectively. The two weather systems in Figures 2.3 and 2.4 are fairly similar, although the weather corresponding to Figure 2.4 seems more organized with a stronger and better defined cyclone than what is shown in Figure 2.3. For the purpose of conciseness, I only describe the weather system corresponding to the AR in Figure 2.4 (I refer to this as the18th April AR event).

Geopotential heights at 850hPa (contours in Figure 2.4a) and surface pressure (contours in Figure 2.4d) show the presence of a low pressure center near eastern Iowa. At 850hPa level, the slow-moving lee trough over much of the Great Plains and a subtropical ridge over the Atlantic near the East Coast of the United States maintained poleward advection of warm moist air from the Gulf of Mexico and south-eastern United States. At higher levels, an advancing shortwave trough and cutoff low can be seen at 500hPa (geopotential height contours in Figure 2.4c), affecting the surface low and steering it northeastward. However, as the cyclonic flow progresses, the location of the 500hPa cutoff low coincides with the location of the surface low pressure center (not shown here) indicating the mature phase of the system. This low pressure system is associated with a cyclonic circulation which is evident in the wind barbs in Figure 2.4b.

The steep gradient of equivalent potential temperature (contours in Figure 2.4b) over Iowa, Missouri and extending to Texas defines the position of the surface cold front that was present during this AR. In Figure 2.4b, winds to the east of the front have a strong southerly component, whereas the winds just to the west of the front have a prominent westerly component. The position of the AR (large IVT values in Figure 2.4c and large IWV values in Figure 2.4a) is marginally to the east of the cold front in the warm sector (color shaded regions in Figure 2.4a and Figure 2.4c). To the east of this front, the air is uniformly warm and moist, and a narrow band of ascent takes place (Figure 2.4b) associated with convective rainfall coincident with the surface cold front. Widespread heavy rainfall can be seen in the earlier period of AR (0000-0600UTC 18 April) along the warm front across most of the upper Midwest (not shown here). Similar to a typical AR and extratropical cyclone system, sinking of cold and dry air takes place behind the cold front (Carlson 1980; Browning 1997; Schultz 2001; Catto et al. 2009). This cold air is advected by winds that are directed equatorward and to the west of cold front.

As in a typical extratropical cyclone, with the progression of the baroclinic wave and its associated surface low pressure center and cold front intensified and propagated eastwards, the AR results in continuous heavy precipitation along its path. In Figure 2.4d, the narrow band of heavy rainfall along the cold front due to convection is persistent during all the AR's time steps. The circular structure of rainfall around the low pressure center over Iowa is related to the spiral ascent of warm moist air and descent of cold dry air that

results due to cyclonic flow in and around the low pressure system. In Figure 2.4e, the skew-T–log-P diagram near Little Rock, Arkansas at 1500UTC 18 April is provided. Near-saturated and unstable conditions prevailed in the above-freezing layer from surface to 620hPa with a convective available potential energy (CAPE) of 1055.9Jkg^{-1}. Precipitation occurred in the form of rainfall from surface to the higher levels as indicated by the high freezing level (~ 3.6km). Near-surface southerlies are advecting warm-moist air from the Gulf of Mexico northwards, suggesting a geostrophic flow. At lower levels, veering of these geostrophic winds (vertical shear of the geostrophic winds) from southerly to south-westerly is consistent with the thermal wind relationship. Aloft (~ 550–500hPa) the dry layer of absolute static stability shows the presence of a frontal zone in the upper levels. At higher levels (< 400hPa), strong westerly winds dominate and the atmosphere remains stable and unsaturated. The skew-T–log-P diagram of the AR on 1800UTC 10 April is shown in Figure 2.3e. The lower levels (~920–780hPa) are moist and unstable, with a high corresponding CAPE value of 2476.4Jkg^{-1}. The atmospheric conditions in this case are similar to the AR on 18th April; however, in this case, dry cap inversion occurs at a lower level (~ 700hPa as opposed to 500hPa).

The weather system corresponding to the third AR is shown in Figure 2.5. This AR was associated with a major tornado outbreak that began on 27th May in the U.S. Midwest, and intensified on 29th and 30th May. The AR was driven by the anticyclonic flow around the Bermuda High, bringing warm moist air from the Gulf of Mexico into the central United States. During the initial time steps of the AR on 29th May, scattered rainfall was observed over most of the U.S. Midwest. As a weak upper level disturbance approaches, a low pressure center formed near Nebraska. Large values of IVT and IWV magnitude (Figure 2.5a, c) are present over most of the central United States indicating the moist atmospheric conditions from the Gulf of Mexico all the way to the northern parts of the central United States. At lower levels, southerly winds advected warm and moist air from the Gulf of Mexico (presented in the next section). A 500hPa trough was located over the Great Plains (Figure 2.5c) and with time, it intensified and propagated eastwards (temporal progression not shown here). The presence of the AR for an extended period of time provided continuous supply of warm-moist air supporting the development of rainfall events and thunderstorms. These conditions favored the formation and sustainability of MCSs (Houze

2014) over Kansas. Figure 2.5e shows the skew-T–log-P diagram for 1200UTC 30th May at Lamont, Oklahoma. The atmosphere in the lower levels is warm and at near-saturation, with winds exceeding 25ms^{-1}. The winds from the surface to 750hPa veer from the south to the southwest, as warm air advection further destabilizes the atmosphere. Strong vertical wind shear was associated with the severe weather which severely impacted many locations in the U.S. Midwest. In particular on 30th May, seven people were killed in Oklahoma due to tornadoes. Although a capping inversion exists at 1200UTC, the CAPE and convective inhibition (CIN) values are 1850Jkg^{-1} and -100Jkg^{-1}, which suggest a highly convective atmosphere. With daytime heating and sufficient lifting to trigger thunderstorms, deep convection resulted in intense rainfall at this and many other locations across the U. S. Midwest.

A Lagrangian trajectory analysis was performed for the three ARs to find out the sources of air parcels and their properties along the trajectories. For the ARs on 10th April and 18th April, parcels 1º × 1º apart in the box encompassing (86ºW, 37ºN and 90ºW, 40ºN) ending at 0600UTC 11 April and 1800UTC 18 April, respectively, were traced backwards. For the AR on 29th April, parcels in the box encompassing (93ºW, 37ºN and 97ºW, 40ºN) and ending at 1200UTC 30 May were traced. In all the three cases, the parcels were traced 72-h backwards at 1000 (~880), 4000 (~ 620) and 6000m AGL (~ 500hPa) levels. At these selected locations and times, IVT was relatively high with widespread concurrent rainfalls over the central United States. This analysis is similar to what was performed by Moore et al. (2012) and Neiman et al. (2014). In Figures 2.6a, b and c, 1000m AGL parcels mostly originated from central or eastern Gulf of Mexico; although, 84-h backward trajectory analysis (not shown here) shows that some parcels originated in the Caribbean Sea. Figures 2.6d, e and f, show the average pressure and mixing ratio of the parcels along the trajectories. In all the three cases, the parcels gradually descended while entering the southern United States. These parcels remained moist throughout their trajectories (with relative humidity 60–80% and mixing ratio 8–12gkg^{-1}). In the AR on 10th April low level trajectory, there is a substantial increase in mixing ratio; however, along the trajectory the parcels exhibited a decrease in mixing ratio and a weak subsidence before entering the box from which the parcels were traced. As the parcels enter into the box, after an initial increase in the mixing ratio, a strong decrease in the mixing ratio and a

moderate ascent and relative humidity about 80% suggest significant rainout. In the lower level parcels of ARs on 18th April and 30th April, significant amount of moisture is gained throughout the trajectory before entering the boxes. Similar to the AR on 10th April, decrease in mixing ratio, and ascent (with high relative humidity 80%) indicates substantial condensation and rainout. The majority of the parcels ending at 4000m AGL originated over the eastern Gulf of Mexico; however, in the ARs on 18th April and 30th May, some parcels advected from western Mexico and western United States. Most of the parcels ending at 6000m AGL originated from western Pacific and south-western United States. For the ARs on 10th April and 18 April, parcels ending at 4000 and 6000m AGL are dry (mixing ratio 2–4gkg^{-1} and relative humidity 25–35%) with mild descent before entering the southern and the central United States (1200UTC April 10–06UTC April 11 in Figure 2.6d and 0000UTC April 18 to 1800UTC April 18 in Figure 2.6e). Here, mixing ratio and relative humidity increase rather abruptly and parcels ascend over a small period of time suggestive of the lifting of moist air along the frontal boundary present during this AR. Similar conditions are observed in the AR on 30th May except that parcels are initially lifted around the middle point of their trajectory. This is perhaps due to the presence of high elevation mountains over the western United States. After this, the parcels descend gradually, only to be lifted again towards the end of the trajectories (0000UTC to 1200UTC May 30 in Figure 2.6f), where relative humidity increases to 60–80%. At this stage, there is also a large decrease in the mixing ratio, indicating rainout with lifting in the presence of the cold fronts associated with the ARs. In all the three cases, noting that the upper level trajectories were rather dry, most of the water vapor in the ARs originates from the northern tropics and subtropics over the Gulf of Mexico and the Caribbean, perhaps with some moisture generated over the terrestrial southern United States as depicted in Figure 2.6d, e. Moore et al. (2012) also identified the Caribbean Sea and Gulf of Mexico as the predominant sources of moisture in the May 2010 heavy rainfall that resulted in flooding over Kentucky and Tennessee.

The IFloodS rainfall mechanism for the first two ARs were similar to a major flooding event that happened on 1-2 May 2010 in Nashville, Tennessee, and surrounding areas. In this event, a low pressure system developed over the Northern Great Plains including eastern Canada (at the low pressure center, 850hPa geopotential height was 1230m; see

Figure 2.4b of Moore et al. (2012)). In essence, this event was caused by the persistent presence of AR conditions, high IVT and high IWV values, over the U.S. Midwest providing a constant source of precipitable water to the MCSs that developed over a couple of days (Moore et al. 2012). Although the low pressure systems during IFloodS ARs (e.g., 850hPa geopotential height of 1340m at the low pressure center on 18th April AR) were not as strong as the 2010 Tennessee event (corresponding height of about 1200m), the synoptic features, low pressure system over northern Great Plains and persistent AR conditions characterizing the first two ARs were similar to the 2010 Tennessee event. In their first MCS environment, Moore et al. (2012) observed two moist and unstable atmospheric layers with dry conditions aloft. In their second MCS, the lower layers were extremely moist with a convectively unstable layer just above 200hPa from the surface. In the ARs during IFloodS, moist unstable atmospheric conditions were observed only in the lower atmosphere, and in all the cases, the unstable layers were capped by a dry stable layer, followed by a dry conditionally stable layer. In essence, the mesoscale conditions that presented themselves during the ARs in IFloodS were similar to the one that resulted in heavy flooding in Tennessee in May 2010 described in Moore et al. (2012).

2.3 Rainfall Characteristics in ARs

The assessment of the distribution of rainfall around the AR major axis is an important objective of this chapter. For each of the 17 AR time steps, I divide the area around the AR major axis into three regions. The closest region is within one longitude-point from the major axis; (i.e., ±74km from the major axis). The second region covers a distance from 74 to 150km to the east and to the west of the major axis. The third and farthest region is from 150 to 370km to the east and west of the major axis. The average rainfall within these regions is calculated one hour before and one hour after each AR occurrence time. I also calculate the Pearson and Spearman correlation coefficients between IVT and rainfall in these three regions. This is done as I suspect more IVT may lead to more rainfall.

The relationship between rainfall amount and distance from the AR major axis is shown in Figure 2.7. In these panels, Spearman and Pearson correlation coefficients between IVT and rainfall are also plotted. The highest rainfall is observed in the region closest to the AR major axis, and then it decreases as one moves further away. Hence, most of the rainfall

occurs within about 100km of the AR major axis. This is likely due to higher IVT (water vapor transport) in this region, which in the presence of unstable conditions leads to condensation of water vapor and increased precipitation. The rainfall amounts tend to be the largest between 34.5°N and 37.5°N, with a less marked latitudinal dependence as one moves further away from the AR major axis.

The region closest to the AR major axis is also the one characterized by the strongest relationship between IVT and rainfall. For this region, the correlation coefficients are quite large, in excess of 0.60 and up to 0.70. These results suggest that there is a strong relationship between these two quantities, though its nature is not linear but monotonic (the values of the Spearman correlation coefficients are generally larger than the Pearson correlation coefficients). The strength of the relationship decreases in the regions farther away from the AR major axis (Figure 2.7b, c).

Another research question I shed light on in this chapter involves the examination of the effects of AR duration on rainfall. There are three persistent ARs, two of which last six time steps and one five time steps. For each time step of the three ARs, the areal average rainfall ±150km around the major axis is calculated. With this, I can plot the rainfall amounts corresponding to each AR time step, allowing the examination of the effects of AR duration on rainfall amounts (Figure 2.8). This figure suggests that the rainfall amounts are small at the early stage of the AR development. As the duration of the AR increases, so does the rainfall. The correlation coefficient between the AR time step and rainfall is 0.65. The rainfall associated with the AR on 18th April consistently increased with time, while with the other two ARs it increased in the middle timesteps followed by a decrease as the ARs subside. Although the dataset here is small, there is some indication of a positive relationship between rainfall and AR duration in the area close to AR major axis. A reasonable assumption is that this may be due the continuous supply of enhanced water vapor and unstable conditions sustaining mesoscale convective events (Houze 2014) leading to long periods of precipitation.

The final question I answer is related to the diurnal variation of AR occurrences and associated rainfall (Figure 2.9). This is accomplished by considering the closest region around the AR major axis. I calculate the total rainfall from all the ARs at the 6-hourly reanalysis times (i.e., 0000UTC, 0600UTC, 1200UTC, and 1800UTC). For example, at

0600UTC, five ARs are detected, and I calculate the total rainfall from all the five steps. I repeat this for the other three reanalysis time steps as well. Out of the 17 AR time steps, four occurred at 0000UTC, five occurred at 0600UTC, five occurred at 1200UTC, and three occurred at 1800UTC. Note that 0000UTC and 0600UTC correspond to evening (06p.m. local time) and mid-night hours (00a.m. local time), respectively, over the central United States. The relationship between IVT intensity and rainfall at each of the reanalysis times is also determined using Pearson and Spearman correlation coefficients. Figure 2.9 is similar to Figure 2.7, except that I focus on the four time steps and only on the region closest to the AR major axis. More rainfall is generally observed during the evening and mid-night hours (Figure 2.9a, b) compared to the rest of the day. This suggests that the diurnal cycle of the boundary layer, with its deep mixed layer in the afternoon initiating convection, followed by a stable nocturnal layer after sunset enhancing vapor transport, may be important factors for heavy rainfall associated with ARs (Arritt et al. 1997). Moreover, the rainfall amounts are higher at the mid-latitudinal regions than at other latitudes during evening and mid-night hours. The correlation between rainfall amounts and IVT intensity is not very strong at different times of the day. However, there is a strong relationship in the middle latitudes between 34ºN–37ºN during all times of the day, with the exception of the midnight hours (0600UTC) for which latitudes 37ºN–38ºN show a strong relationship. A strong monotonic relationship exists in the morning hours (1200UTC) in the lower to middle latitudes from 32ºN–36ºN.

2.4 Summary and Conclusions

The analyses in this chapter provide some basic characteristics of ARs and the associated rainfall during IFloodS. Over the central United States, the IFloodS period (65 days from 10 April to 15 June 2013) was characterized by several heavy rainfall events making it among the top five wettest 10 April–15 June periods over a record of 66 years. About 50% of the accumulated rainfall during the IFloodS campaign was caused by only three ARs, highlighting the significant impact the ARs can have on the rainfall over the central United States.

Even though the occurrence of ARs is associated with heavy rainfall, this is not necessarily the case everywhere within the central United States. For instance, there is a

region at the border between Iowa and Minnesota that received large rainfall amounts not related to ARs. More detailed analysis indicates that there were several days with daily rainfall accumulations smaller than 25mm (~1inch). The largest daily rainfall accumulations (in excess of 100mm) occurred on 20 May 2013. The examination of the IVT maps for that day indicates that there were regions with IVT values exceeding our threshold. However, the length requirement (IVT exceeding the threshold from 40ºN to 30.5ºN) was not satisfied. I visually inspected all the six-hourly IVT maps and confirmed that the AR-identification algorithm I presented was able to capture the elongated nature of these events. Lagrangian trajectory analysis depicted the tropical and subtropical sources of the water vapor present in ARs.

Intense rainfall was associated with the three ARs that occurred during IFloodS. Long and narrow regions of intense rainfall along the major axes were present in the first two ARs and were caused by the ascent of warm and moist air along the cold fronts present during these ARs. During these three ARs, intense rainfall was mostly convective in nature with warm and moist conditions sustained by the southerly advection in the ARs. During the third AR, unstable atmosphere with significant vertical wind shear (see in skew-T–log-P diagram in Figure 2.5e where lower level winds significantly change direction and magnitude from 950hPa–850hPa level) contributed to strong tornadoes over the U.S. Midwest during this AR.

Our analysis of the rainfall distribution for these events showed that much of the rainfall is located within about 100km from the AR major axis, with rainfall amounts decreasing for increasing distance. The rainfall showed some latitudinal dependency with more rainfall occurring at latitudes in the range 34.5ºN–37.5ºN. There is also strong positive monotonic relationship between IVT magnitude and rainfall amounts, especially in the region close to the AR major axis. In analyzing the effects of AR duration on rainfall, I find that there are small rainfall amounts in the early period of the AR lifetime, with substantial increases as these events develop and decreases as they come near to their end. Therefore, from an impact stand point, it would be useful to include a criterion of persistence in the AR detection algorithm as done, for instance, in Lavers and Villarini (2013b). Finally, I did not see any major diurnal dependence in the number of ARs; analysis

related to the diurnal variation of AR rainfall suggested that rainfall was larger in nocturnal ARs.

This chapter and the results from the high quality IFloodS data are useful for future studies on ARs and rainfall. As an example, given the presence of AR conditions during IFloodS and data from IFloodS, it is possible to model, or at least better understand, the horizontal and vertical structure of rainfall during ARs. One limitation of this analysis is related to the small number of events I analyzed. Here I focused on a period of 65 days which is not long enough to make any climatological claims regarding ARs and the associated rainfall. However, with this caveat in mind, this dataset does suggest possible relationships between AR and rainfall characteristics. In its essence, this chapter paves the way for a number of research questions that will be answered in the next chapters using longer records.

2.5 Figures Chapter 2

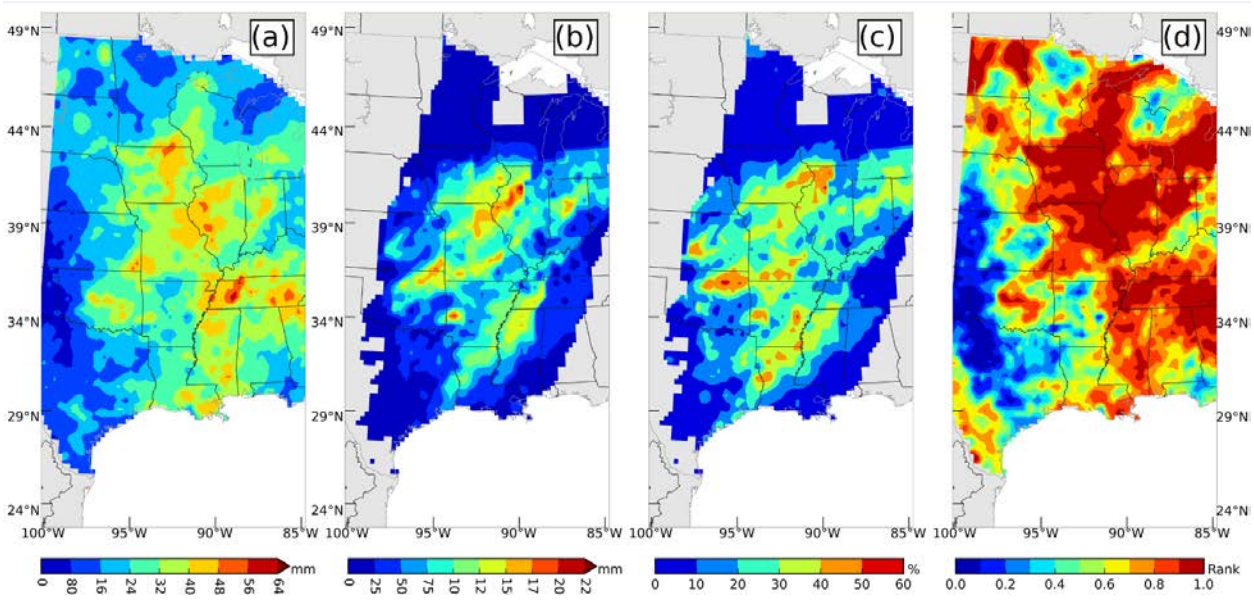

FIG. 2.1: Contribution of ARs to the total rainfall during the IFloodS campaign based on CPC rainfall data. a) Total rainfall (mm) over the period 10 April–15 June 2013. b) Rainfall (mm) associated with ARs. c) Percentage (%) of total rainfall associated with ARs d) Rank of the amount of rainfall during IFloodS period in a 66-year record ("1" means the wettest period, "0" the driest).

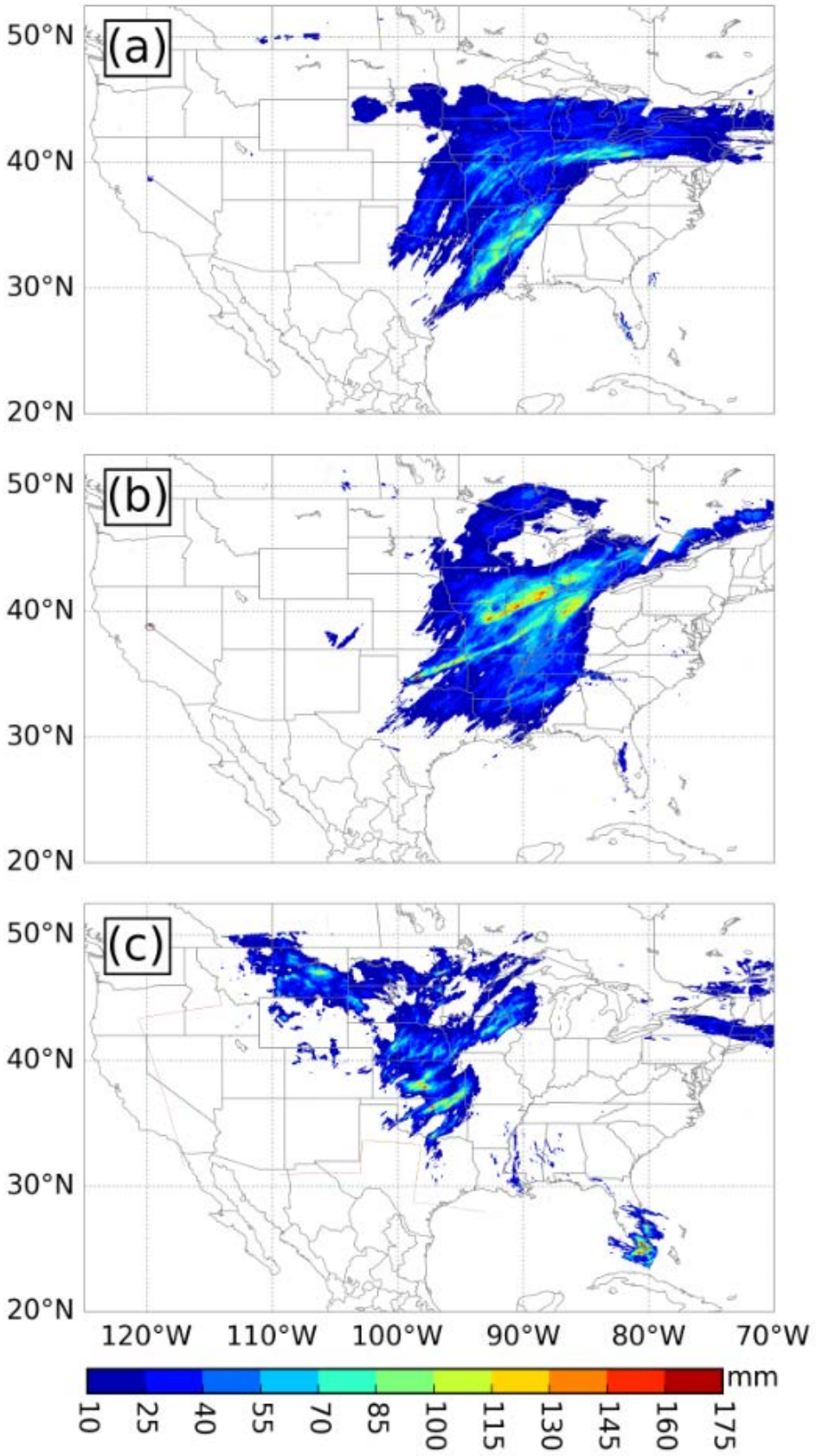
(a)
(b)
(c)
50°N
40°N
30°N
20°N
120°W
110°W
100°W
90°W
80°W
70°W
mm
10
25
40
55
70
85
100
115
130
145
160
175

FIG. 2.2: Accumulated rainfall during the three ARs during the IFloodS period based on Stage IV precipitation estimates for: a) 10th April AR b) 18th April AR c) 30th May AR. For these events, the accumulations are based on rainfall from three hours before the first AR time step to three hours after the last AR time step.

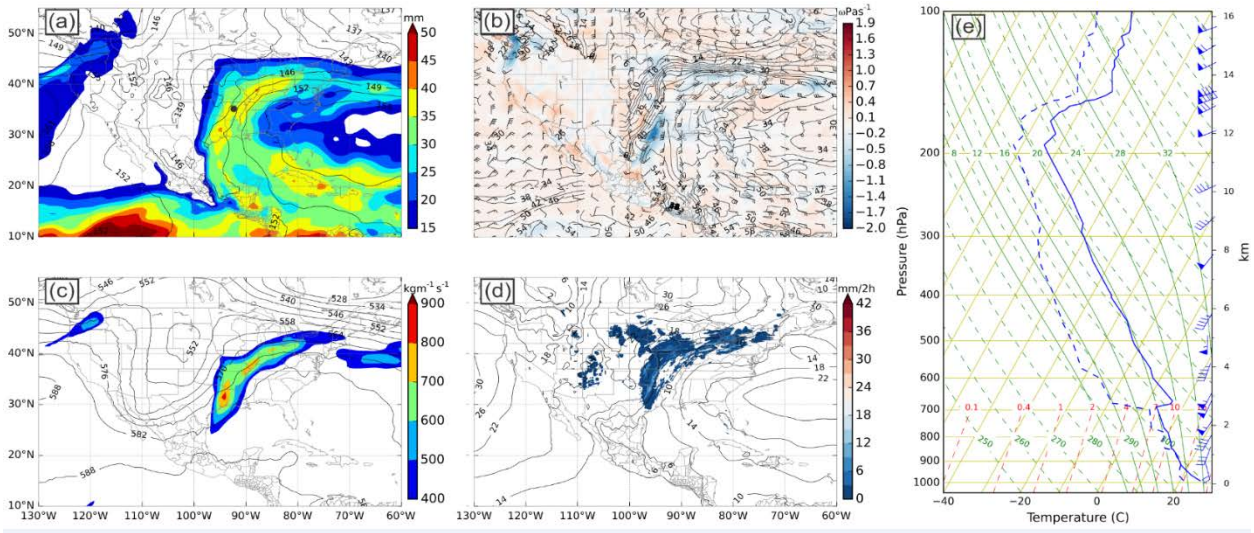

FIG. 2.3: Weather system prevalent at 1800UTC, 10 April, 2013. a) 850hPa geopotential height (contours at 3 dam interval), and IWV (mm) shaded contours. b) 850hPa vertical wind velocity (negative means ascent; based on ERA-Interim (Dee et al. 2011)) shaded, wind barbs (half barbs=2.5ms^{-1}, full barbs=5ms^{-1}, and pennant 25ms^{-1}), and contours of equivalent potential temperature θ_e (ºC) at 4ºC interval. c) 500hPa geopotential height (contours at 3dam interval), and IVT shaded in kgm^{-1}s^{-1}. d) Mean sea level pressure (slp-1000) contours at interval 40m, and two hour (1700 to 1800UTC and 1800 to 1900UTC, 10th April, 2013) Stage IV cumulative rainfall. e) Skew-T–log-p plot for 1800UTC 10th April 2013. Vertical temperature is plotted as solid line, dewpoint as dashed line and wind barbs are according to the convention used in Figure 2.3b. These results are for Little Rock, Arkansas (Station ID 72340) and were obtained from the University of Wyoming's sounding archive. The black filled circle in (a) shows the location of the station.

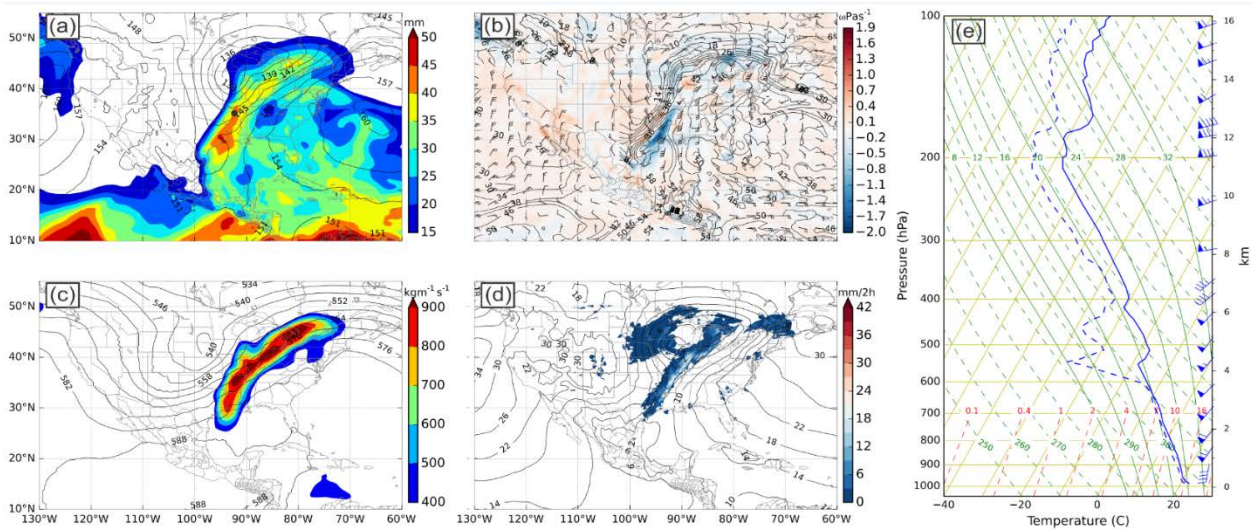

FIG. 2.4: Same as Fig. 2.3 but for 1800UTC, 18 April, 2013. Skew-T–log-p plot is for 1500UTC 18th April 2013.

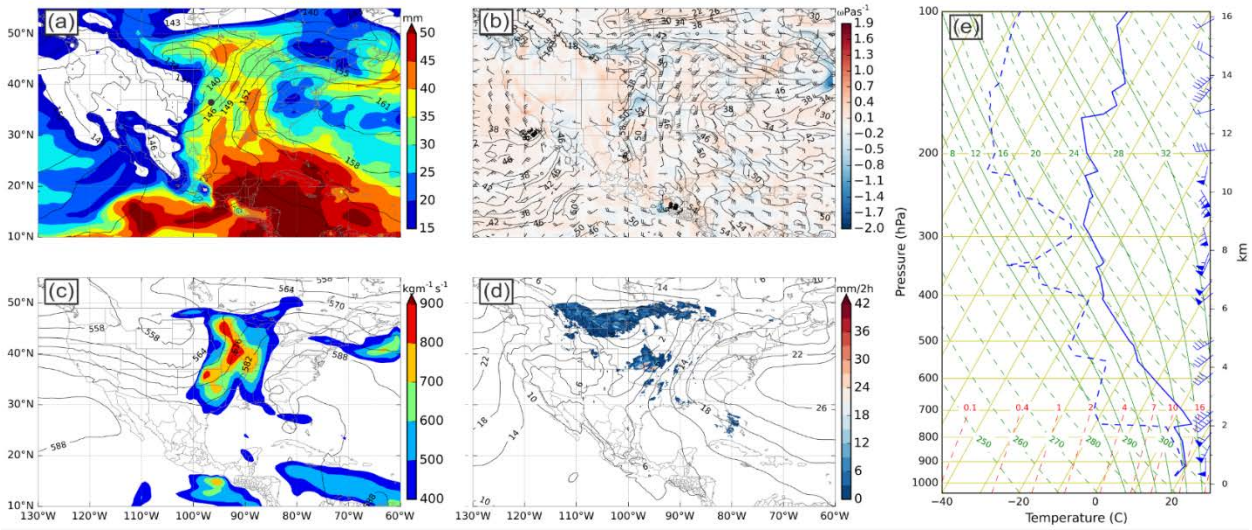

FIG. 2.5 Same as Fig. 2.5 but for 1200UTC, 30 May, 2013. Skew T–log-p plot is for 1200UTC 30th May 2013 with soundings taken at Lamont Oklahoma (Station ID 74646).

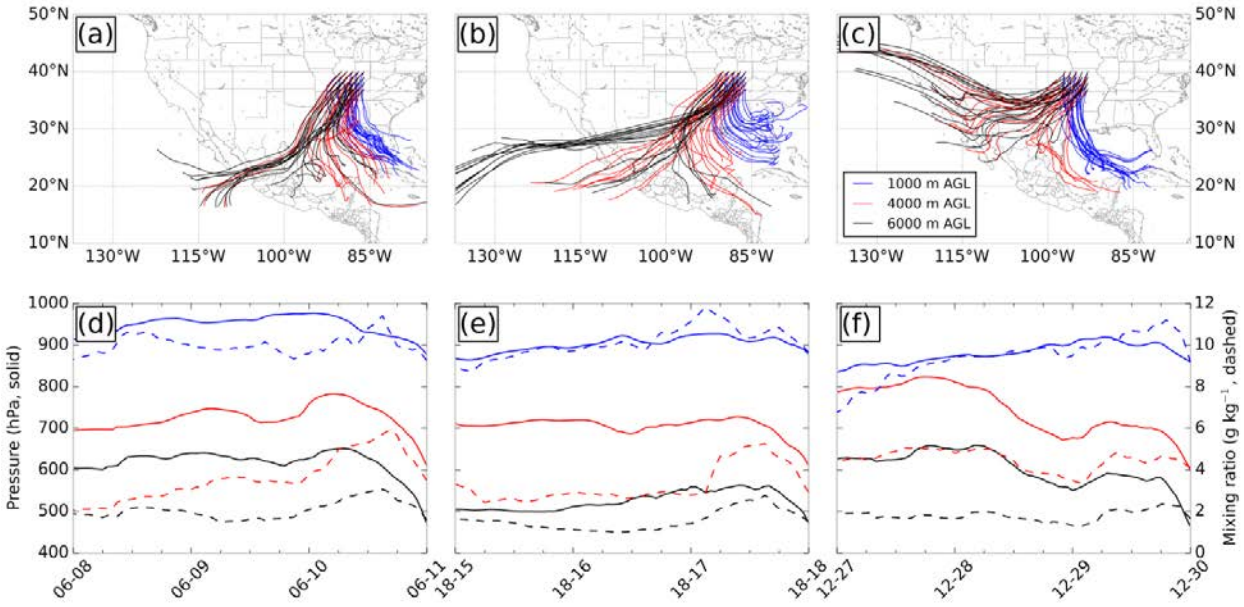

FIG. 2.6: Trajectory analysis of air parcels ending at 0600UTC 11 April (panels a, d), 1800UTC 18 April (panels b, e), and 1200UTC 30 May (panels c, f) for the three ARs. Panels a, b and c represent 72-h backward trajectories for the three ARs with parcels ending at 1000m AGL (blue), 4000m AGL (red) and 6000m AGL (black). Panels d, e, and f show air pressure (solid) and mixing ratio (dashed) along the trajectories. The data in these plots are obtained from NARR analyses using the Hybrid Single Particle Lagrangian Integrated Trajectory (HYSPLIT) model (Draxler and Rolph 2015). Please see text for detailed description.

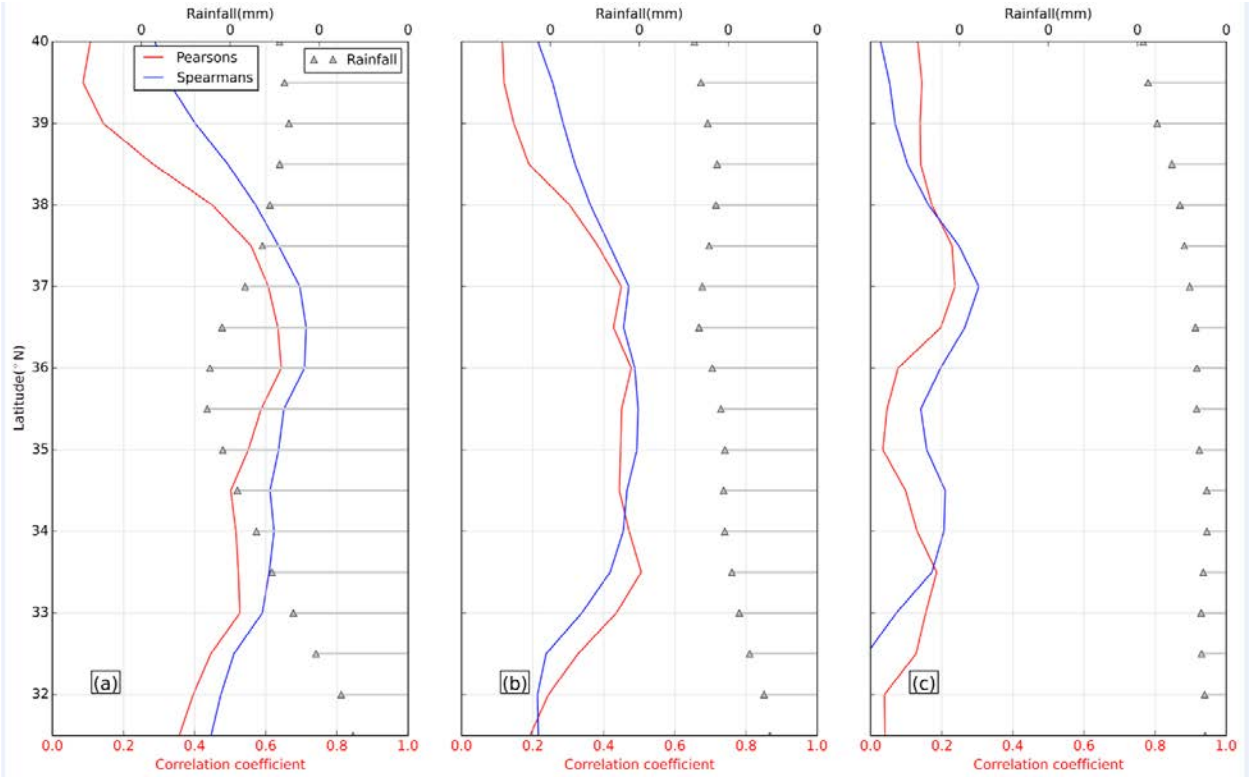

FIG. 2.7: Examination of the relationship between rainfall and AR characteristics for regions at different distances from the AR major axis. Panel a is for the region closest to AR (0km to 74km on both sides from major axis), panel b is for the 2nd closest region (74km to 150km on both sides from major axis), while panel c is for the region farthest away from AR (150km to 370km on both sides from major axis). The plot shows the average rainfall at different latitudes, and Spearman and Pearson correlation coefficients between rainfall (from Stage IV) and IVT (from MERRA).

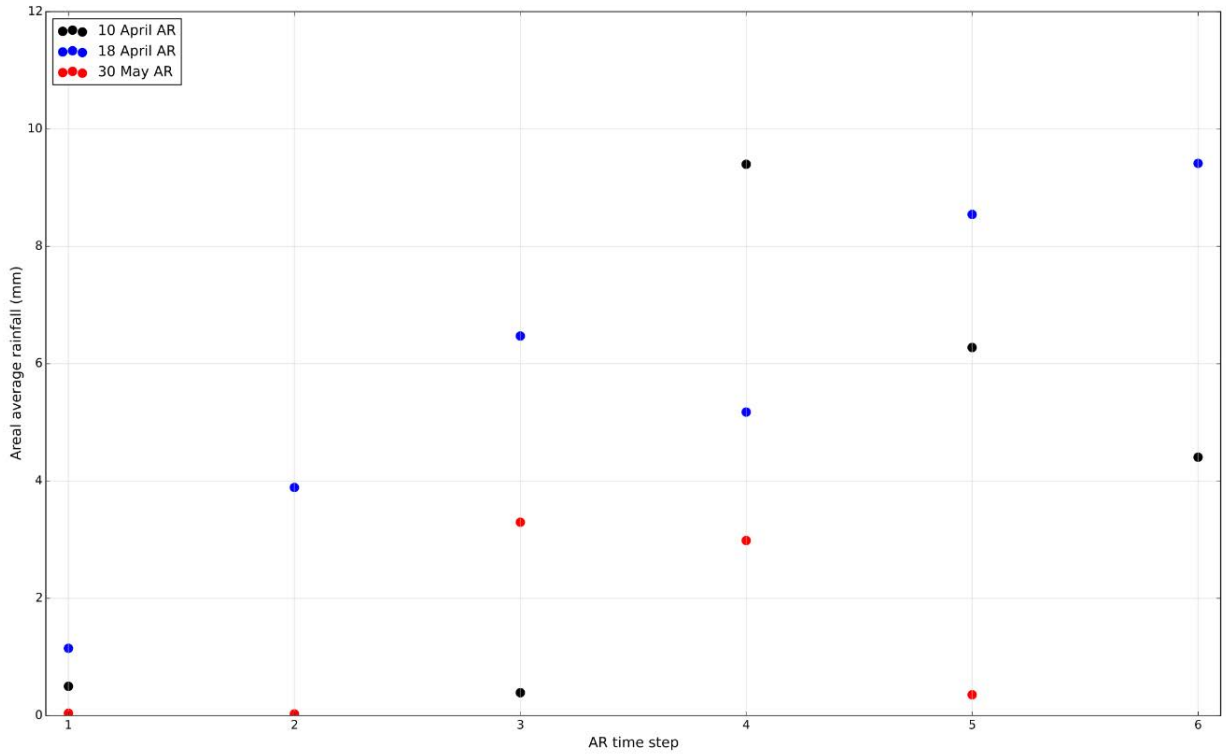

FIG. 2.8: Average rainfall around the AR major axis at different time steps of ARs. The rainfall values are computed from 40°N to 30.5°N within 150km buffer from the AR major axis. The values on the x axis refer to the duration of individual AR events: 1 means the first time step when the AR was identified, 2 means the consecutive 2nd time step of AR condition, and so on.

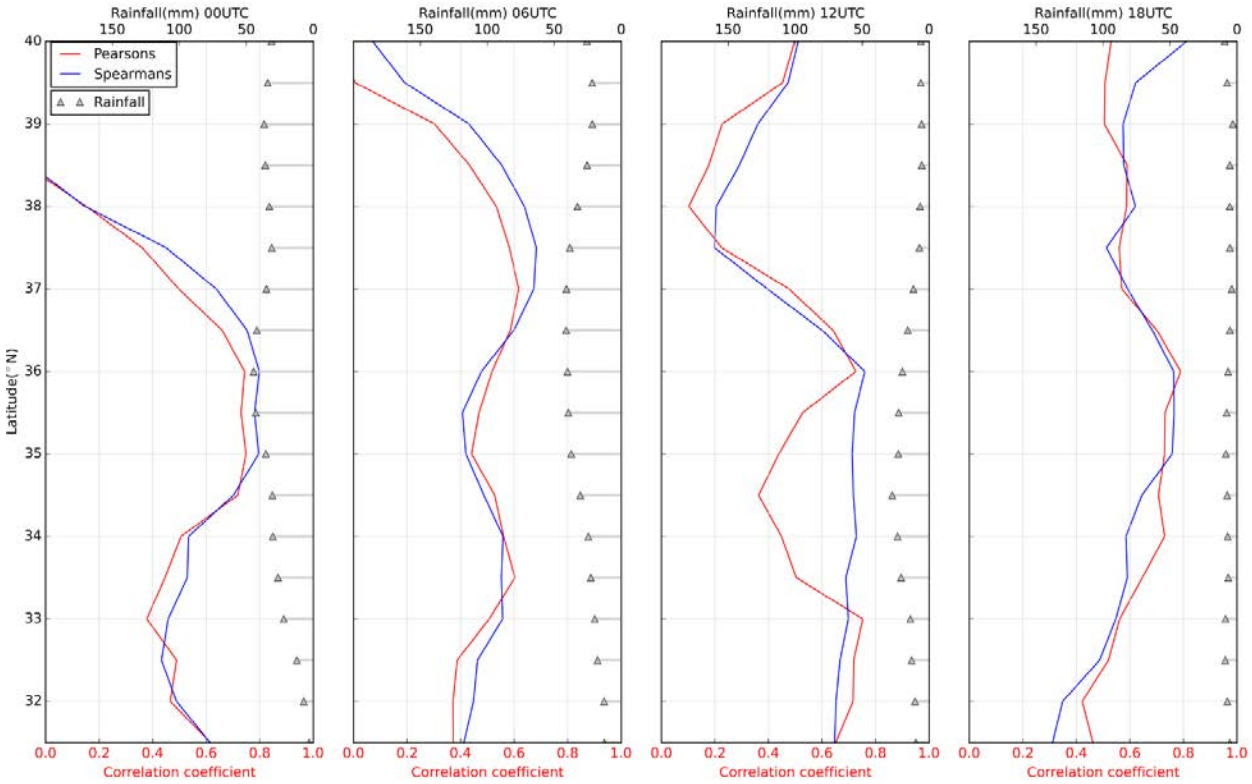

FIG. 2. 9: Similar to Fig. 2.7, but for the four times of a day (panel a is for 0000UTC; panel b is for 0600UTC; panel c is for 1200UTC; panel d is for 1800UTC). Analyses are performed only for the region closest to the AR major axis.

CHAPTER 3

REMOTE SENSING-BASED CHARACTERIZATION OF RAINFALL DURING ATMOSPHERIC RIVERS OVER THE CENTRAL UNITED STATES[2]

Despite the important role ARs play over the central United States, little is known about the distribution of rainfall associated with them. Chapter 2 provided preliminary insights on this subject; however, the results were limited to a very small sample size—a study period of 65 days in which only three ARs occurred. The lack of knowledge regarding the rainfall distribution in ARs is a major gap in the understanding of the science of ARs. Filling this gap serves as the motivation of this chapter. In essence, this chapter builds on and expands Chapter 2 by using a large dataset (13 years), and hence makes it possible to statistically verify the AR-rainfall characterization results previously presented.

Specifically, the research questions I address are:

1. Where is the heaviest rainfall located in the ARs? How quickly does it decrease as we move away from the areas of the most intense transport within these storms?
2. What is the relationship between rainfall intensity and the magnitude of the moisture transport? How does this relationship vary within the ARs and across the central United States?
3. How does AR rainfall change with the duration of these events? Over the U.S. West Coast, for example, Ralph et al. (2013) found that long-duration ARs produce significantly larger amounts of rainfall and stream flow than short-duration events, likely due to the continuous supply of water vapor available for rainout. Over the U.S. West Coast, orographic lifting of moisture-laden air masses results in intense rainfalls (Ralph et al. 2004, and references therein); whereas over the central United States, Mesoscale Convective Systems (MCSs) and frontal systems associated with extratropical cyclones are the main drivers of extreme precipitation events (Kunkel et al. 2012; Stevenson and Schumacher 2014). Although the rain producing mechanisms over the central United States are different than those over the U.S.

[2] Chapter adopted from Nayak, M. A. and G. Villarini,2016: Remote sensing-based characterization of rainfall during atmospheric rivers over the central United States, doi: 10.1016/j.jhydrol.2016.09.039, Journal of Hydrology (in press).

West Coast, it is reasonable to assume that as the duration of the ARs increase, the rainfall may increase here as well. This was observed in the three ARs during the IFloodS period (see Chapter 2). The impact of the duration of ARs on rainfall intensity over the central United States is addressed in this study.

4. How does the AR rainfall magnitude differ during the course of the day? An important characteristics observed in rainfall extremes across the Great Plains is their diurnal cycle. This cycle is the most pronounced in the summer season when most of the extreme rainfall events occur from mid-night to the early morning (e.g., Wallace 1975; Dai et al. 1999). In winter, on the other hand, the diurnal cycle is weak. In Chapter 2, AR-related rainfall for the three ARs in IFloodS showed diurnal character with larger rainfall amounts in nighttime hours than in daytime hours. In this chapter, I will confirm this pattern in AR-related rainfall for a large sample of ARs.

In Chapter 2, I used Stage IV to understand rainfall distribution during three AR events in IFloodS. However, the use of Stage IV does not warrant the best choice as many competitive high spatial and temporal resolution precipitation products are available. To carry out the analyses in this chapter and address the research questions listed above, I will use quantitative precipitation estimates (QPE) from different remote sensing products. Over the past decade, we have seen the development of several datasets providing QPE, each with different strengths and weaknesses. As part of this study, I will focus on one radar-based and four satellite-based rainfall products and perform a comprehensive evaluation with respect to a rain-gage based reference product. While the evaluation of remote-sensing product is topic addressed in several previous studies (e.g., Villarini and Krajewski 2007; Vila et al. 2009; Villarini et al. 2009; AghaKouchak et al. 2011; Chen et al. 2013; Derin and Yilmaz 2014; Puca et al. 2014; Cai et al. 2015; Prat and Nelson 2015; Zhang et al. 2015), how well different products can represent AR rainfall is a topic that requires further investigation. AghaKouchak et al. (2011) compared four satellite products and concluded that none of the products can be treated as best suited to characterize extreme rainfalls. Further, the performance of the products decreases as the events become more extreme. A more recent study by Prat and Nelson (2015) also highlights the poor performance of satellite and remote sensing products in capturing extreme rainfall. Further

challenges arise due to the peculiar structure of narrow and long rain bands that have been observed in some ARs studied over the central United States (e.g., Moore et al. 2012; see also Chapter 2). Hence, from an AR perspective, it is important to evaluate different remote sensing products to select the best product before performing rainfall characterization in ARs.

3.1 Data and Methods

3.1.1 Data

I evaluated one ground-based and four satellite-based products for characterizing rainfall during ARs: 1) Stage IV; 2–3) the Tropical Rainfall Measuring Mission (TRMM) Multisatellite Precipitation Analysis (TMPA) (Huffman et al. 2007) Version 7 for research (TRMM 3B42-V7) and near-real-time (TRMM 3B42RT-V7); 4) Precipitation Estimation from Remotely Sensed Information using Artificial Neural Networks (PERSIANN, Sorooshian et al. 2000); 5) Climate Prediction Center (CPC) morphing method (CMORPH, Joyce et al. 2004). For simplicity, throughout the paper, I will address TRMM 3B42-V7 as TRMM and TRMM 3B42RT-V7 as TRMMRT.

As mentioned in Chapter 2, Stage IV is a fine resolution precipitation product and the data can be obtained at hourly, 6-hourly and daily temporal resolutions. The data are available from 2002 to the present over most of the conterminous United States at approximately 4km × 4km horizontal resolution. The data are a mosaicked analysis, performed at NCEP, from precipitation estimates produced by 12 Regional Forecasting Centers (RFCs) across the United States. All the RFCs that encompass the central United States use multi-sensor precipitation estimates from Weather Surveillance Radar-1988 Doppler (WSR-88D) radars merged with hourly rain gauge measurements. The hourly rain gauge data for these RFCs come from either all or some of the real-time gauges of the Hydrometeorological Automated Data System (HADS) gauges, the Automated Surface Observing System (ASOS), and the Automated Airport Weather Stations (AWOS) reports. See Hou et al. (2014) for further details on Stage IV analysis. A manual quality control is performed at each RFC.

The two TMPA datasets (TRMM and TRMMRT) are available from 1998 and 2000, respectively. Both datasets are at 3-hourly temporal resolution and 0.25º × 0.25º horizontal

resolution. TRMMRT estimates are obtained by calibrating and merging passive microwave data and ~10μm band infra-red (IR) data from sensors on different satellites. The passive microwave data are obtained from TRMM Microwave Imager (TMI) on TRMM satellite, the Special Sensor Microwave Imager (SSM/I) on Defense Meteorological Satellite Program (DMSP) satellites, the Advanced Microwave Sounding Unit-B (AMSU-B) on the National Oceanic and Atmospheric Administration (NOAA) satellites, and the Advanced Microwave Scanning Radiometer-Earth Observing System (AMSR-E) on Aqua. The IR data are obtained from the international constellation of Geosynchronous Earth Orbit (GEO) satellites. For the research version TRMM, monthly gauge-based precipitation data from Global Precipitation Climatological Center (GPCC, Rudolf 1993) and the Climate Assessment and Monitoring System (CAMS, Xie et al. 1996) are used to adjust this product on a monthly basis. For detailed information regarding TMPA estimates refer to Huffman et al. (2007).

CMORPH and PERSIANN data are available at 0.25º × 0.25º horizontal resolution. The finest temporal resolution for CMORPH is 3-hourly and data are available from December 2002 to the present. PERSIANN data are available at 3-hourly, 6-hourly and daily temporal resolutions from March 2002 to the present.

The reference data used to evaluate the remote sensing products is CPC's gauge-based precipitation, which are at daily temporal resolution, 0.25º × 0.25º horizontal resolution, and available from 1948 to the present. Presently, CPC extracts daily rainfall data from daily rainfall reports provided by about 13000–15000 stations (Higgins et al. 2000). RFCs provide daily reports at about 8000 stations, and around 4000 are independently provided by National Climatic Data Center (Hou et al. 2014). Hou et al. (2014) estimate that out of the 8000 stations provided by RFCs, 90% have data available at hourly temporal resolution, which could have been used to obtain the Stage IV hourly estimates as well. This implies that CPC and Stage IV data are not completely independent, even though there are differences because of the use of different quality controls at each RFC and the availability of 4000 additional independent stations in CPC. With that said, I expect Stage IV and TRMM to show closer agreements to the reference CPC data.

3.1.2 AR identification

For identifying ARs, I followed the same methodology that I presented in Chapter 2; similarly, MERRA data are used to detect ARs over the 2002–2014 period, consistent with the data availability of the precipitation products. A modification to the identification algorithm in the calculation of threshold that is used the selection of the IVT threshold that is used to screen potential AR and non-AR time steps Instead of a constant 550kgm^{-1}s^{-1} threshold, a daily-varying threshold is obtained as follows. At the latitude 40ºN, daily average IVT fields, calculated from the four 6-hour time steps of the day, are calculated at each grid point of the longitude band of 100ºW to 85ºW for all the years from 2002 to 2014. Then, for each day the maximum IVT value is selected in the longitude band for all the days in the dataset, and a 15-day moving-average smoothing is performed for each day. In this way, for each day of the year, we have a time series (one value for each year) of smoothed maximum IVT values, and the threshold is taken as the 85th percentile of the time series of the day. I treat this as the daily-varying threshold for AR identification. An important feature of the daily-varying threshold is that it takes into account the seasonality that is prevalent in the water vapor transport over the central United States.

3.1.3 Evaluation methods

I evaluate and compare all the precipitation products for a common period of 12 years from 2003 to 2014. Data from CMORPH are available only after December 2002, so I start evaluation from 2003. First, all the products are brought to a common spatial and temporal resolutions of 0.25º × 0.25º and (1200UTC to 1200UTC), respectively. For visual comparison, I calculate total rainfall and rainfall associated with AR for the 12-year period from CPC and the five remote sensing products. I refer to the rainfall within a 250km buffer around the AR major axis as the rainfall associated with the AR (or AR-related rainfall). I perform different quantitative evaluations to get a better idea of any under- or over-estimation by the remote sensing products. Daily rainfall estimates from remote sensing products are compared with CPC rainfall amounts at each grid point over the central United States (30ºN to 50ºN and 85ºW to 100ºW) with the help of boxplots and scatter plots. Further, objective evaluation measures are also considered, including Pearson's product moment correlation coefficient (correlation coefficient from here onwards), Mean

Absolute Error (MAE) and Mean Squared Error (MSE). For each of the five products, I calculate these measures at each grid point from daily rainfall data of 12 years. These analyses are performed for rainfall associated with ARs as well.

3.1.4 Rainfall distribution in ARs

To understand how rainfall is distributed within ARs, I consider three separate regions around the AR major axis, similar to Chapter 2 but with minor changes. The first region, the one closest to the AR major axis, covers the area within 75km on both sides of the major axis (i.e., on east side and west side of the major axis). The second region is the area from 75km to 150km, while the third region is from 150km to 300km. In all the three regions, I calculate 4-hr accumulated rainfall, 2 hours before the AR time step and 2 hours after the AR time step for all the ARs from 2002 to 2014. This is possible because I use Stage IV which is the product that shows the closest agreement with CPC, as discussed in the next section. These accumulations are obtained for each latitude point (from 30ºN to 40ºN, which is the latitudinal range used to define ARs).

Another important question is related to the relationship between IVT magnitude in ARs and the corresponding rainfall magnitude. I expect higher rainfall amounts corresponding to large IVT magnitudes, even though this depends on precipitation efficiency and the location of cold fronts for the lift. To examine this, at each latitude I calculate the Spearman correlation coefficient between IVT and rainfall magnitudes during ARs to quantify monotonic relationship between the two variables.

To understand the impact of AR duration on rainfall, for each AR time step, 4-hr rainfall accumulations are calculated (2 hours before the AR time step and 2 hours after it) within a 250km buffer around the major axis. The first time step of an AR defines the start of the event; as the AR duration increases, the time steps increase. The accumulated rainfall for each AR time step is divided by the number of grid cells encompassed by the 250km buffer to give 4-hr rainfall intensities. The rainfall corresponding to each AR time step is averaged across all ARs from 2002 to 2014. Hence, we get an average 4-hr rainfall per pixel for each AR time step. We can compare the rainfall intensity of different AR time steps, providing us with an insight on the effect of AR duration on rainfall.

Finally, I verify the diurnal variation observed in Chapter 2 in the rainfall associated with ARs. As in Chapter 2, I consider four times for which MERRA provides data (i.e.,

0000UTC, 0600UTC, 1200UTC and 1800UTC). At each of these time steps, I compare rainfall amounts in the region closest to the major axis (i.e., the area within the 75km-buffer around the major axis) at each latitude point from 30ºN to 40ºN. Moreover, at each of the four times of the day, I calculate the Spearman correlation coefficient between rainfall and IVT magnitudes to detect any time-dependent relationship between the two variables.

3.2 Results and Discussion

3.2.1 Evaluation of remote sensing products

The average annual rainfall and the contribution from ARs using CPC for the 2003-2014 period are shown in Figure 3.1. Distinct spatial variations can be observed in the average annual rainfall, with areas receiving less than 500mm on the west part of the central United States (east of the Rockies) and areas receiving more than 1700mm around the Gulf of Mexico (Figure 3.1, top-left panel). A large stretch of the central United States receives significant contribution to the annual rainfall from ARs (Figure 3.1, top-right and bottom-left panels). Generally, regions characterized by large rainfall have relatively large fractions (about 25%–35%) contributed by ARs. These areas also resemble reasonably well the regions of high AR density (Figure 3.1, bottom-right panel) defined here as the average frequency of AR-days per year over the period 2003–2014. As can be expected from the AR characteristics, the shape of the areas with the largest AR contributions resembles extratropical storm track on the west side of the Appalachian Mountains.

The magnitude and the spatial structure of average annual rainfall and AR contribution from the remote sensing products are shown in Figure 3.2 and can be compared with CPC (Figure 3.1). Stage IV is the product that most closely resembles the CPC results, followed by TRMM (Figure 3.2, top panels). The other three products (TRMMRT, CMORPH and PERSIANN) show overestimation over much of the Great Plains including the states of Iowa, Missouri, Kansas, and Arkansas. Similar to what was found for the average annual rainfall, these three products underestimate the fractional contribution from ARs to annual rainfall over much of the central United States, which is instead much better captured by Stage IV and TRMM (Figure 3.2, middle and bottom panels). Overall, the visual examination of these figures indicates that Stage IV most closely resembles the reference

data, followed by TRMM. These findings also underline the importance of the bias correction of the remote sensing-based precipitation estimates.

Figure 3.3 shows 2-d histograms of the daily rainfall (left panels) and AR-related rainfall. Most of the points in the Stage IV panels (Figure 3.3, top row) are scattered symmetrically around and close to the 1:1 line. There is a lack of symmetry for the other products both for the overall and AR-related rainfall. This suggests that Stage IV has the lowest bias. Another feature that distinguishes Stage IV from the rest of the products is the smallest spread in its scatter, pointing to its higher precision. Figure 3.4 shows the boxplots of the errors in daily rainfall per pixel (top panel) and AR-related rainfall (bottom panel). The errors are calculated as the difference between the remote sensing product and CPC rainfalls (reference). All products, except Stage IV, show positive biases. Stage IV and TRMM have lower variances (i.e. higher precision) than the other products. When focusing on the AR-rainfall, Stage IV and TRMM show the best performance. Although TRMMRT has the lowest bias, its variance is quite high. CMORPH and PERSIANN both show negative biases (i.e., underestimation) and large variances. It is interesting to note that CMORPH and PERSIANN show an underestimation in daily rainfall and overestimation in AR-related rainfall.

Quantitative comparisons between the remote sensing-based products and CPC rainfall are plotted for daily rainfall and AR-related rainfall in Figures 3.5 and 3.6, respectively. When considering Stage IV, the correlation coefficients (top panels) are larger than 0.9 over much of the central United States. Similarly, MAE and MSE (middle and bottom panels, respectively) are small (~1mm/day and $3mm^2/day^2$, respectively) over this area. These results indicate that there is a strong agreement between CPC and Stage IV daily rainfall estimates, likely the results of the bias correction with respect to the rain gages. Among the other products, TRMM shows a better performance over most of the region, even though the results are worse than what observed for Stage IV. As seen earlier in the graphical comparisons, the other three products show limited performance over much of the Great Plains. The results for the daily rainfall (Figure 3.5) hold for the AR-rainfall (Figure 3.6). Note that since ARs generally result in high magnitude rainfall (10.7mm per day per grid cell as compared to 2.6mm daily average in a year), the error scales are higher (Figures 3.4–3.6).

From the results of this section, it is clear (and not surprising) that Stage IV is the product that most closely reproduces the observed rainfall. This is true with respect to both daily and AR-related rainfall. The superior performance and the fact that Stage IV has high temporal and spatial resolutions makes this product well-suited for characterizing the rainfall distribution during ARs.

3.2.2 Rainfall characteristics during ARs

Figure 3.7 shows the rainfall distribution in the three regions around the AR major axis (see Section 3.1.4) as a function of latitude. In general, most of the rainfall occurs in the mid-latitudes from 33ºN to 38ºN, with peak rainfall amounts at around 35.5ºN in the closest region to the AR major axis (~10mm/4-hour at each grid cell). In all the three regions, the rainfall gradually decreases as we move away from 35.5ºN. An evident feature in Figure 3.7 is the decrease in rainfall as we move from the closest region to the AR major axis (left panel) to the region farthest away from it (right panel). These results are similar to what I obtained in Chapter 2 for the three ARs during IFloodS. I performed multiple comparisons using two sample Student's t-tests to statistically test whether the decrease in rainfall in the three regions is statistically significant. Bonferroni adjustments are performed to take into account multiple comparisons instead of a single comparison. At each latitude, three comparisons are performed: 1) rainfall in the first region is greater than rainfall in the second region; 2) rainfall in the second region is greater than rainfall in the farthest region; and 3) rainfall in the first region is greater than the rainfall in the farthest region. Figure 3.8 shows the Bonferroni-adjusted p-values corresponding to each comparison at each latitude. Based on these results, there is strong statistical evidence (p-value smaller than 0.01) that on average the AR rainfall decreases as we move away from the major axis, in particular between 29ºN and 42ºN. The difference extends beyond this latitude band, albeit with lesser evidence to support it. The results in Figures 3.7 and 3.8 show that the largest differences are between the third region and regions one and two, further indicating the narrow nature of ARs in terms of rainfall, with most of the rainfall concentrated within 150km around the AR major axis.

In Figure 3.7 I also plot Spearman rank correlation between IVT and rainfall magnitudes as a function of latitude. IVT and rainfall show the largest values of Spearman correlation coefficient in the first region (within 75km of the AR major axis) and between

30ºN and 40ºN. This relationship weakens as we move further away from the major axis and this latitudinal band. Pearson's correlation coefficient, which measures the strength of linear relationships, also shows similar trends in all the three regions (not shown). These results suggest that in the region closest to AR major axis, higher rainfall may be expected with higher amounts of water vapor transported.

AR duration has a major effect on the rainfall associated with these events (Figure 3.9). I used a maximum duration of 90 hours in our plot because only three ARs lasted longer. There is a strong dependence of AR rainfall on its duration, with on average twice as much rainfall in storms lasting three days compared to one-day ARs. From an impact perspective, these results suggest that when ARs persist for longer durations, heavy, flood-producing rainfall events can be expected. Moreover, the rainfall intensity does not decrease even when the duration has reached 90 hours. This is different from what is observed in the western United States where rainfall intensity decreases quickly after much shorter durations than observed here (Figure 7 in Ralph et al. (2013)).

Finally, I examine whether there are differences in ARs during the course of the day focusing on the areas closest to the AR major axis (Figure 3.10). There is a marginal difference between the rainfall magnitudes at 0000UTC and 1800UTC; however, by performing one-way Analysis of Variance (ANOVA) tests, I do not see a major difference in rainfall magnitudes among the four times of the day. This suggests that a weak or zero diurnal variation exists in rainfall associated with ARs. This is not consistent with the results in Chapter 2, where a distinct diurnal variation was observed. Earlier studies have shown that diurnal variations in extreme rainfall over the central United States are predominant in summer and have a weaker signature in winter (Dai et al. 1999). Wallace (1975) also observed that the diurnal variations in heavy rainfall events during winter over the U.S. Midwest had smaller amplitude in the winter than in the summer. Because AR frequency is the largest in winter and spring, and the smallest in summer (Lavers and Villarini 2013b), our findings of weak or no diurnal variations in AR-related rainfall are consistent with past observations and physical understanding of ARs. Figure 3.10 also shows that the relationship between AR-related rainfall and IVT magnitudes is similar across all the times of the day, with larger rainfall magnitudes in the mid-latitudes.

3.3 Summary and Conclusions

In this chapter, I have focused on the characterization of rainfall associated with ARs that affected the central United States over the 2002–2014 period. Over this regions, the fractional contribution of ARs to annual rainfall can be as high as 35%. For characterizing the AR rainfall, a suite of remote sensing-based precipitation products are evaluated. Stage IV showed the closest agreement with the reference rainfall data in terms of both total rainfall and rainfall associated with ARs. TRMM turned out to be the next best product.

In understanding the rainfall distribution in ARs, I found that most of the rainfall during ARs is located within about 150km around the AR major axis, and the magnitude of the rainfall has a significant monotonic relationship with IVT magnitude. Rainfall as well as its relationship with IVT vary as a function of latitude with peak rainfall magnitudes in the latitude band 32ºN–36ºN. The AR duration is an important factor in determining the intensity of rainfall. As the AR duration increases, rainfall intensity increases. Weak diurnal variations are observed in the rainfall around the AR major axis, with marginally larger rainfall during evening and night hours as compared to daytime hours.

The results from this chapter provide significant contribution to the scientific knowledge about rainfall in ARs. Improved understanding of the distribution of rainfall during ARs and how it relates to water vapor transport can help to better model or constrain the precipitation process in regional and numerical weather prediction models. Over the central United States, numerical weather prediction models forecast ARs with good skill up to a lead-time of 7 days (see Chapter 6) Therefore, The results here can have a direct impact on developing flood protection strategies during ARs as once we know the AR location and duration, it is possible to anticipate the location and intensity of maximum rainfall.

3.4 Figures Chapter 3

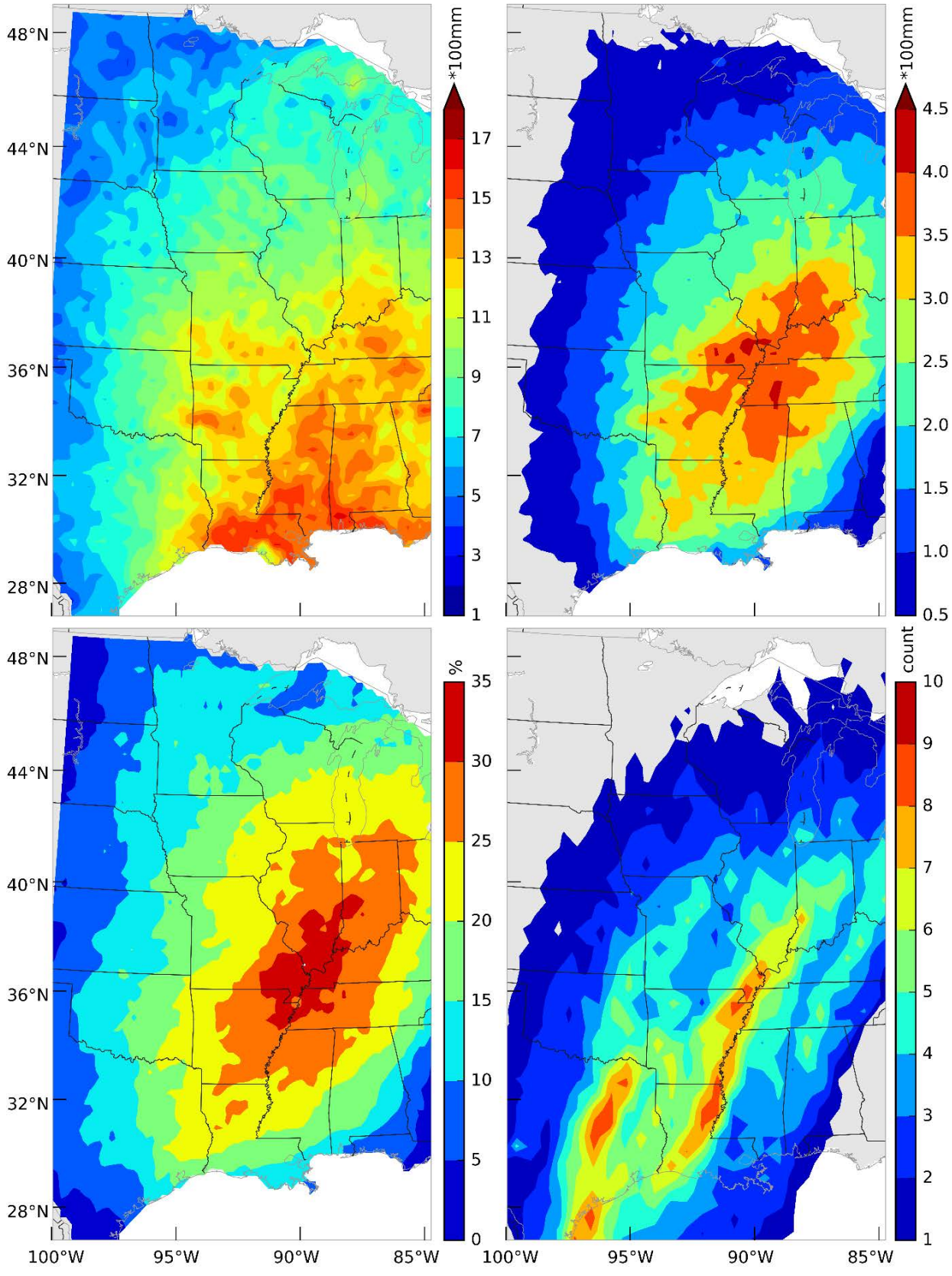
48°N
44°N
40°N
36°N
32°N
28°N
*100mm
17
15
13
11
9
7
5
3
1
*100mm
4.5
4.0
3.5
3.0
2.5
2.0
1.5
1.0
0.5
%
35
30
25
20
15
10
5
0
count
10
9
8
7
6
5
4
3
2
1
100°W
95°W
90°W
85°W

FIG. 3.1: Annual rainfall and AR-related rainfall based on CPC data for the 2003–2014 period. Annual average rainfall (top-left panel), annual averaged rainfall associated with ARs (top-right panel), AR fractional contribution to the total rainfall (bottom-left panel), and AR density (defined as the average frequency of AR-days per year over the period 2003–2014; bottom-right panel).

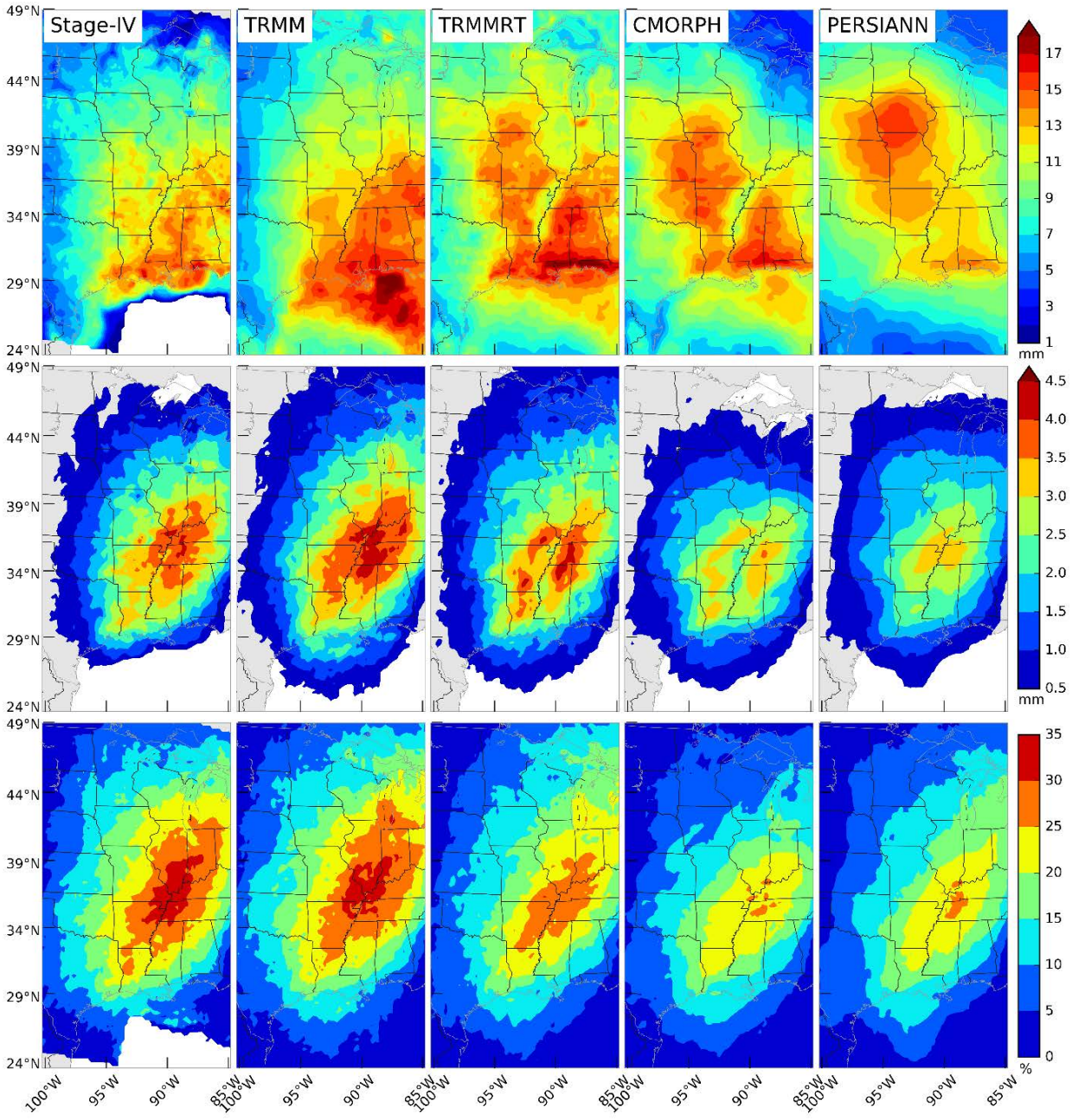

FIG. 3.2: Annual rainfall and AR-related rainfall based on remote sensing-based precipitation products. Annual average rainfall (top rows), rainfall associated with ARs (middle rows), and fractional contribution to the total rainfall from ARs (bottom rows).

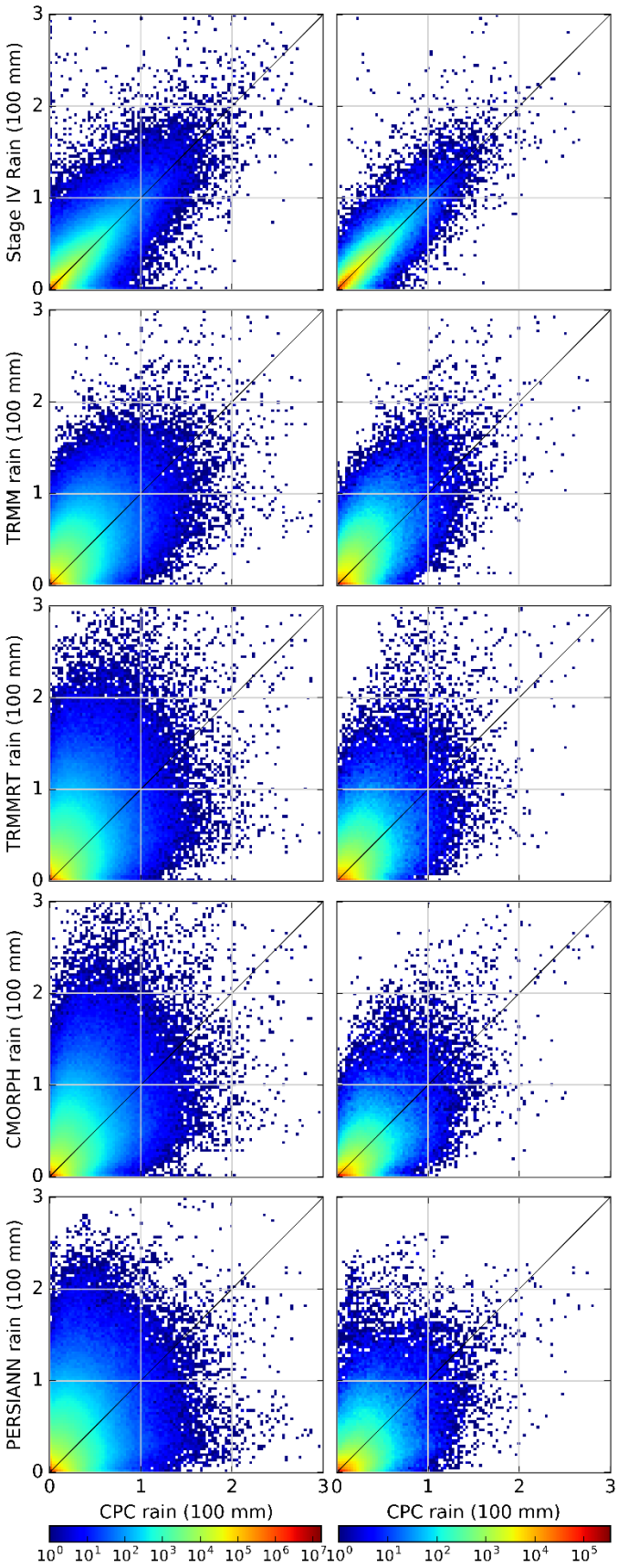
Stage IV Rain (100 mm)
TRMM rain (100 mm)
TRMMRT rain (100 mm)
CMORPH rain (100 mm)
PERSIANN rain (100 mm)
0
1
2
3
CPC rain (100 mm)
CPC rain (100 mm)
10^0 10^1 10^2 10^3 10^4 10^5 10^6 10^7
10^0 10^1 10^2 10^3 10^4 10^5

FIG. 3.3: Two-dimensional histograms between CPC and remote sensing-based precipitation products: daily rainfall (left panels) and AR-related daily rainfall (right panels). The colorbars show the number of scatter points falling within each bin in the plots. The black line shows the 1:1 line, representing a perfect match between CPC and the remote sensing product.

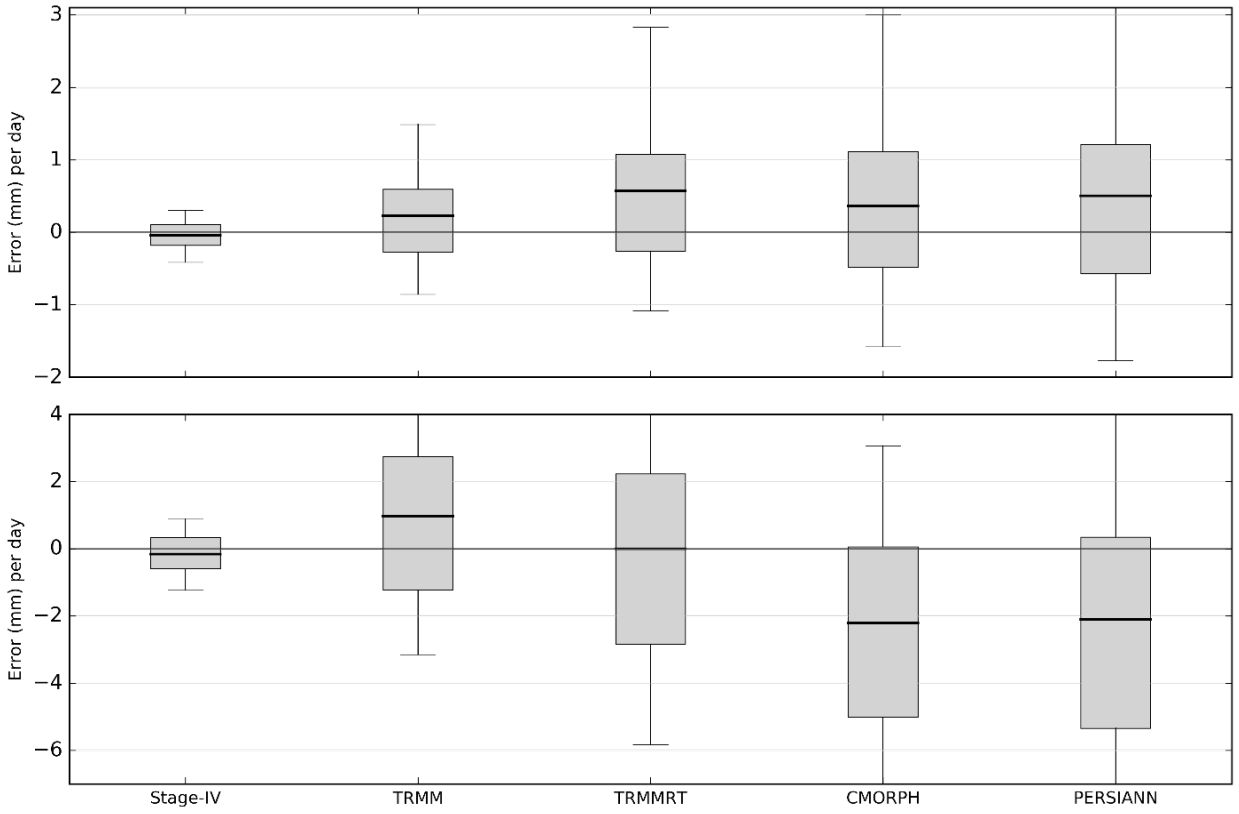

FIG. 3.4: Boxplots showing the errors (difference between the remote sensing products and CPC rainfall; mm per day per grid cell) in daily rainfall (top panel) and AR-related rainfall (bottom panel). The boxes cover the lower and upper quartile of the data. Lower and upper whiskers represent 10th and 90th percentiles, respectively. The solid black line in each box represents the mean of the data.

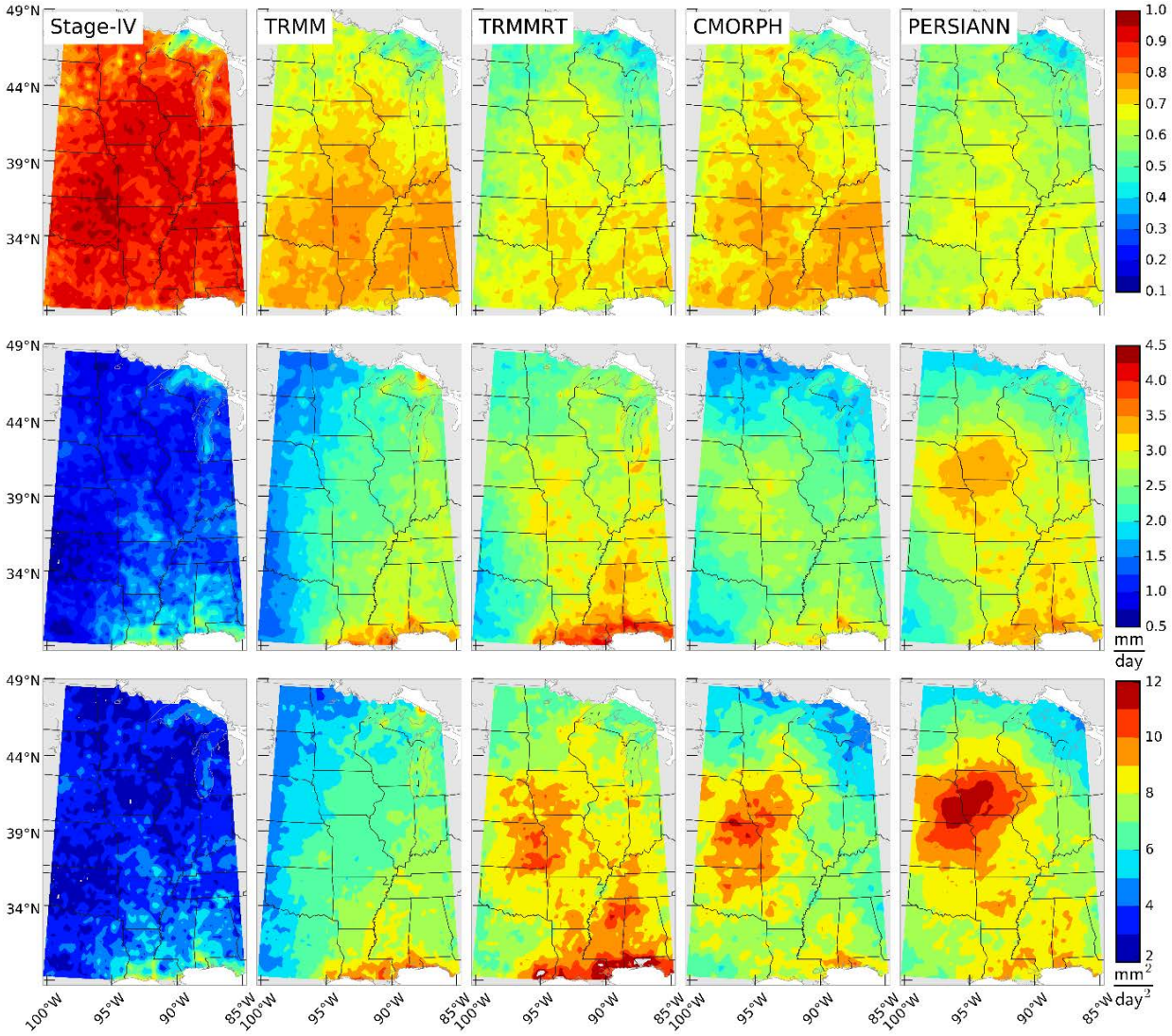

FIG. 3.5: Metrics-based comparison of daily rainfalls between CPC and remote sensing-based products. Pearson's correlation coefficient (top panels), Mean Absolute Error (in mm/day; middle panels), and Mean Squared Error (in mm^2/day^2; bottom panels).

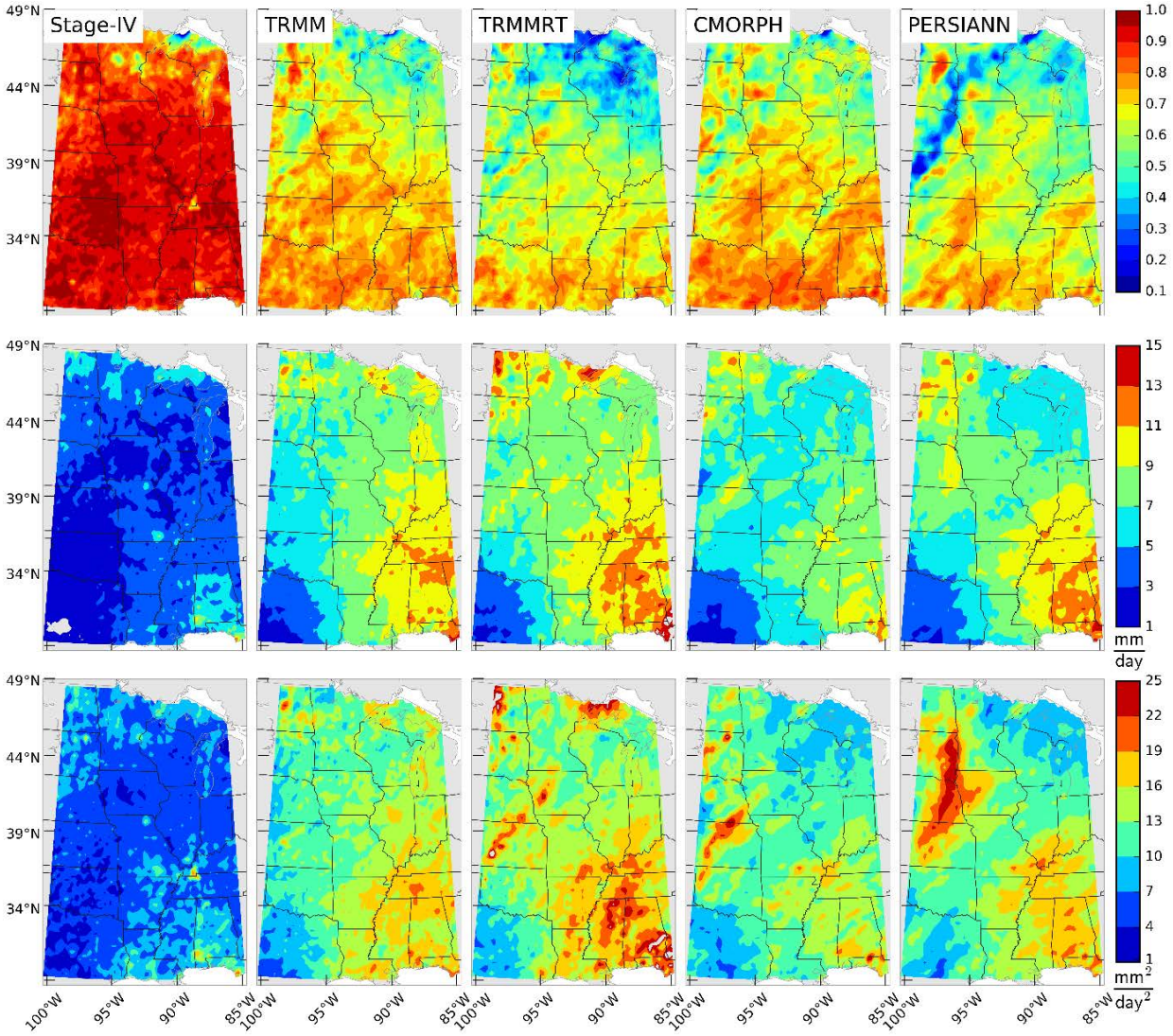

FIG. 3.6: Same as Figure 3.5, but for AR-related rainfall.

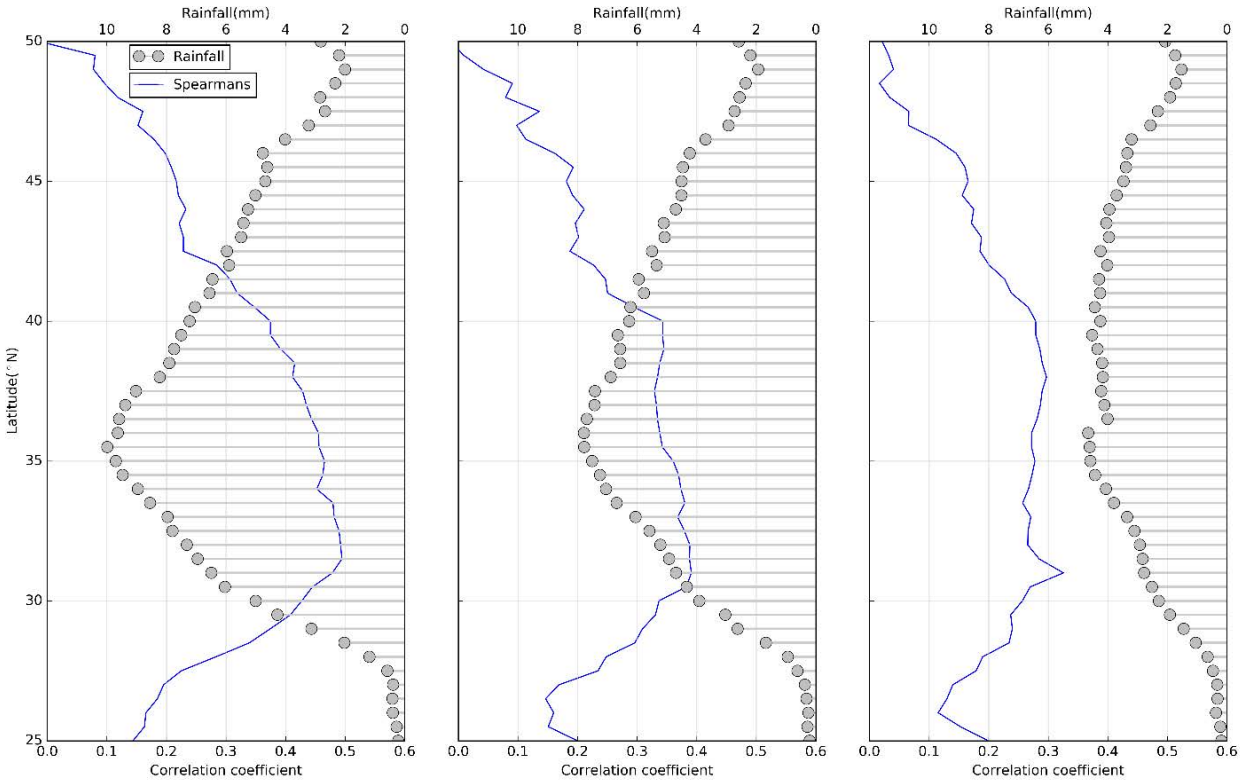

FIG. 3.7: Rainfall distribution within ARs. Rainfall intensity (mm/4-hr per grid cell) within the first region (i.e., the region within 75km from the AR major axis; left panel), the second region (i.e., the region within 75km and 150km from the AR major axis; middle panel), and the third region (i.e., the region within 150 km and 300 km from the AR major axis; right panel). Blue lines are the Spearman's rank-based correlation coefficient between rainfall and IVT magnitudes. See text for more information.

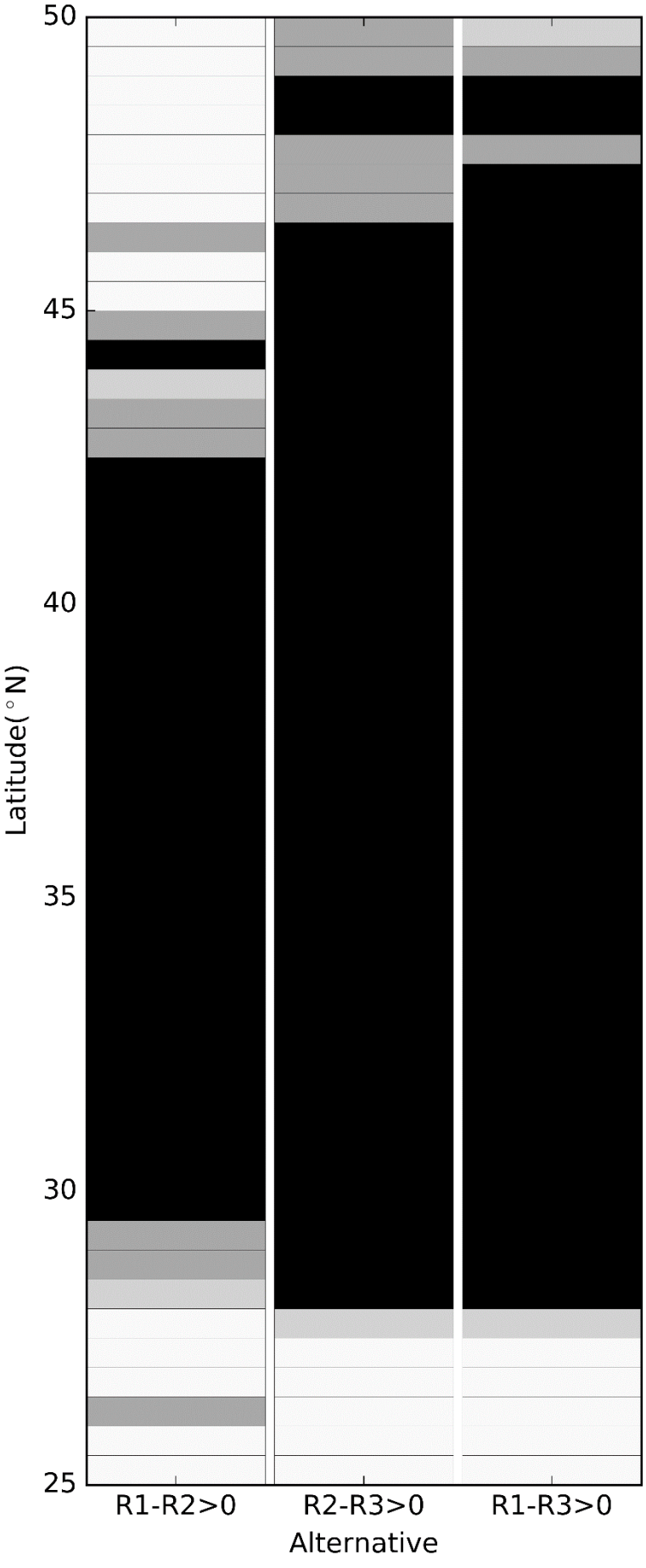
50
45
40
35
30
25
Latitude(°N)
R1-R2>0
R2-R3>0
R1-R3>0
Alternative

FIG. 3.8: P-values from multiple comparisons regarding the rainfall differences in the three regions around the AR major axis. Rainfall in first region is denoted as R_1, while R_2 and R3 are the rainfall amounts in second and third regions, respectively. The null hypothesis is that the rainfall difference in two regions is zero (e.g., Ho: $\mu(R_1) - \mu(R_2) = 0$). The alternatives are shown in the x-axis. Bonferroni adjustments are performed on the p-values to take into account multiple comparisons. Color notation: p-value <0.01 = black; p-value between 0.01 and 0.05 = dark gray; p-value between 0.05 and 0.10 = light gray; p-value >0.10 = white.

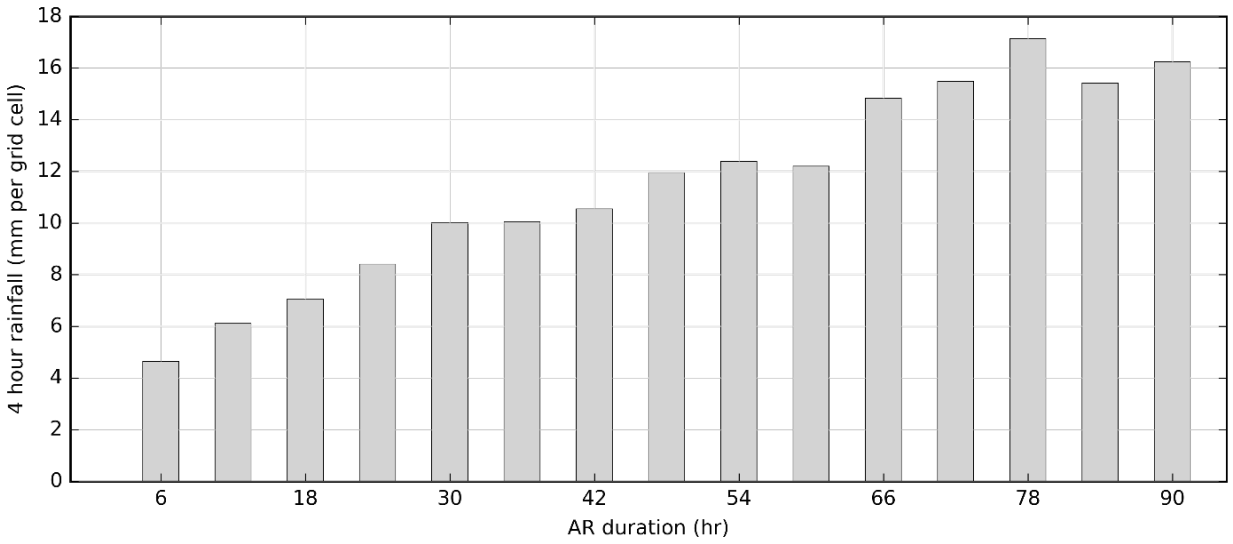

FIG. 3.9: Average AR-related rainfall intensity (mm/4-hr per grid cell) as a function of duration (persistence) of ARs.

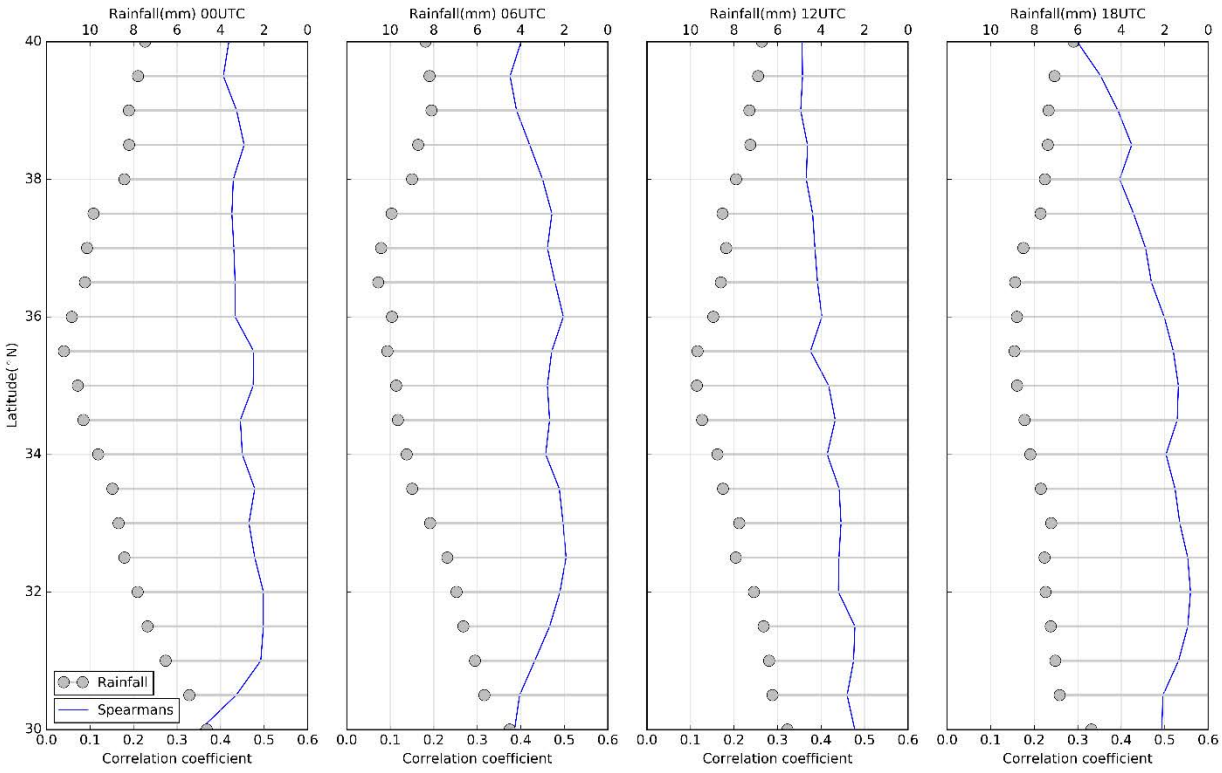

FIG. 3.10: Diurnal variation in AR-related rainfall. Same as Fig. 3.7, but for AR-related rainfall and different times of the day. The analysis corresponds to the region within 75 km around the AR major axis.

CHAPTER 4

A LONG-TERM PERSPECTIVE OF THE HYDROCLIMATOLOGICAL IMPACTS OF ATMOSPHERIC RIVERS OVER THE CENTRAL UNITED STATES[3]

The thesis has thus far focused on detailed assessments regarding the synoptic conditions associated with ARs (Chapter 2) and the rainfall distribution associated with them (Chapter 3) for relatively small study periods. This chapter comprehensively expands on the previous ones and is dedicated to the development of the climatology of ARs over the central United States based on multiple, long-term, state-of-the-art atmospheric reanalysis products. With the AR climatologies are available, this chapter examines the role played by ARs in the hydroclimatology of the central United States. I start this chapter by reviewing relevant recent studies on the impacts of ARs over this region, with the aim to elucidate the unanswered research questions that I intend to address here.

In Chapter 3, the distribution of rainfall during ARs was evaluated and, in doing so, I also found that the AR contribution to annual precipitation over a period of 12 years (from 2002–2014) ranged from 15–35% (Figure 3.1). In this chapter, I intend to expand the analyses to extreme precipitation events and floods over this regions. Steinschneider and Lall (2015b) evaluated the association between Tropical Moisture Exports (TMEs) and extreme precipitation events over this region. As mentioned in Chapter 1, TMEs consist of high-moisture parcels in the atmosphere that strictly originate from the tropics and maintain tropical characteristic while entering the central United States; furthermore, their structure can cover broader regions as compared to the river-like structure of moisture transport in ARs. ARs can originate in the tropics and subtropics, and the air parcels can gain significant amount of moisture from the oceanic and/or land surfaces along their tracks (Bao et al. 2006; Dacre et al. 2015). Steinschneider and Lall (2015b) used Archetypical Analysis to examine the spatial structure of extreme rainfall events and their association with TMEs. In the analysis, the architypes of extreme precipitation and TME-based precipitation matched closely, particularly over the northern and north-eastern parts of the central United

[3] Chapter adopted from Nayak, M. A. and G. Villarini, 2016: A long-term perspective of the hydroclimatological impacts of atmospheric rivers over the central United States, Water Resources Research (Under revision)

States; this suggests that TMEs are associated with most of the extreme precipitation events over this region. The study by Steinschneider and Lall (2015b), however, did not attempt to quantify the contribution of TMEs to extreme precipitation events. Recently, Mahoney et al. (2016) studied ARs over the southeastern United States (90º–75ºW and 31º–39ºN, which includes a part of the central United States as defined here) and their impacts on heavy precipitation events over the region. Among the 25 large-scale heavy precipitation events during the period 2002–2011 with amounts more than 100mm/day and covering an area of more than 7000km^2, 13 (52%) matched with timing and location of their identified ARs.

Of practical importance are the impacts of ARs on hydrology and water resources over this region. The studies reviewed above and those by Lavers and Villarini (2013b, 2015a) and Steinschneider and Lall (2016) have taken some solid initiatives in this direction; however, these works are limited in the range of analyses performed and/or the study period. For example, Lavers and Villarini (2013b) considered the impact of ARs on floods only in terms of annual maximum floods, whereas the contribution to total precipitation was carried out in Lavers and Villarini (2015a). In these studies no attempt was made to evaluate the contribution of ARs to either peak-over-threshold (POT) floods or to extreme precipitation. With the help of Empirical Orthogonal Functions (EOFs), Steinschneider and Lall (2016) found similar spatial modes of variability in TMEs and POT flood counts. However, the magnitudes of TME contribution to POTs and extreme precipitation are still unclear, and their spatial and seasonal distributions have not been addressed thus far. Steinschneider and Lall (2015b) looked at the modes of precipitation variability, but maps showing the spatial and seasonal contribution of TMEs to extremes were not included. I also note that Steinschneider and Lall (2015b, 2016) have focused on TMEs, while the impacts of ARs are still not clear.

In all the studies cited above, another important limitation is the use of only one reanalysis product with relatively short study periods of 30–34 years. As will be discussed later in the context of results in Lavers and Villarini (2013b), the lack of long-term records, especially for seasonal analyses, casts a doubt on the statistical significance of the results. Furthermore, to my knowledge, none of the studies in the literature provided a detailed description of the climatology of ARs over the central United States.

Another important aspect related to ARs that I explore in this chapter is the relation of these storms to large-scale atmospheric modes. Several studies (e.g., Mo et al. 1997; Coleman and Budikova 2010; Harding and Snyder 2015; Mallakpour and Villarini 2016b) have linked heavy precipitation and flooding events over the central United States to the variability in large-scale atmospheric circulation modes, which are low-dimensional variables that characterize the state of atmospheric conditions. These studies suggest that changes in atmospheric modes alter the Great Plains low-level-jet (GPLLJ) and ARs, leading to changes in the frequency of heavy precipitation events over this region. For example, the negative phase of Pacific-North American teleconnection (PNA; Wallace and Gutzler 1981), characterized by contrasting pressure regions of above-normal heights over much of the eastern United States and below-normal heights over the western United States, enhances GPLLJ; this in turn leads to increasing heavy precipitation events during the warm-season (April–October) over the central United States (Harding and Snyder 2015), even though the variability of PNA is smaller in the warm than in the cold season. Although the relationship between atmospheric modes and heavy precipitation is relatively clear, the relationship between ARs and the atmospheric modes is not well known. Preliminary insights on this aspect are provided by Lavers and Villarini (2013b) who concluded that the mean sea level pressure pattern during ARs is similar to the pattern prevalent in the positive phase of the North Atlantic Oscillation (NAO), and by Steinschneider and Lall (2015b), who suggested a direct relationship between TME-based precipitation and PNA. This chapter extends the analyses to fill the gaps of linking atmospheric modes to ARs using visual inspection and statistical tools. This has important implications regarding the predictability of ARs and extreme hydrologic events such as floods. I provide more discussion on this aspect in the discussion section.

With these research gaps in mind, the objectives of this chapter are:

1. To present a long-term climatology of ARs over the central United States based on multiple reanalysis products. In so doing, I discuss the primary features of these storms, including their duration and seasonality. This has important implications for the hydrologic cycle, regional water budget and water resource management because vast amounts of moisture transport occur *via* ARs.

2. To evaluate the spatial impacts of ARs on total precipitation, extreme precipitation, and annual maximum and POT floods at the annual and seasonal scales.
3. To use multiple reanalysis products so that uncertainties resulting from different modelling and assimilation techniques can be highlighted and recognized. In all the analyses, a comparison is provided between higher and lower resolution reanalysis products.
4. To examine the relationship between ARs and three prominent atmospheric modes with the help of visual examination and statistical tools.

4.1 Data and Methods

4.1.1 Data

The atmospheric reanalysis data that are used to identify ARs are: 1) the Twentieth Century Reanalysis (V2) project (20CRV2; Compo et al. 2011), 2) the (NCEP)/National Center for Atmospheric Research (NCAR) reanalysis project (NCEP-NCAR; Kalnay et al. 1996), 3) The Japan Meteorological Agency (JMA)'s Japanese 55-year Reanalysis (JRA-55; Kobayashi et al. 2015), 4) MERRA, 5) the European Centre for Medium-Range Weather Forecasts (ECMWF) reanalysis project (ERA-Interim; Dee et al. 2011), and 6) NCEP-Department of Energy (DOE) Atmospheric Model Intercomparison Project (AMIP-II) reanalysis project (NCEP-DOE; Kanamitsu et al. 2002). The data from 20CRV2 are available from 1871 to 2012 at a horizontal grid resolution of 2º × 2º. I used all the 56 members of the 20CRV2, in addition to the ensemble mean of the 56 members. NCEP-NCAR data are retrieved from 1948 to 2013 at 2.5º × 2.5º horizontal grid resolution. JRA-55 data are obtained from 1958 to 2013 at 2.5º × 2.5º resolution. MERRA, ERA-Interim, and NCEP-DOE data are obtained from 1979 to 2013, and at horizontal grid resolutions of 0.5º × 0.667º, 0.75º × 0.75º, and 2.5º × 2.5º, respectively. To identify ARs, I retrieved q, and u and v wind components at vertical levels from surface (~1000hPa) to approximately 300hPa. All the variables are at 6-hour intervals.

To analyze the impact of ARs on precipitation, I used CPC's daily precipitation product used in Chapters 2 and 3. The daily data are available from 1948 to the present at 0.25º × 0.25º horizontal grid resolution. To examine the connection between ARs and flooding, I downloaded daily average and annual instantaneous peak discharge data from U.S.

Geological Survey (USGS) stream gaging stations. I selected stations that have at least 50 complete years of the most recent data (ending no earlier than 2010), and a continuous record having a total gap length of no more than five years. For daily averaged discharge, a year is treated to have complete data if the data are available for more than 330 days. The location of stream gaging stations is shown in the bottom panels of Figure 4.1. A total of 1567 stations were used for peak discharge (Figure 4.1, bottom-left panel) and 942 stations were used for daily averaged discharge (Figure 4.1, bottom-right panel). Overall, the stations are well distributed across the study area with a density that allows to capture the spatial variability of the AR-flooding link. Only few stations have data in the early 1900s (Figure 4.1, top panels), with a consistent coverage starting from the early 1960s. Even though I selected 50 years as the minimum record, most of the stations have a record length of 60–80 years (Figure 4.1, middle panels).

4.1.2 Methods

ARs are identified from 6-hourly IVT fields from each of the six reanalysis datasets using the algorithm in previous chapters. An important algorithmic step that is different here compared to Chapter 3 is the extended search region. In previous chapters, the search was conducted at only one latitude (40ºN) over the longitude band of 100ºW to 85ºW; here, the search is made at different latitudes (42ºN, 40ºN, 38ºN, 36ºN, and 34ºN) and extended to the east (80ºW), with the goal of identifying most of the ARs that affected the central United States. Indeed, sensitivity results (not discussed in detail here) show that about 30% additional ARs are captured by extending the search region. The threshold for each reanalysis product is different, and varies with the day of the year and the above selected latitudes. After calculating the threshold for each model, the AR identification proceeds as in the previous chapters. All the ARs identified with each latitude are then concatenated to obtain an AR time step repository.

As in Chapters 2 and 3, ARs that last for at least three time steps (i.e., are at least 18-hour long) are selected as persistent ARs (referred simply as ARs hereafter). The 18-hour persistence criterion is used to consider only the ARs that have some hydrologic impact in terms of precipitation over the central United States (see section 3.2.2). From the identified ARs, I build the AR climatology based on each of the six reanalysis products. The climatology includes important AR features, such as the time series of the frequency of

ARs, their duration, and the location of the AR major axes (collection of the latitude-longitude of maximum IVT grid points). From this climatology, we can examine the seasonal and inter-annual variability in the frequency and duration of ARs.

The next part of this study is to explore the role ARs play in the hydrology and hydroclimatology of the central United States. In particular, the focus is on the annual and seasonal impacts of ARs on precipitation and flooding. I accomplish this by computing the ratio of precipitation associated with ARs to the total precipitation from CPC. As in Chapter 3, the amount of precipitation that occurs within a 250-km area around the AR major axis is taken as the precipitation associated with an AR (or AR-related precipitation). Time series of annual AR-related precipitation is compared with total annual precipitation from CPC, taken as an average yearly precipitation in the region from 30ºN to 40ºN and from 100ºW to 80ºW. Moreover, I examine the spatial distribution of AR contributions to the total precipitation at the annual and seasonal scales.

The impact of ARs on extreme precipitation is considered in terms of the number of heavy precipitation days that are associated with ARs. At each grid point in CPC, days for which the precipitation amount exceeded the 99th empirical percentile of the daily precipitation distribution are taken as heavy precipitation days. Over the period 1948–2012, the 99th percentile corresponds to the 237 heaviest precipitation days. In terms of floods, I consider the impact of ARs on annual instantaneous peak discharge and POT floods. For POT floods, at each stream gaging station, a threshold is selected such that there are, on an average, two events per year that exceed the threshold. If there are more than two floods less than a week apart, the largest discharge value is selected. Because I have selected only those stations that have at least 50 years of data, the count of floods is at least 100 at each station. A flood event at a stream gage is considered to be associated with an AR if: 1) the station is within 4º (~ 400km) latitude and longitude of the AR major axis, and 2) the flood occurred within two days before the beginning of the AR and a week after its end. The distance and time criteria are introduced to allow for the precipitation associated with ARs to be routed through the river network. The analyses are performed at annual and seasonal scales. Here, the seasons considered are winter (December-January-February), spring (March-April-May), summer (June-July-August), and fall (September-October-November).

I examine the atmospheric controls of the frequency of ARs using three prominent large-scale atmospheric modes that have been shown to affect the precipitation across the central United States: 1) NAO, 2) Arctic Oscillation (AO), and 3) PNA. Standardized AO and PNA are obtained from CPC (http://www.cpc.ncep.noaa.gov/products/precip/CWlink/). The monthly data are available from 1950 to the present. Because studies have shown that some of the main characteristics of NAO change with seasons (e.g., the subtropical node of the North Atlantic dipole is located more to the west in the summer than during the winter), I use the mobile NAO index based on Portis et al. (2001). To gain insights on which modes could be physically more relevant to precipitation and ARs, I plot correlation maps between precipitation and index values of these modes for the four seasons. Further, I compare the 500hPa geopotential height anomalies during ARs with the anomalies during the positive or negative phases of these modes. Anomalies are computed from 20CRV2 data with the daily climatological mean taken from the year 1950 to 2012. Based on the results from the above analyses, I move towards the modeling of AR activity over the central United States in terms of climate modes. For this, I use Poisson regression, where the number of ARs in a season is modelled as a Poisson process conditional on covariates such as PNA, AO and/or NAO indices. Poisson regression is implemented for each season separately. More specifically, the frequency of ARs is modelled in the season for a given year using PNA, AO and/or NAO indices as predictors (via a logarithmic link function). The significance and the magnitude of the coefficients relating the covariates to the average number of AR events quantifies their effects on the frequency of ARs.

4.2 Results

4.2.1 AR climatology

Figure 4.2 shows the time series of the number of ARs from different reanalysis products. Long-term AR frequency from 20CRV2, with the range from its 56 members, is presented in the top panel along with two other long-term products (NCEP-NCAR and JRA-55). From this plot, the average annual frequency of ARs is about 26 with large year-to-year variations, and the frequency can range from as low as 6 to as high as 35. The uncertainty (range) of the frequency of ARs in the 56 members is in general higher before

1940 than after it, with mean differences between the maximum and minimum frequency equal to 9.9 from 1871 to 1940, and 7.7 from 1941 to 2011. The potential effects of the inhomogeneity in 20CRV2 can be responsible for these results (e.g., Ferguson and Villarini 2012) and for the impacts in the trends over the 1871–2012 period: the trend from 1871 to 1940 is positive and significant at the 1% significance level, while this is not the case from 1941 to 2012. Lombard's test (Lombard 1987; Nayak and Villarini 2016), a rank-based non-parametric change-point test, identified a shift in the mean of the annual frequency of ARs in the year 1905 at the 1% significance level (19 ARs per year in 1871–1905 period and 23.6 in 1906–2012 period). Ferguson and Villarini (2012) also detected changes in the period 1905–1920 during the winter season for different atmospheric variables over the central United States. The results of their study suggest that the inhomogeneities could be due to the sparse observational network in the late 19th to mid-20th century years. The frequency from different products is shown in the bottom panel of Figure 4.2 for the most recent period of 1979–2013, highlighting large annual variations in the frequency of ARs, which I will examine further later in this chapter in the context of atmospheric modes. All the reanalysis products tend to agree with each other, and none of them shows consistent over- or under-estimation of the frequency of ARs. This is true for 20CRV2 as well, which assimilates only observations of surface pressure and temperature, and sea-ice distribution, and not vertical atmospheric observations from satellite, aircraft, radiosondes, etc., as is done in the other reanalysis products. A more concise comparison among the different products is provided in Figure 4.3, which shows the percentage of persistent AR timesteps present in the "reference" model (in rows) that are also observed in the "validation" model (in columns) for the period 1979–2012. Clearly, the higher spatial resolution models perform better: the higher resolution models (MERRA and ERA-Interim) are able to capture most of the ARs identified in the lower resolution models (JRA, 20CRV2, NCEP-NCAR, NCEP-DOE), while the lower resolution models struggle to capture ARs identified in the higher resolution models. For example, in the first row only 67% of MERRA AR timesteps are identified in NCEP-NCAR, while in the corresponding last row, 83% of NCEP-NCAR ARs are observed in MERRA. The performance of 20CRV2 is generally acceptable, although somewhat smaller fractions of its AR timesteps are observed in the other models.

Figure 4.4 shows the time series of the annual mean and annual maximum duration of ARs in 20CRV2. The yearly mean and maximum durations are about 36 and 82 hours, respectively (Figure 4.4, top panel). As can be expected, the annual mean duration shows less variability (Coefficient of Variation: CV = 0.11); but the maximum yearly duration has larger year-to-year variability (CV = 0.24) with ARs lasting as long as 174 hours (~7 days). The frequency histogram of all ARs (bottom-left panel) shows that the majority of ARs are shorter than 60 hours (~2.5 days), with the 95th percentile equal to 72 hours. The minimum duration of the longest ARs in a given year is about 48 hours, which means that each year an AR remains over the central United States for a minimum of 2 days. The results based on 20CRV2 are fairly consistent with the results from the other reanalysis products (not shown here). In most of the products, the longest duration ARs in the most recent decades occurred in the years 1990 and 2012 lasting for 174 hours (~7 days) and 138 hours (~6 days), respectively. These two ARs occurred on 8–15 March 1990 and 17–21 March 2012, respectively. During these days, large amounts of rainfall with magnitudes in excess of 25mm/day were observed over a large areas in Alabama and northern Georgia in 1990, and Louisiana, Arkansas, Oklahoma and southern Missouri in 2012 AR.

The seasonality of ARs is shown in Figure 4.5. Winter (summer) is the most (least) active season, with a total of 1445 (158) ARs from 1871 to 2012. Spring and fall have experienced 930 and 657 ARs, respectively. The seasonal distributions show that the maximum frequency of ARs during a given winter can be as high as 19 (Figure 4.5, top-left panel), while for the summer it is only 6 (Figure 4.5, bottom-left panel). Table 4.1 shows the details of the seasonality in 20CRV2 and compares the results across other reanalysis products. The seasonality of AR frequency is consistent across all the reanalysis products, with the highest frequency in winter and the lowest in summer. Based on the two highest resolution products (MERRA and ERA-Interim), on average there are 26 ARs each year over the central United States. Table 4.1 also shows the maximum number of ARs observed based on all the reanalysis products in their respective period of records, with the higher resolution products (MERRA and ERA-Interim) showing higher annual AR frequencies than the other four lower resolution products. It can be noted that as the spatial resolution decreases (from the top row to the bottom row), the frequency of ARs decreases, suggesting that higher resolution products are more apt in identifying ARs. One possible

reason for this could be the better spatial continuity in IVT fields offered by higher resolution models; however, further research is required to comprehensively answer this question.

4.2.2 Impact on precipitation

The contribution of ARs to annual precipitation is shown in Figure 4.6. Annual precipitation over the study area varies approximately from 800mm to 1500mm, with an average value of 1109mm over the period 1948–2013. Generally, years with high frequency of ARs tend to have larger precipitation magnitudes. AR-related precipitation (Figure 4.6, 3rd panel from the top) shows better correspondence with the annual precipitation. In a linear regression model with AR-related precipitation as the only explanatory variable for annual precipitation, the coefficient of determination is high (0.52; Pearson correlation coefficient of 0.72), suggesting that more than 52% of the variance in the annual precipitation over the central United States is explained by AR-related precipitation. Generally, the large precipitation years (e.g., 1973) have larger contributions from ARs. The bottom panel in Figure 4.6 shows that ARs provide significant contributions to total precipitation on a yearly basis, and the fractional contribution can be as high as 45%. It is worth noting that this contribution is an average over the central United States taken here as the region 30°N–40°N and 100°W–80°W; therefore the contribution to specific locations can be higher. In 1993, for example, regions outside the study domain such as Iowa and northern Illinois, received large amounts of rainfall on the order of 10mm/day (figure not shown); only a part the study domain observed high rainfall, resulting in a contribution of about 30% for the summer of 1993. All the products and the members of 20CRV2 suggest a similar pattern of year-to-year contributions. Similar results across all the products provide additional evidence regarding the AR contributions over the central United States.

Although Figure 4.6 provides important insights into the AR contributions to total precipitation over this area, it is necessary to understand how these contributions vary spatially and across different seasons. Figure 4.7 shows the fractional contribution of ARs across the central United States at annual and seasonal time scales. At the annual scale, the fractional contribution can be as high as 30%, and a large area in the middle of the study region receives contributions in excess of 25%. Winter has the highest fractional

contributions, with a large part of the central United States receiving more than 60% of winter precipitation from ARs. These percentages tend to be lower in fall and spring, with less than 10% in summer. The summer contribution over the study region matches reasonably well with the results in Steinschneider and Lall (2016), who also show a 0%–10% TME-based contribution. In their study, however, particularly high TME contributions (exceeding 70%) were observed over the northern regions beyond 40°N; however, the authors note that this could an overestimation due to the wet bias more prominent in summer specific humidity of ERA-Interim, which was used to compute the TME-based precipitation. The fractional contributions from high spatial resolution models (i.e., MERRA and ERA-Interim) are in general higher (see Figures 4.8–4.12). The annual fractional contribution is 30–40% over a large area and more than 60% for winter. In addition, the areal extent of the higher contributions is larger in these products. In the results of the AR climatology (Table 4.1), lower resolution products showed marginally lower AR frequencies, which potentially led to the underestimation of the AR contribution to the total precipitation. This could be important for AR impact analysis. Many studies have used low-resolution reanalysis products for understanding the role ARs play in precipitation and water resources; given these results, I recommend the use of high-resolution products for AR impact assessment whenever possible. These results are similar to those by Lavers and Villarini (2015a), which are based only on ERA-Interim reanalysis data from the year 1979 to 2012. Here I focus on a longer period of record (1948–2012) and use six reanalysis products. Because the reanalysis products are not observations, the use of multiple datasets allows us to compare and contrast them, providing robustness to our conclusions.

I also consider the contribution of ARs to precipitation extremes. Figure 4.13 shows the seasonality of the highest 1% daily precipitation events. A contrasting pattern is observed between summer and the remaining seasons. Summer has the highest frequency of extreme events over most of the areas in the northern part of our study domain, including all of the upper Mississippi River Basin and much of the Missouri River Basin. In the southern and southeastern United States, the frequency is unevenly distributed among the remaining three seasons depending on the location. The fractional contribution of ARs to the precipitation extremes at the annual and seasonal scales is shown in Figure 4.14.

Annually, over a large area, more than 40% of extreme precipitation events are associated with ARs. The percentage is smaller in the northern parts where most of the extreme precipitation events occur during the summer. More than 70% of winter extreme events over much of the central United States are associated with ARs. Spring and fall also show large fractions of extreme precipitation events linked to ARs.

4.2.3 Impact on floods

The fraction of annual maximum and POT flood events associated with ARs are shown in Figure 4.15. ARs can be responsible for more than 70% of the annual maximum peaks over large areas of the central United States, including Ohio, Tennessee, Alabama and the areas in the lower Mississippi River Basin. There is a strong contrast in the AR fractional contributions across the two sides of the Appalachian Mountains, with higher contributions (more than 80%) on the west side and significantly lower contributions (less than 40%) on the east side. This suggests that the Appalachian Mountains act as a flood generating agent in western regions, due to the potential for upslope transport of moisture, and as a barrier to the moisture transport to the eastern regions. Similar to what was found for the annual maxima, ARs provide major contributions to POT floods, with more than 70% of the events associated with these storms over a large area of the central United States. As can be expected, the structure of the region showing high percentages of POT floods resembles the storm track of extratropical cyclones over this area. In essence, the two plots suggest that ARs have a major effect on the long-term flooding across the central United States.

As shown for precipitation, the effects of ARs on extremes is not constant during the year but exhibits a marked seasonality. This holds true for flooding. The seasonality of flooding (Figure 4.16) shows that spring is the most active season over almost the entire central United States, with more than half of the POTs occurring in this season. The northern part of our domain receives nearly all POTs during the spring season due to snow melt and rain-on-snow events in early spring (Villarini et al. 2011). Winter is also an active season for floods over our region, with higher fractions of annual peaks and POT floods associated with AR (Figure 4.15). For detailed information regarding the seasonality of flooding, consult Villarini (2016) and references therein.

The seasonal contribution from ARs to POT floods is presented in Figure 4.17. I focus only on those stations that have more than 20 POT floods occurring in a given season. The

seasonal contribution from ARs to POTs is high for all the seasons except for summer, which, as we have seen earlier, is the least active flood season over much of the study region. Almost all the POT floods in winter and fall over the area from Michigan to northern Georgia are associated with ARs. In spring, the fractional contribution over most of the central United States is more than 50%. These results suggest that most of the floods over the central United States are governed by ARs. Long-term streamflow and AR records are particularly useful in delineating the areas that are vulnerable to ARs. The results on seasonal impacts here are in reasonable agreement with the results in Lavers and Villarini (2013b), except for some spatial discrepancies which may be attributed to differences in AR identification algorithm, the reanalysis products, and study period. The seasonal contributions in Lavers and Villarini (2013b), however, are based on small sample size of floods—for most of the stations, the number of events evaluated for AR contribution in winter and spring were less than 15, in summer less than 10, and in fall less than 5 (see Figure 3 of Lavers and Villarini (2013b)). With these small sample sizes, the statistical significance of the results is likely not large. In this study, in any seasons, only stations that have at least 20 flood events are evaluated for AR contribution, providing robustness to the present results.

4.2.4 Relation of ARs with large scale atmospheric modes

An important aim of this paper is to provide a link between large-scale atmospheric features and the frequency of ARs over the central United States. For this, I first consider the relationship between precipitation and the three atmospheric modes at the seasonal scale. Figure 4.18 shows the Pearson's product-moment correlation between seasonal precipitation and each of the three atmospheric modes PNA, NAO, and AO. The PNA index has a strong negative correlation in winter and fall over much of the central United States, west of the Appalachian Mountains. Moving from west to east along the Appalachian Mountains, there is an abrupt change in correlation from strong negative to zero or mild positive correlations. AO shows strong positive correlation in winter and negative correlation in the summer. NAO has moderately positive correlation values during winter over the western parts of the central United States. In summer, strong positive correlation is present between AO, NAO and precipitation over the south-eastern parts of the central United States. The contrasting relations among the different seasons suggest

that these modes may not provide a strong signal at the annual scale, but the potential describe precipitation is high at the seasonal level.

To further examine the physical connection between these atmospheric modes and AR activity, 500hPa geopotential height anomalies are plotted during ARs and compared with anomalies during the negative phase of PNA, and the positive phase of AO, and NAO (Figure 4.19). A dipole is present in the height anomalies during ARs (left column) over the United States. Such dipole is generally a part of a larger planetary wave of atmospheric circulation that oscillates over most of the longitudes in mid-latitude regions. Studies suggest that these quasi-stationary wave patterns are particularly apparent during extreme weather events over the Northern Hemisphere (Petoukhov et al. 2013). For instance, by examining the 300hPa meridional (v-) wind component of the two most persistent ARs of 1990 and 2012 mentioned earlier, I find that both the ARs may have been accompanied by planetary waves of wavenumbers 5 and 6, respectively (Figure 4.20). However, further in-depth analyses are needed to validate the finding. A high pressure region (ridge) is located over much of the eastern United States and a prominent low pressure region (a trough) is located over the central and western United States. A similar height pattern is observed in the work by Moore et al. (2012) who studied a major flooding event associated with an AR over the central United States, in Chapter 2, and more generally by Mallakpour and Villarini (2016b). The primary feature of this pattern is that the ridge over the eastern United States near the Atlantic Ocean coupled with a trough over the Great Plains and the western United States maintain poleward advection of warm and moist air from the Gulf of Mexico and sometimes from the Caribbean, into the central United States—this results in ARs over the central United States. A similar pressure pattern over the western North Atlantic, the North Atlantic Subtropical high (NASH), has also been shown to significantly modulate the meridional moisture transport over the central and eastern United States (Li et al. 2010; Li et al. 2012). This anomaly pattern is noticeable for all the seasons, though it is weaker in the summer. When I compare the AR anomaly pattern with atmospheric modes, I see that the anomaly pattern of the negative phase of PNA closely resembles the AR pattern. The positive phases of NAO and AO show height patterns similar to each other. In the positive NAO and AO phases, positive height anomalies can be observed over the eastern United States, but unlike ARs and PNA, height anomalies over much of the

United States are positive (3rd and 4th columns). The positive anomalies over the United States reduce the horizontal pressure gradient between the eastern and western United States, inhibiting the GPLLJ and southerlies (assuming simple geostrophic wind balance). Note that the positive anomaly over the western United States is generally smaller during AO than during NAO. Overall, for all the three indices, the patterns are the most (least) prominent in winter (summer).

I used Poisson regression to approximately quantify the effect of the atmospheric modes on the frequency of ARs. Based on the findings in Figure 4.19, all the three modes (PNA, NAO, and AO) are used as covariates to model the seasonal frequency of ARs. With these three covariates, all the seven possible combinations, in addition to the intercept-only model term, were investigated for each season. First, I selected models for which all the covariates are significant, and then among this subset I selected the best model based on the lowest Akaike Information Criteria (AIC; Akaike 1974). The results are summarized in Table 4.2.

For winter, PNA and AO have significant negative and positive coefficients, respectively, consistent with the results in Figure 4.19. This suggests that the two modes can have large influence in regulating the year-to-year frequency of ARs. For example, in the winter, a unit decrease in the standard PNA index can increase the frequency of ARs by about 25% ($e^{0.22}$); similarly, a unit increase in the AO index can increase the frequency of ARs by about 15%. In Table 4.2, PNA also shows major effects on ARs in spring. The p-values for PNA and NAO during fall are close 0.10 suggesting a possible link between these two indices and the frequency of ARs in fall season as well. To examine how robust these modeling results are, I compare the observed and modeled frequencies of ARs using both in-sample and out-of-sample predictions (Figure 4.21). The out-of-sample estimates are based on the leave-one-out criterion in which the model is fitted based on all the data except one data point. In winter, the model based on PNA and AO captures the year-to-year variability in the frequency of ARs well. The same is true for spring, even though there is much less year-to-year variability. The in-sample and out-of-sample estimates are very similar, which suggests that our results are robust and that the coefficients are not affected by potential outliers.

4.3 Discussion

The development of long-term multi-product-based AR climatologies accomplished in this chapter is a major step towards understanding the hydrology and hydroclimatology of the central United States. In studying the impacts of ARs on annual precipitation, I found that the seasonal AR contributions are 10–60% depending on the season and location. A recent study by Steinschneider and Lall (2016) compared seasonal TME-based precipitation with total precipitation from CPC. The TME-based precipitation is generally smaller than the AR-related precipitation presented here over most of the central United States. For winter, for example, the TME contribution is less than 25%, whereas the AR contribution to the winter precipitation in this study is more than 45%. The reason for this discrepancy lies in the difference in the definitions of ARs and TME discussed earlier. Therefore, in terms of the hydrologic impacts over the central United States, ARs play a larger role than TMEs.

Important differences are observed in the impacts of ARs on extreme precipitation and flooding. The fractional contributions of ARs to extreme precipitation events are much smaller than what I found for annual instantaneous flood peaks or POT floods (compare Figures 4.14 and 4.15). For example, if we consider the states of Indiana, Kentucky, Tennessee and Mississippi, 20%–60% of the annual extreme precipitation events are related to ARs; in contrast, 60%–70% of the flood events (peaks and POT floods) are associated with ARs. Over the central and eastern United States, more than two-thirds of extreme precipitation events are a result of mesoscale convective systems (~100km in length, MCS), and mostly occur in the summer months (Maddox et al. 1979; Stevenson and Schumacher 2014). On the other hand, ARs cause widespread rainfall, and generally persist longer than one day (often more than two days; Figure 4.4), which leads to high discharge and flooding.

The seasonal and sub-seasonal prediction of precipitation extremes based on large-scale atmospheric features is an emerging concept, particularly in the context of non-stationary climate. Some strides have been made in this direction in recent studies (e.g, Gregersen et al. 2013; Renard and Lall 2014; Steinschneider and Lall 2015a). In this chapter, I explored this topic in the context of seasonal characterization of AR frequency, and found that PNA, NAO and AO can be useful predictors. The seasonal modeling of ARs

can be improved by incorporating additional relevant modes, or by considering pertinent atmospheric and oceanic fields (rather than single modes) as suggested by Renard and Lall (2014).

Steinschneider and Lall (2015a) developed hierarchical models for winter precipitation extremes over northern California. The frequency of extreme events was modelled in a Bayesian hierarchical framework conditioned on the quantity of TME moisture entering the study area. The results showed that the model that included TME performed better in out-of-sample predictions as compared to the models that did not incorporate TME information. As we have seen in this study, large fractions of extreme precipitation and flood events are associated with ARs; ARs themselves are predictable from large-scale atmospheric modes with reasonable skill, particularly in the two most active flood seasons (winter and spring). This naturally suggests hierarchical/multi-level models for flood frequency conditional on the frequency of ARs, which itself is conditional on the climate modes. In essence, an additional level would be added to the model in Steinschneider and Lall (2015a). These models inherently assume that the large-scale climate modes manifest themselves by modulating the frequency of ARs, and ARs are directly responsible for the annual variations in the frequency of floods over the region. The assumptions are realistic, as can be inferred from our results. In Figure 4.18, I saw that the effect of the atmospheric modes is very much location-dependent. Therefore, additional improvements can be made in the models by incorporating spatial and temporal signatures of large-scale climate features. Based on these results, in the next chapter I will develop a Bayesian hierarchical non-stationary spatio-temporal model for the frequency of precipitation extremes over the central United States.

In the 21st century climate model simulations, IVT is expected to increase by more than 20% over the United States and the surroundings oceanic regions (Lavers et al. 2015); moreover, the already apparent westward shift and increased intensity of summer NASH, and higher North-South movement in its western ridge (Li et al. 2010; Li et al. 2012) are expected to be exacerbated. In this context, the results presented here can have large implications. We have seen that ARs have a direct and strong link with extreme precipitation and flooding events; given the projected changes in IVT and NASH, it is

reasonable to expect an increase in the frequency of extreme precipitation and flooding events, controlling for other potential drivers of extremes precipitation and flooding.

4.4 Summary and Conclusions

This study presented a comprehensive analysis of ARs over the central United States. A long-term AR climatology is developed from six state-of-the-art atmospheric reanalysis products. On average, about 26 ARs affect the central United States each year, although the year-to-year variability in the frequency is large. Winter is the most active season in terms of AR activity (the frequency is more than 10 per season), followed by spring (~ 8 per season) and fall (~6 per season). In summer, ARs are rare (the frequency is less than 2 per season). Most ARs last for less than 3 days, but long-duration ARs (lasting for a week) occurred in the past. The AR climatology is similar across all the six reanalysis products considered here, although a slightly larger frequency of ARs is observed in products with higher spatial resolution.

ARs have significant effects on the hydrology of the central United States. On average, ARs account for about 30% of the total annual precipitation, and the year-to-year variability in total precipitation can be largely explained by the variations in AR-related precipitation. In terms of seasonal contributions, winter receives nearly half of its total precipitation during ARs. Summer, on the other hand, has only less than 10% of its precipitation associated with ARs. The impact of these storms is more pronounced when focusing on extreme precipitation and flooding. About 20–70% of the highest 1% daily precipitation events are associated with ARs, although the fraction is season- and location-dependent. The fractional contribution of ARs is even higher for floods. Over a large portion of the central United States, more than 70% of the flood events are associated with ARs. The results for instantaneous peak discharge and POT floods are similar. Large fractions of flood events in the two most active flood seasons (winter and spring) are related to ARs, supporting the notion that the seasonality of floods over the central United States is largely governed by ARs.

Given the large impacts ARs have on hydrology, seasonal forecasts of the frequency of ARs can be extremely valuable. Depending on the season, I found that large-scale atmospheric modes (PNA, NAO, and AO) can have significant effects on the frequency of

ARs. In particular, PNA is useful in explaining the yearly variations in AR frequency for winter, spring and fall seasons. I quantified the effects of the atmospheric modes on the frequency of ARs using Poisson regression. The results showed that a unit decrease of standardized PNA index can increase the frequency of ARs by about 25% in winter. Additionally, PNA and NAO could potentially be important predictors in fall. None of the three modes showed significant effect on the AR frequency in summer, which is also the season with the lowest AR activity. Therefore, improved forecasting of these climate modes can lead to improved forecasting of ARs and associated impacts during the cold season.

4.5 Figures Chapter 4

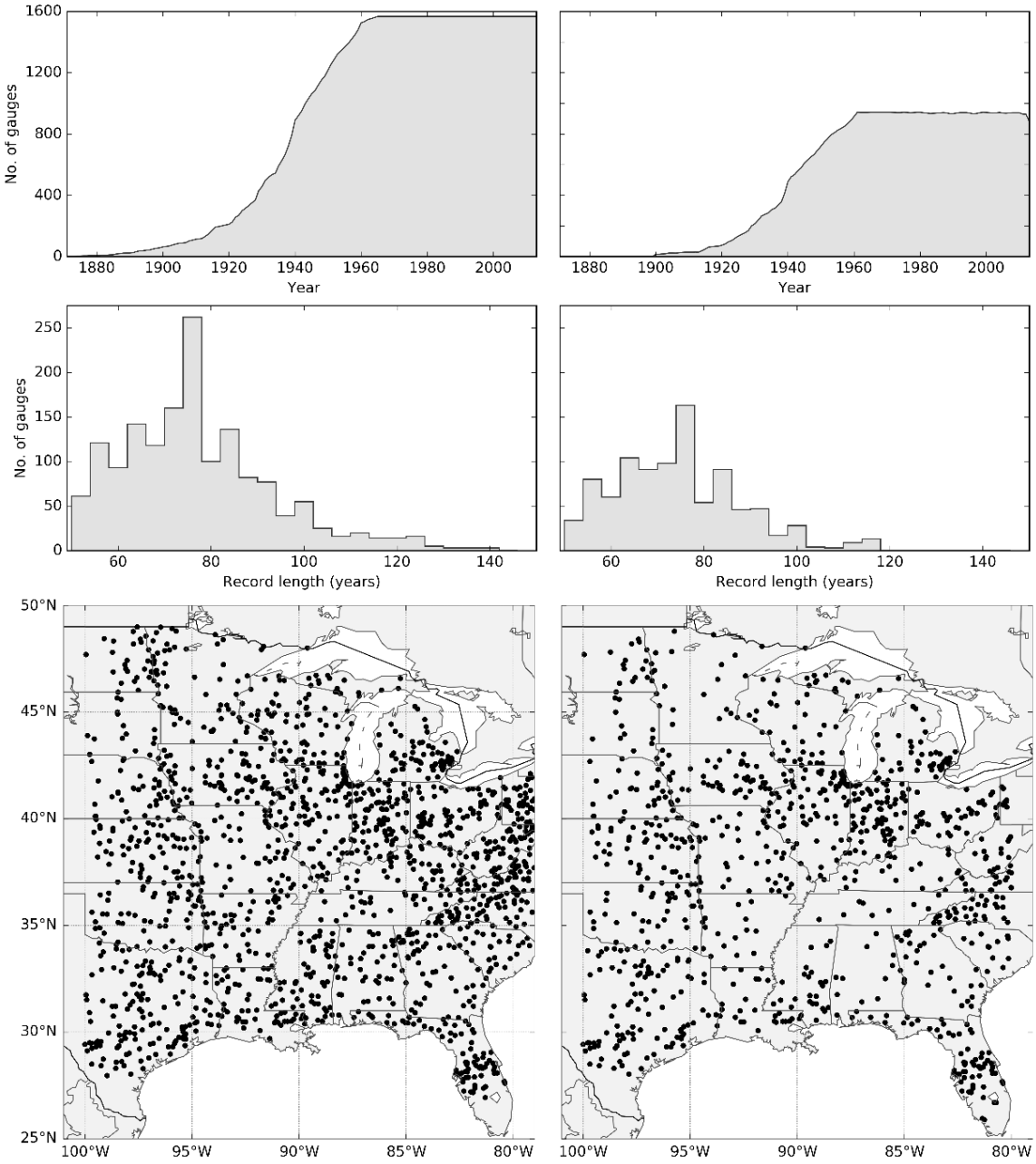

FIG. 4.1: The distribution of the USGS stream gaging stations selected for the study. Stations for annual instantaneous discharge peaks (daily averaged discharge) are shown in the left (right) panels. The top panels show the number of stations with data available

during a given year. The middle panels show the histograms of record lengths for all the stations. The bottom panels show the location and the spatial distribution of the stations. Note that while several of the stations are regulated to varying degrees, regulated and unregulated stations are treated in the same way in the analyses.

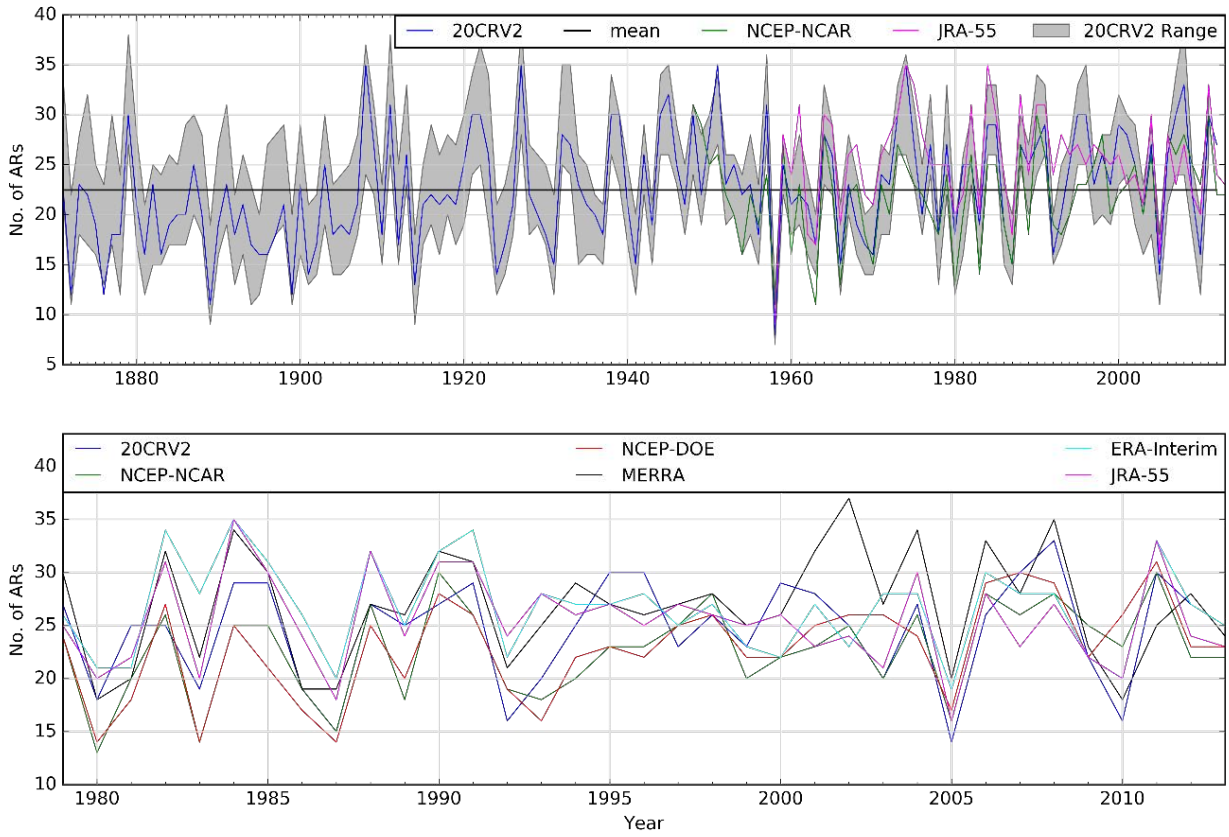

FIG. 4.2: Time series of the annual frequency of ARs. Top panel: yearly frequency (count) of ARs based on 20CRV2, NCEP-NCAR, and JRA-55. Also shown in this panel are the climatological mean from 20CRV2 (black horizontal line) and the range from 56 members of 20CRV2 (gray shaded area; occasionally, at some grid points the data in some members are missing). Bottom panel: yearly frequency of ARs based on six different reanalysis products (indexed by color; for 20CRV2 the ensemble mean is used) for the most recent period 1979–2013.

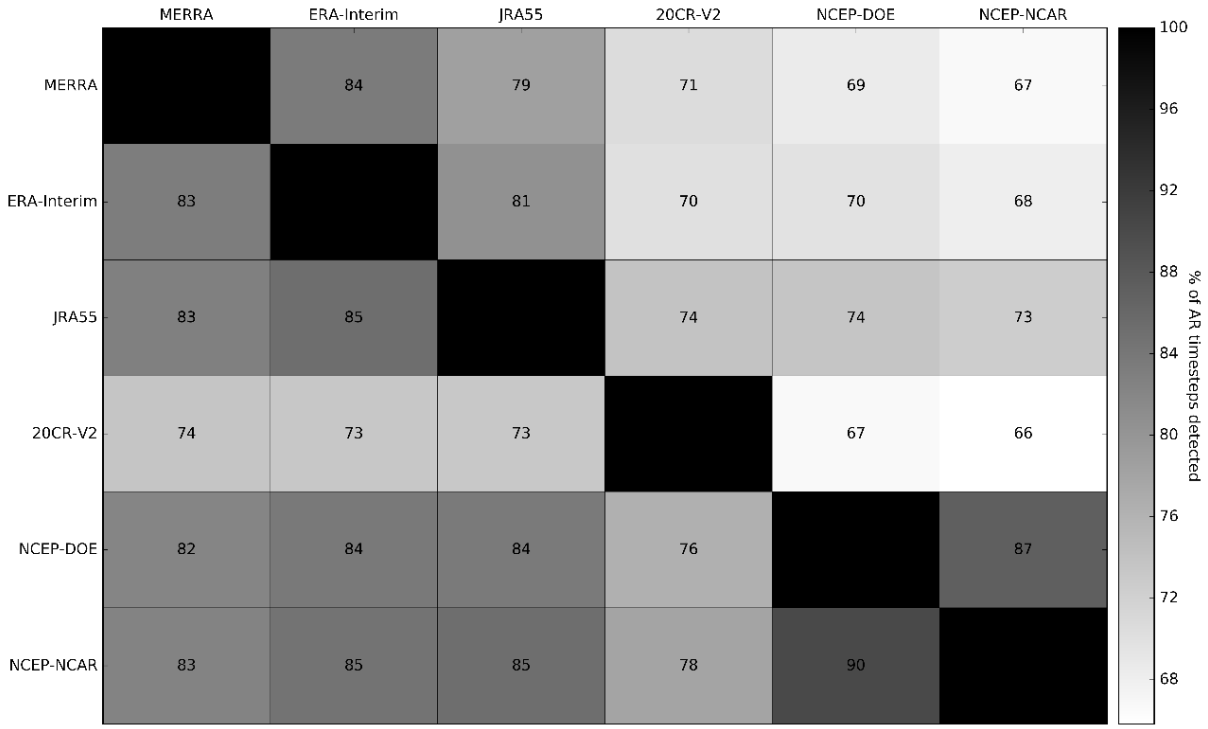

FIG. 4.3: Comparison of different products in reproducing AR frequency. Rows represent the "reference" product and columns represent the "validation" product. The numbers and the color scale represent the percentage of AR timesteps that are present in the reference model and are also observed in the validation model. The comparison is performed for the common period 1979–2012.

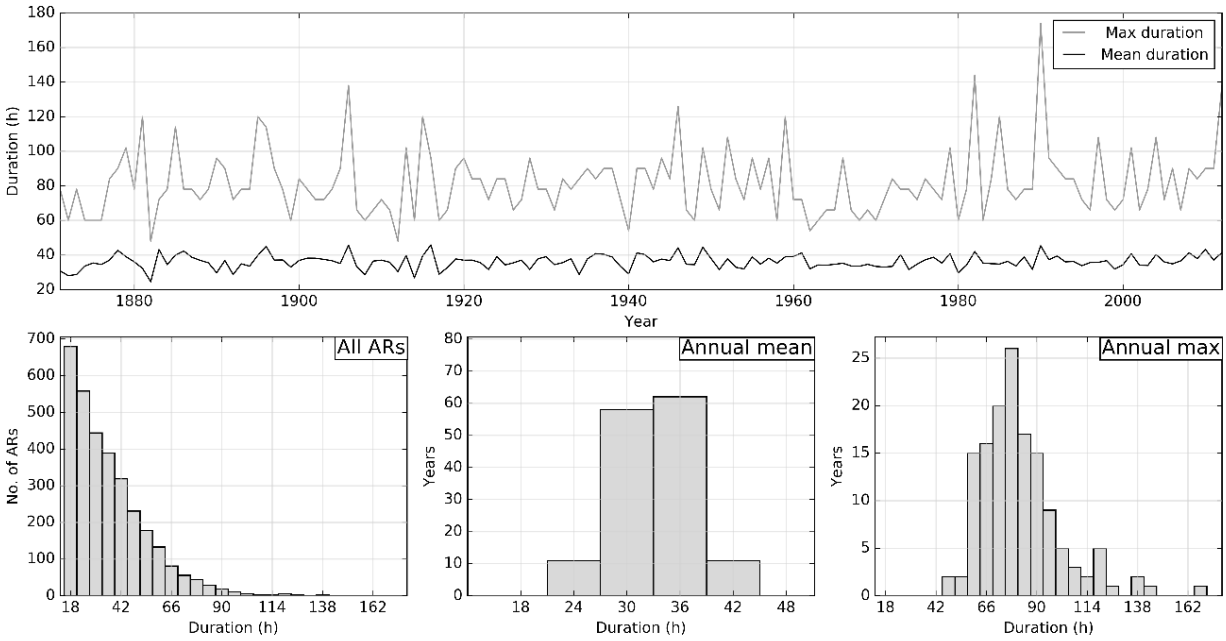

FIG. 4.4: Duration of ARs based on 20CRV2. Top panel: Time series of annual mean and maximum duration of ARs. Bottom panels: frequency histogram of the duration of all ARs (left), their annual mean (middle) and annual maximum (right) duration.

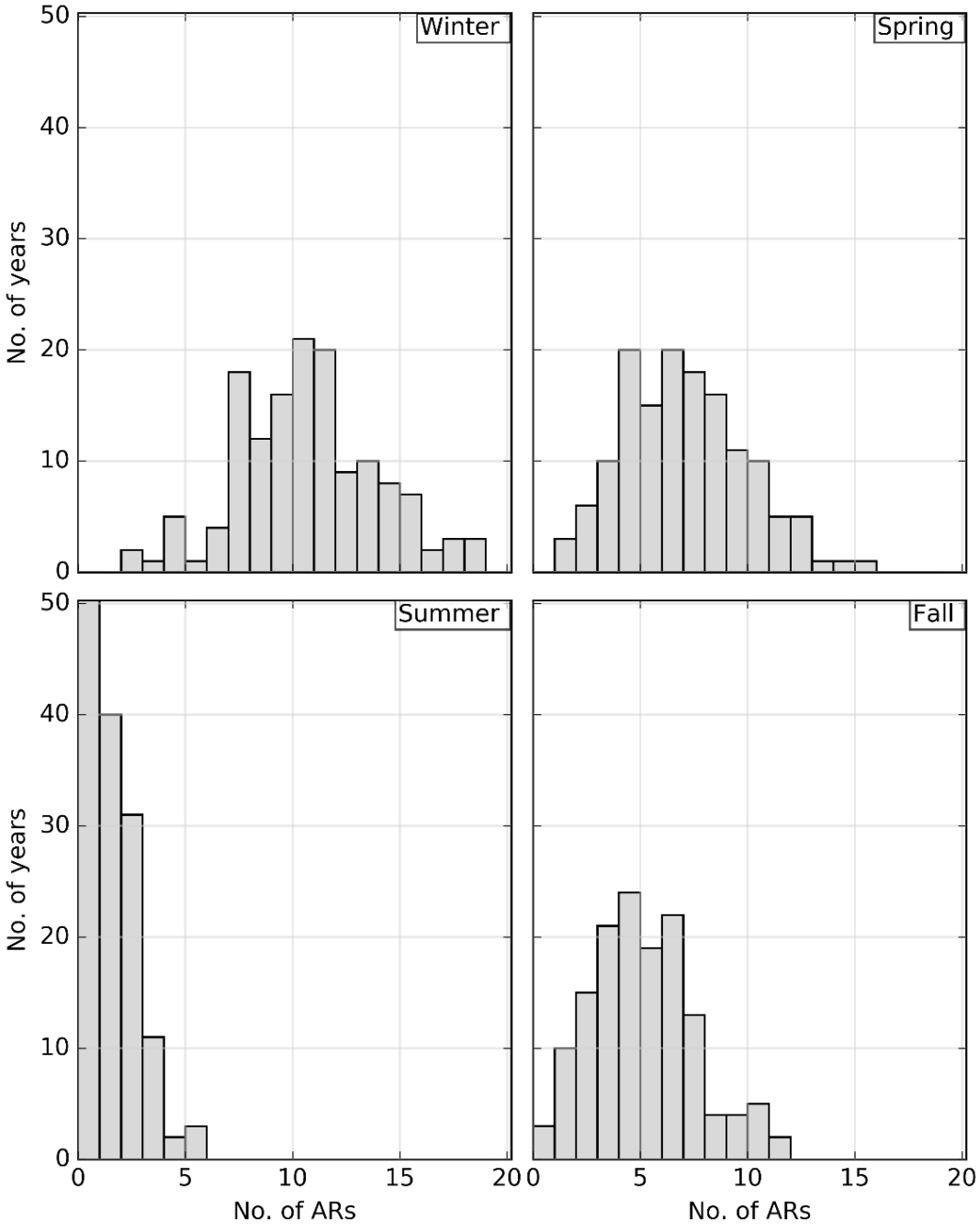

FIG. 4.5: Seasonality of ARs based on 20CRV2 over the 1871–2012 period. There are 1445 ARs in winter, 930 in spring, 158 in summer, and 657 in fall.

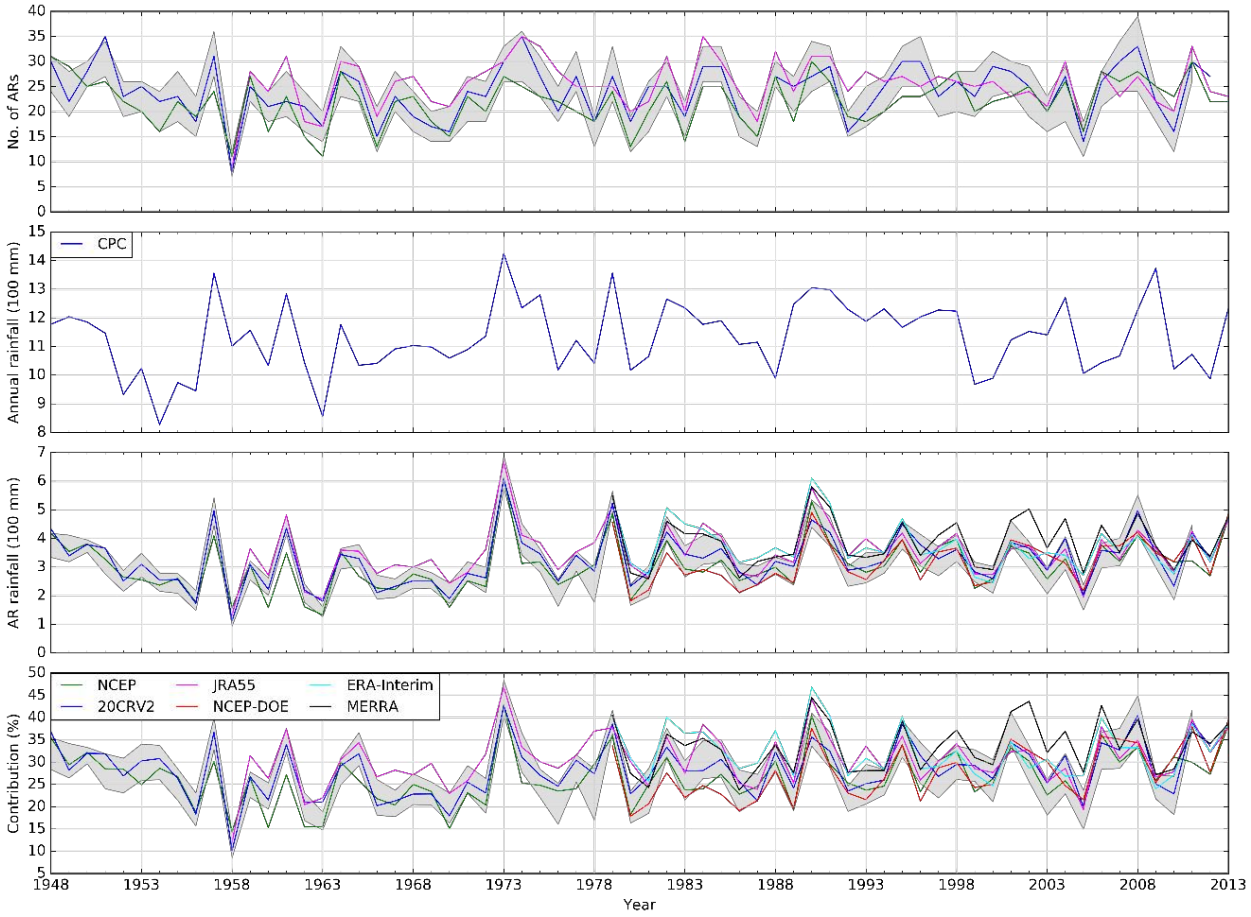

FIG. 4.6: The top panel shows the frequency of ARs from different reanalysis products (indexed by color). The shaded region shows the range of frequency from the 56 members of 20CRV2. Second panel from the top: total annual precipitation over the central United States (defined as the region 30°N–40°N and 80°W–100°W) using CPC data. Third panel from the top: AR-related rainfall from all the products (indexed by colors). The light grey shaded region is the range of AR-related rainfall from the 56 members of 20CRV2. Bottom panel: similar to the 3rd panel from the top, but it refers to the fractional contribution to annual precipitation from ARs.

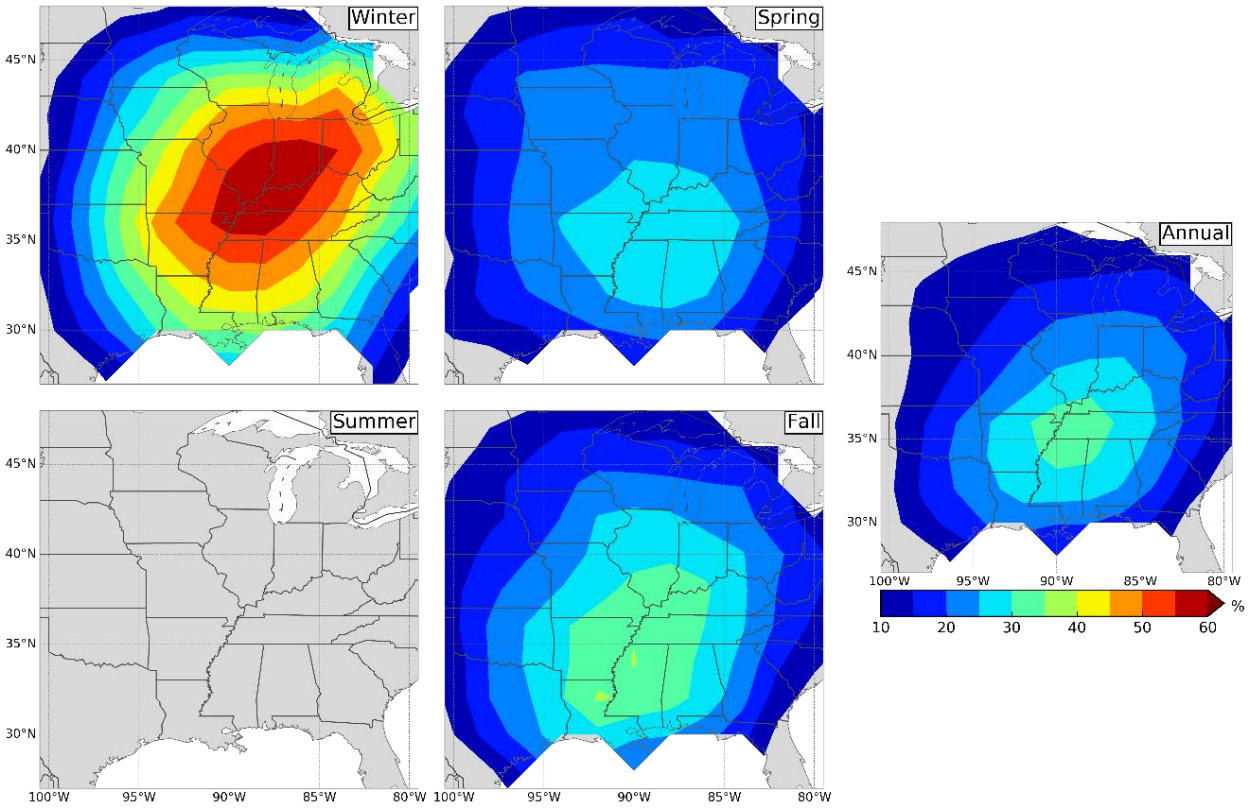

FIG. 4.7: Spatial distribution of the fractional contribution of ARs to total precipitation at the annual and seasonal scales based on 20CRV2 for the period 1948–2012. For clearer presentation, the percentages are plotted on 20CRV2 spatial grid rather than finer CPC grid. Although this has smoothing effects, the fractional contributions are not substantially different.

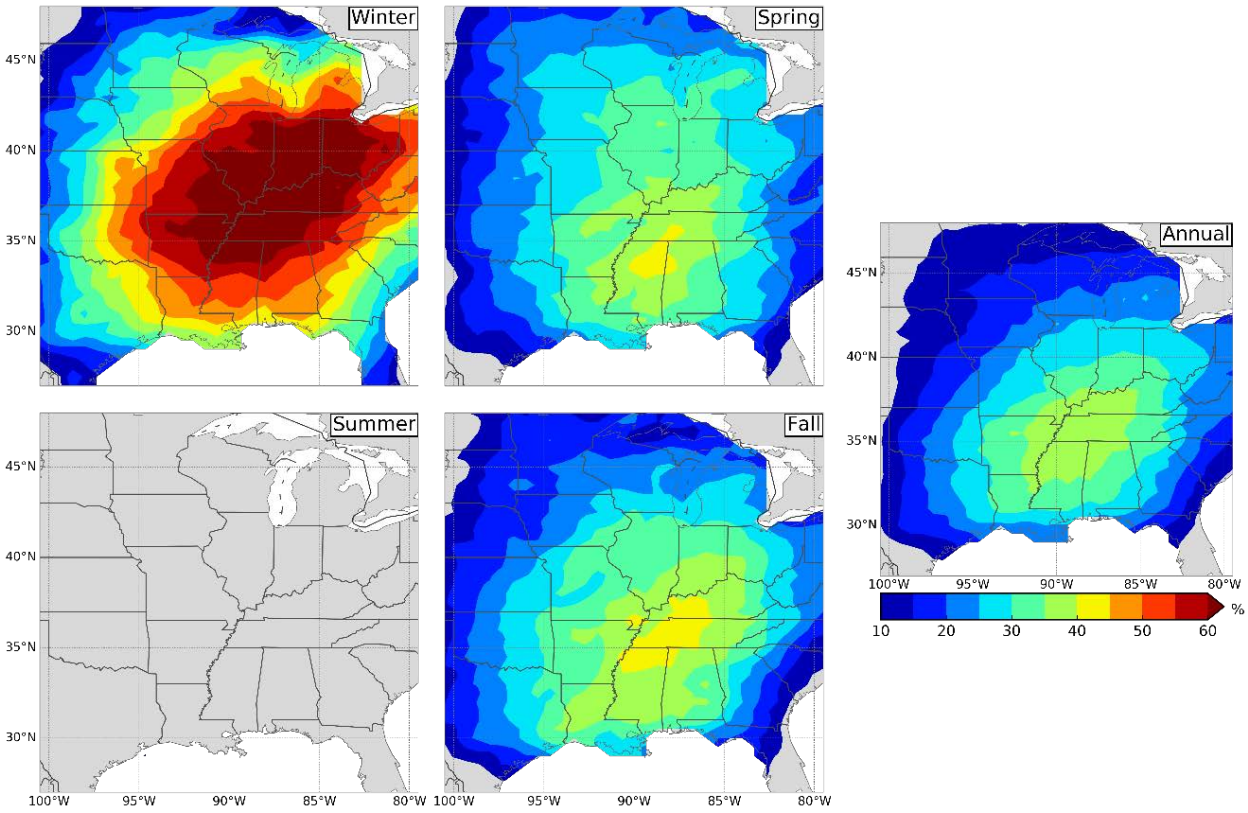

FIG. 4.8: Same as FIG. 4.7 but for MERRA.

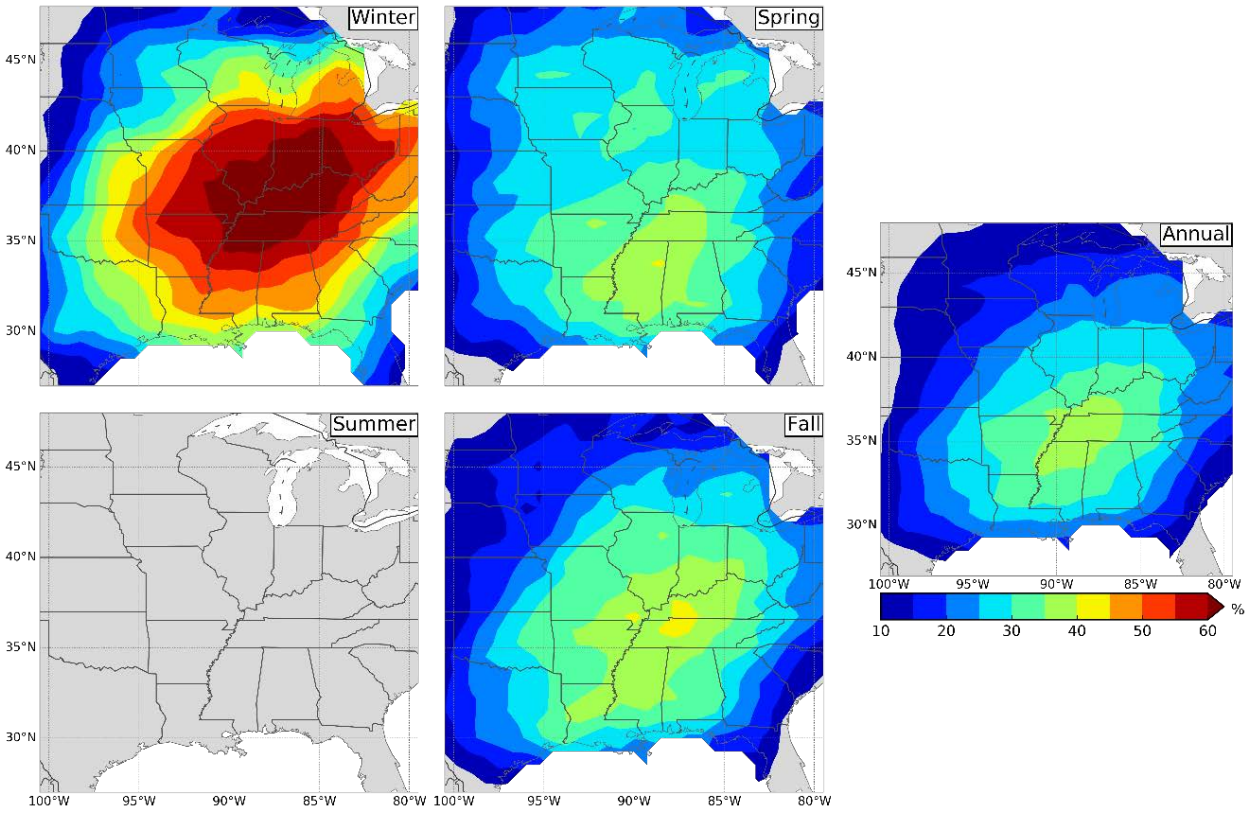

FIG. 4.9: Same as FIG. 4.7 but for ERA-Interim.

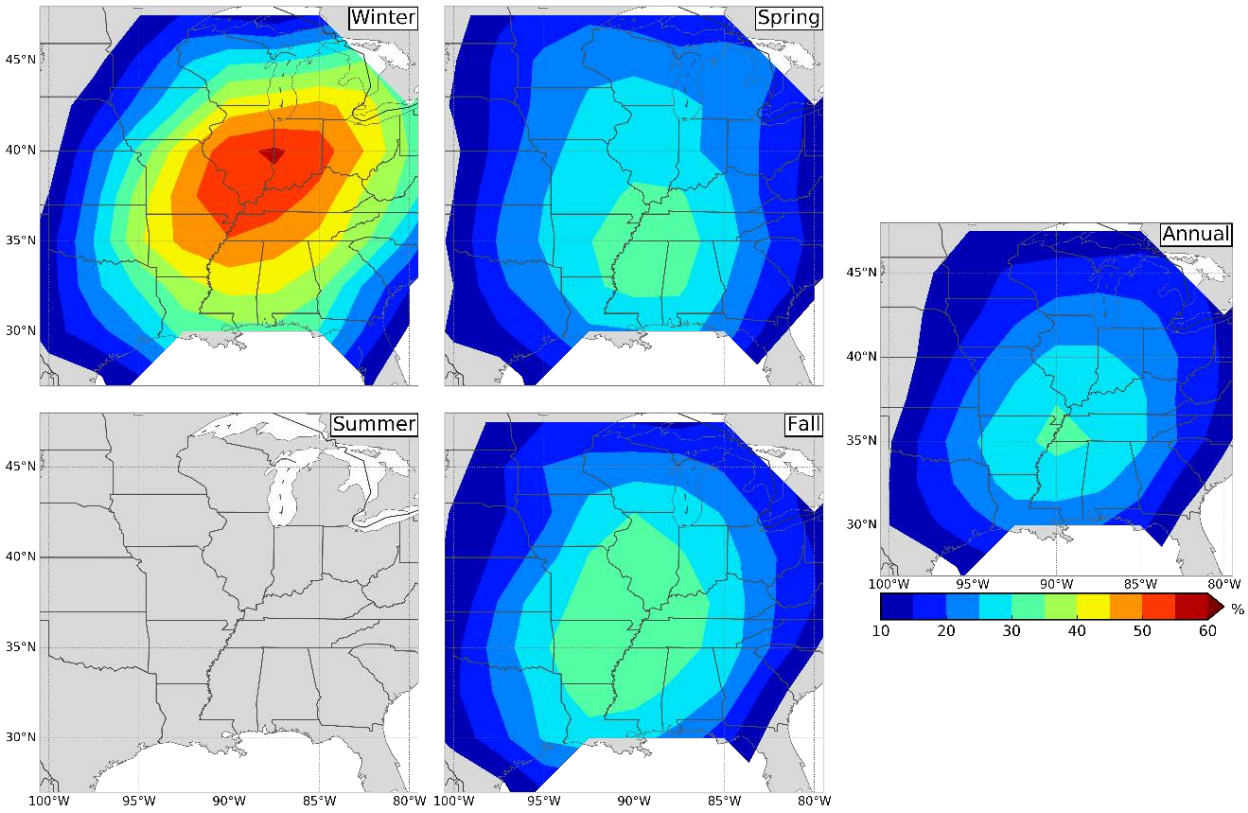

FIG. 4.10: Same as FIG. 4.7 but for NCEP-DOE.

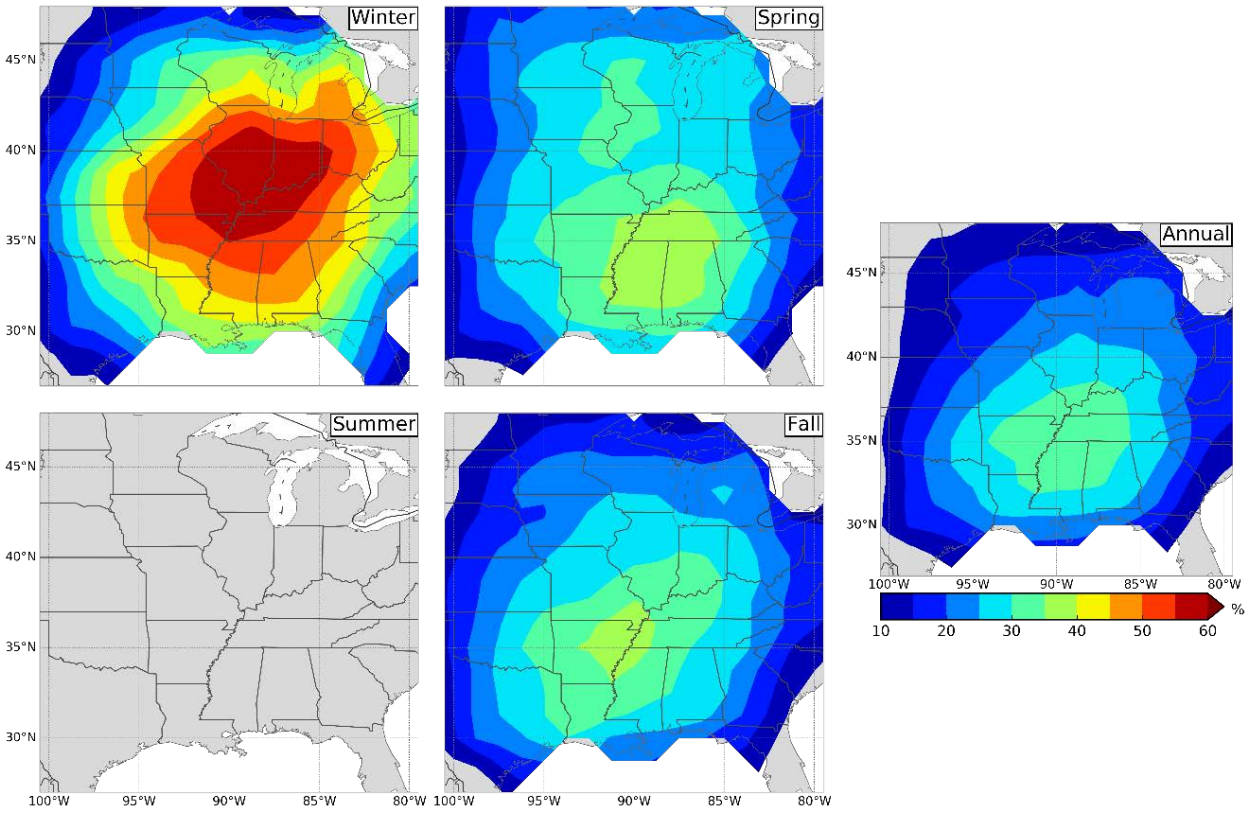

FIG. 4.11: Same as FIG. 4.7 but for JRA-55.

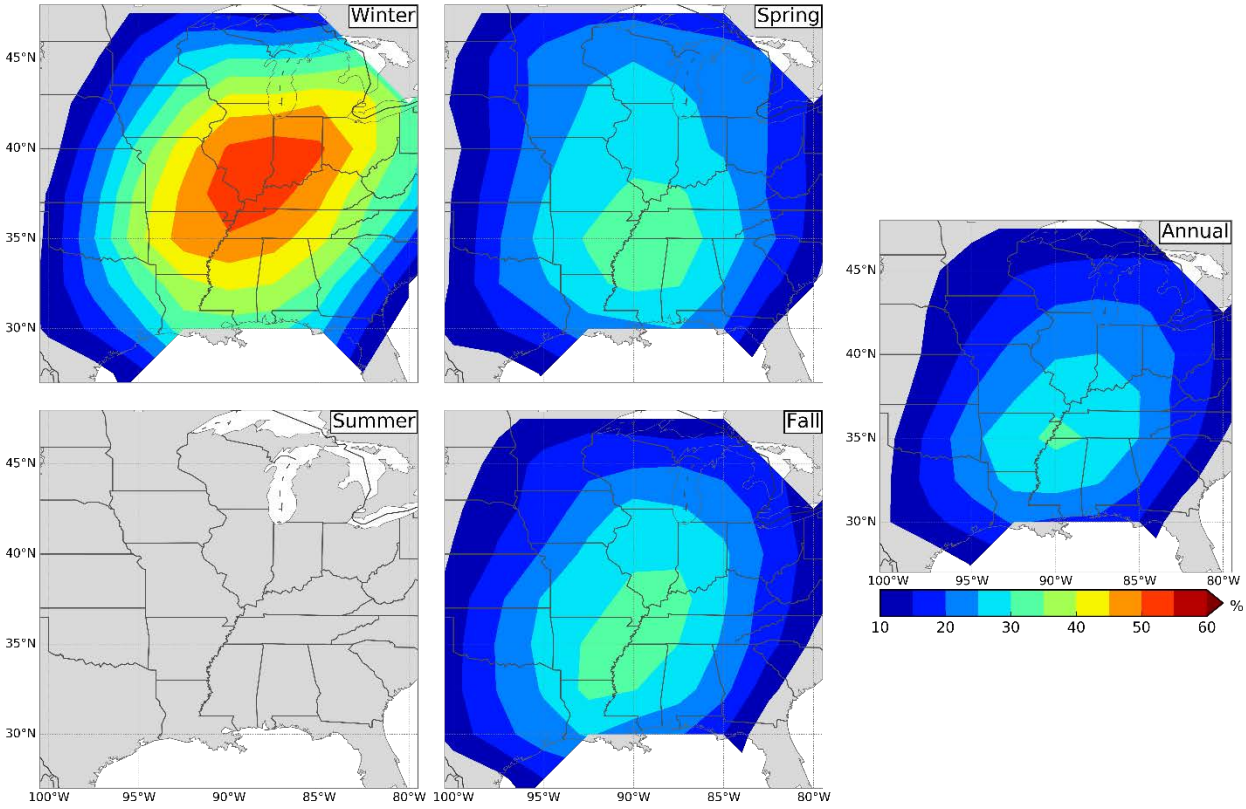

FIG. 4.12: Same as FIG. 4.7 but for NCEP-NCAR.

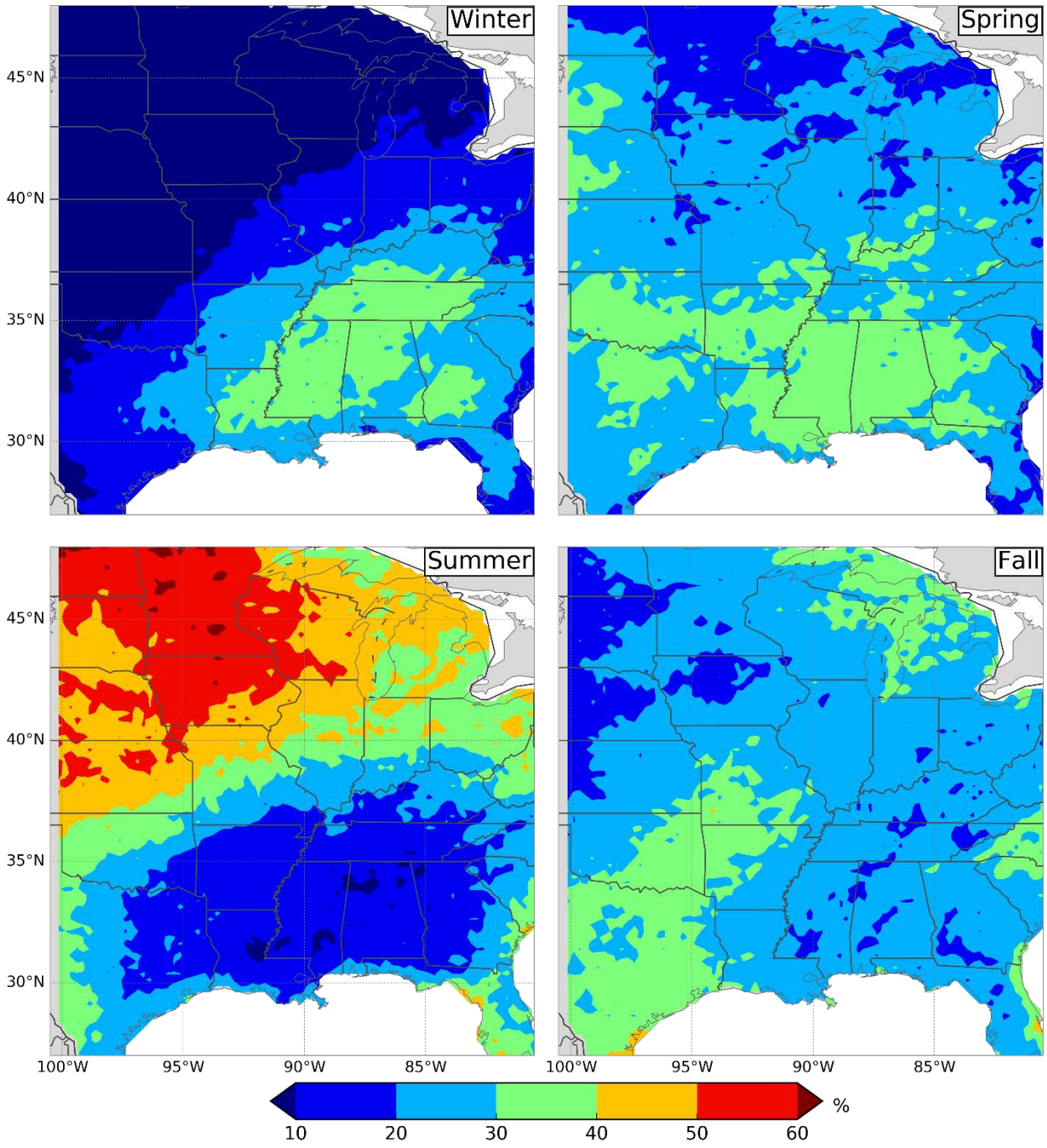

FIG. 4.13: Seasonality of top 1% daily precipitation events based on CPC data from 1948–2013.

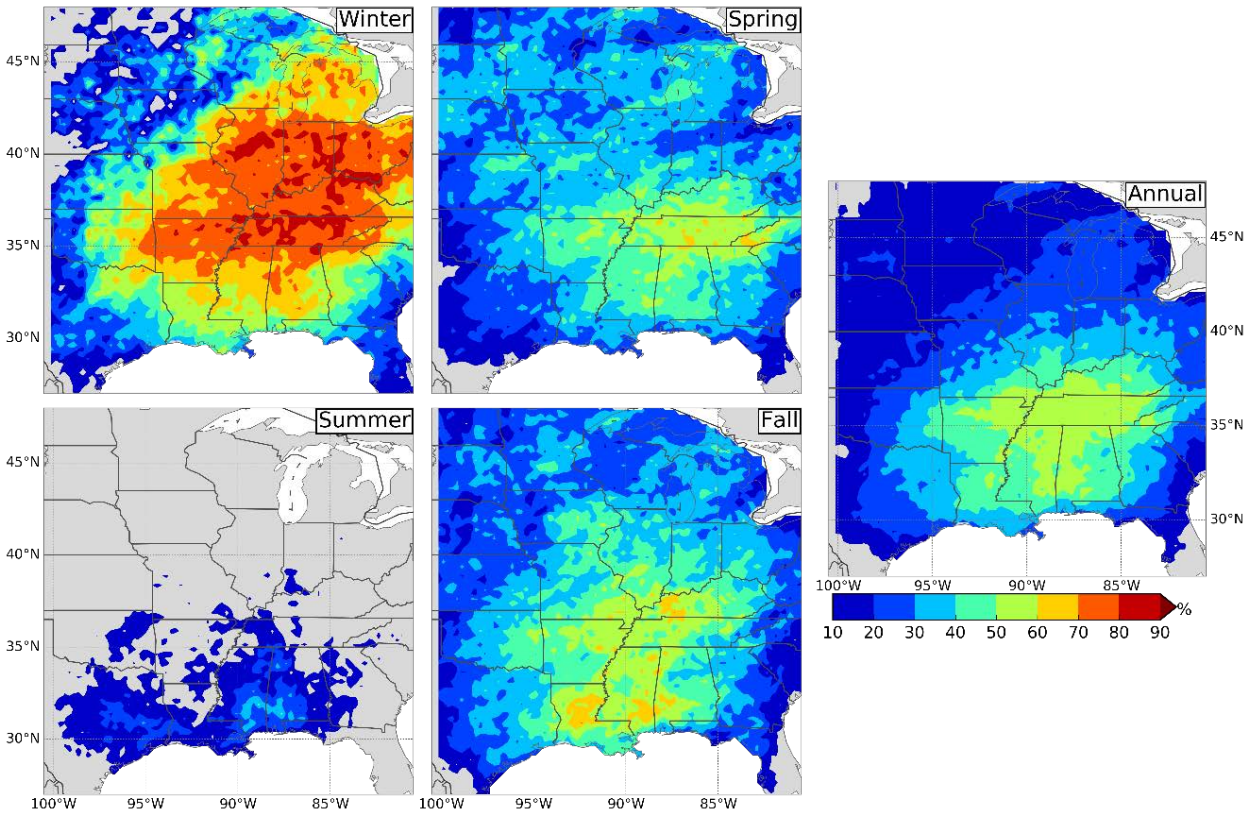

FIG. 4.14: Spatial distribution of the fraction of the top 1% daily extreme precipitation events associated with ARs. Results are based on 20CRV2 over the period 1948–2012.

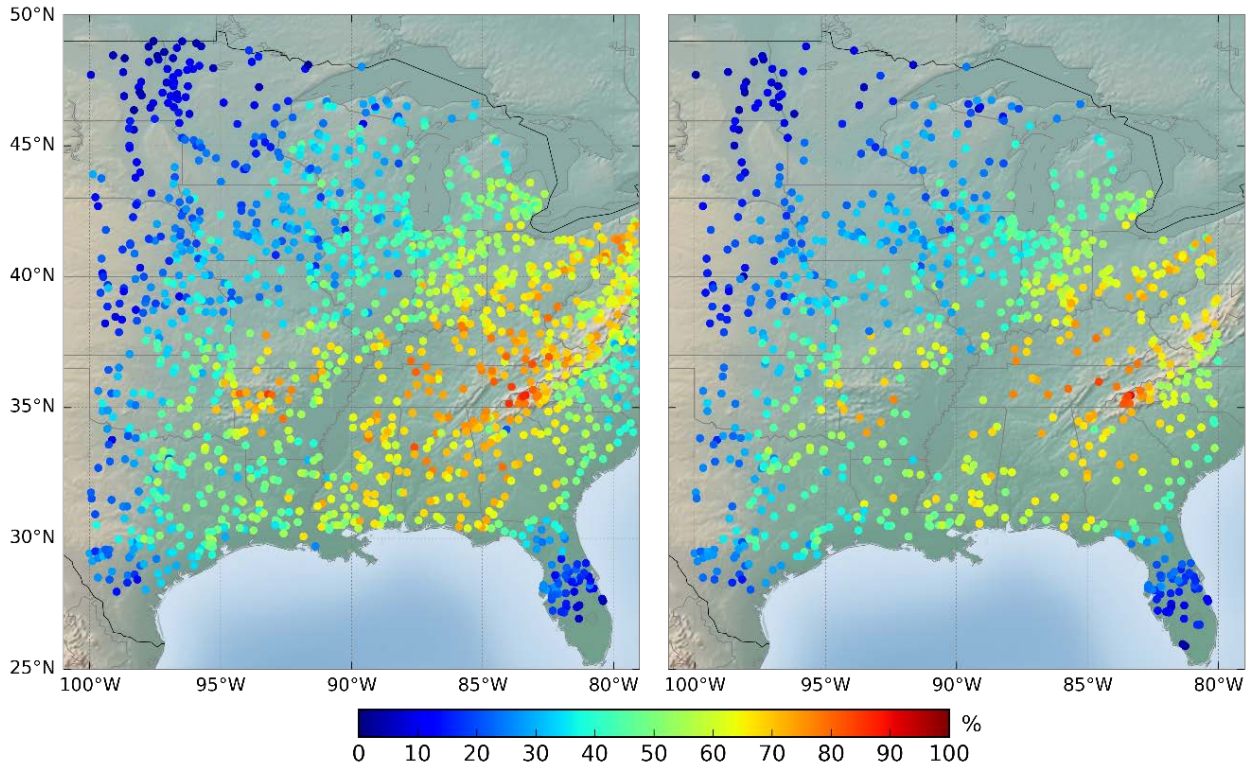

FIG. 4.15: Fraction of flood events related to ARs based on annual instantaneous peak data (left panel) and POT floods (right panel). Results are based on 20CRV2 over the period of record for each stream gage station.

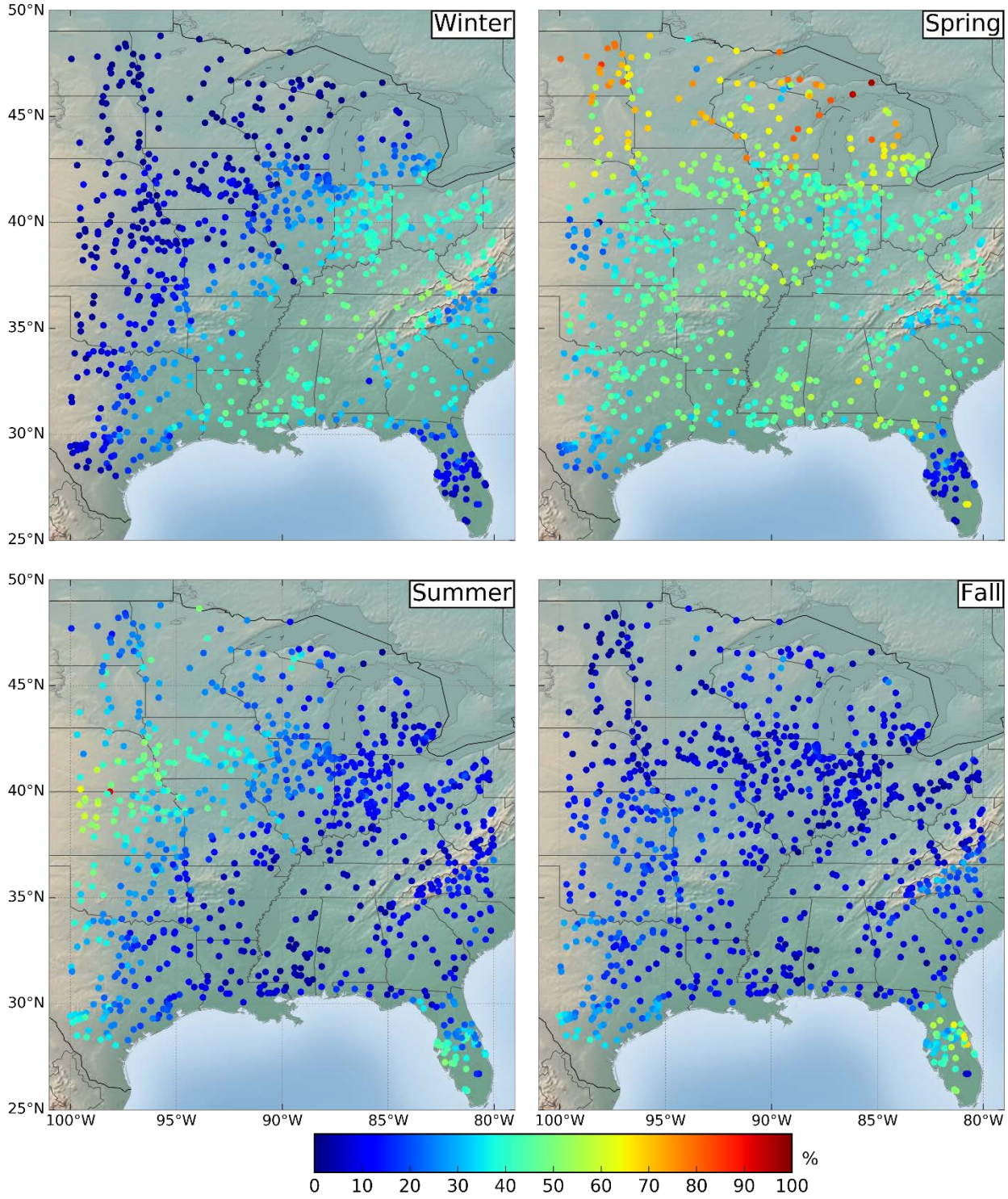

FIG. 4.16: Seasonality of POT floods based on average daily discharge data from long-term (more than 50 years of data) U.S. Geological Survey (USGS) gaging stations.

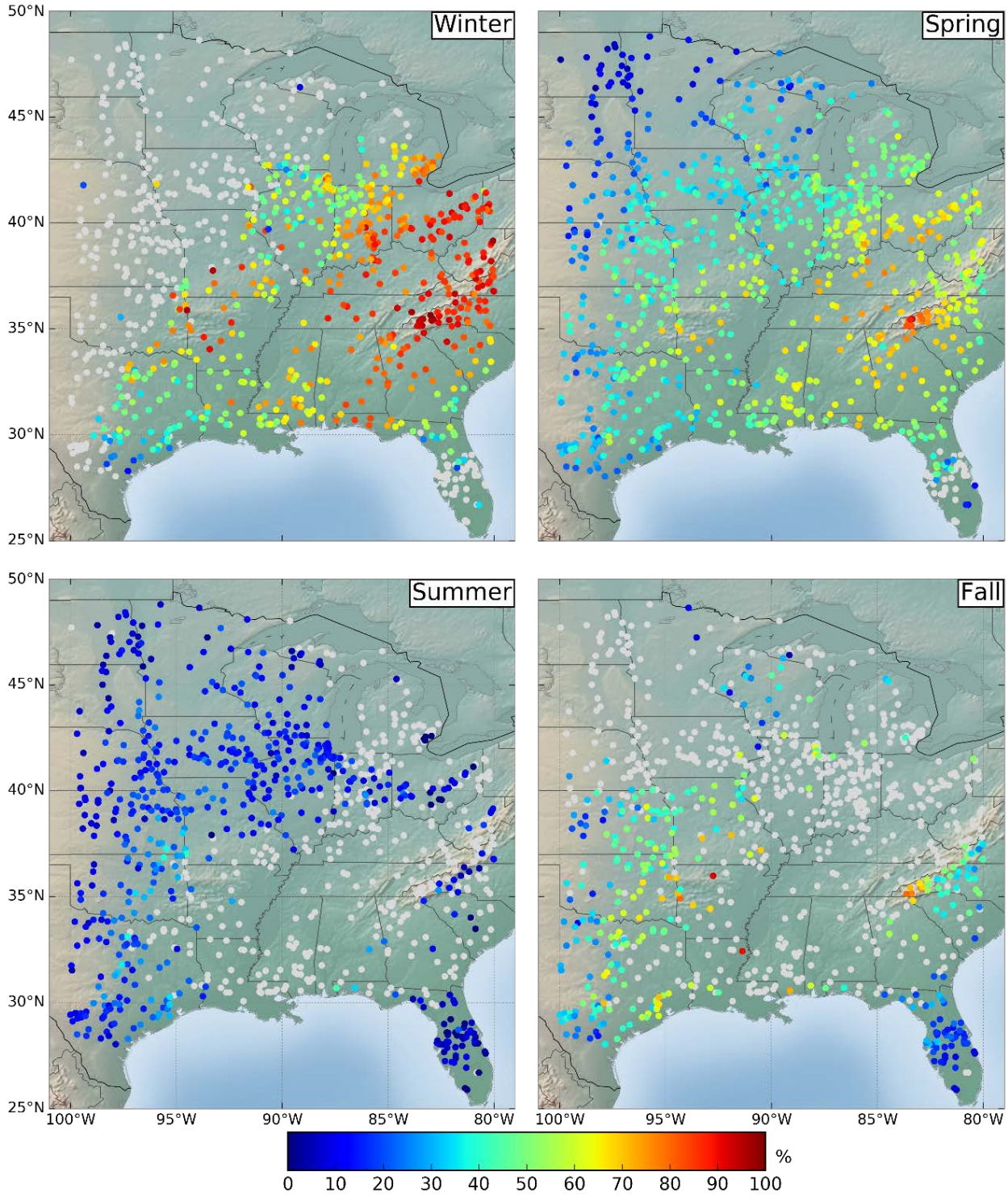

FIG. 4.17: Fraction of POT floods in different seasons associated with ARs. The grey dots are the stations that had less than 10 POT floods during the season.

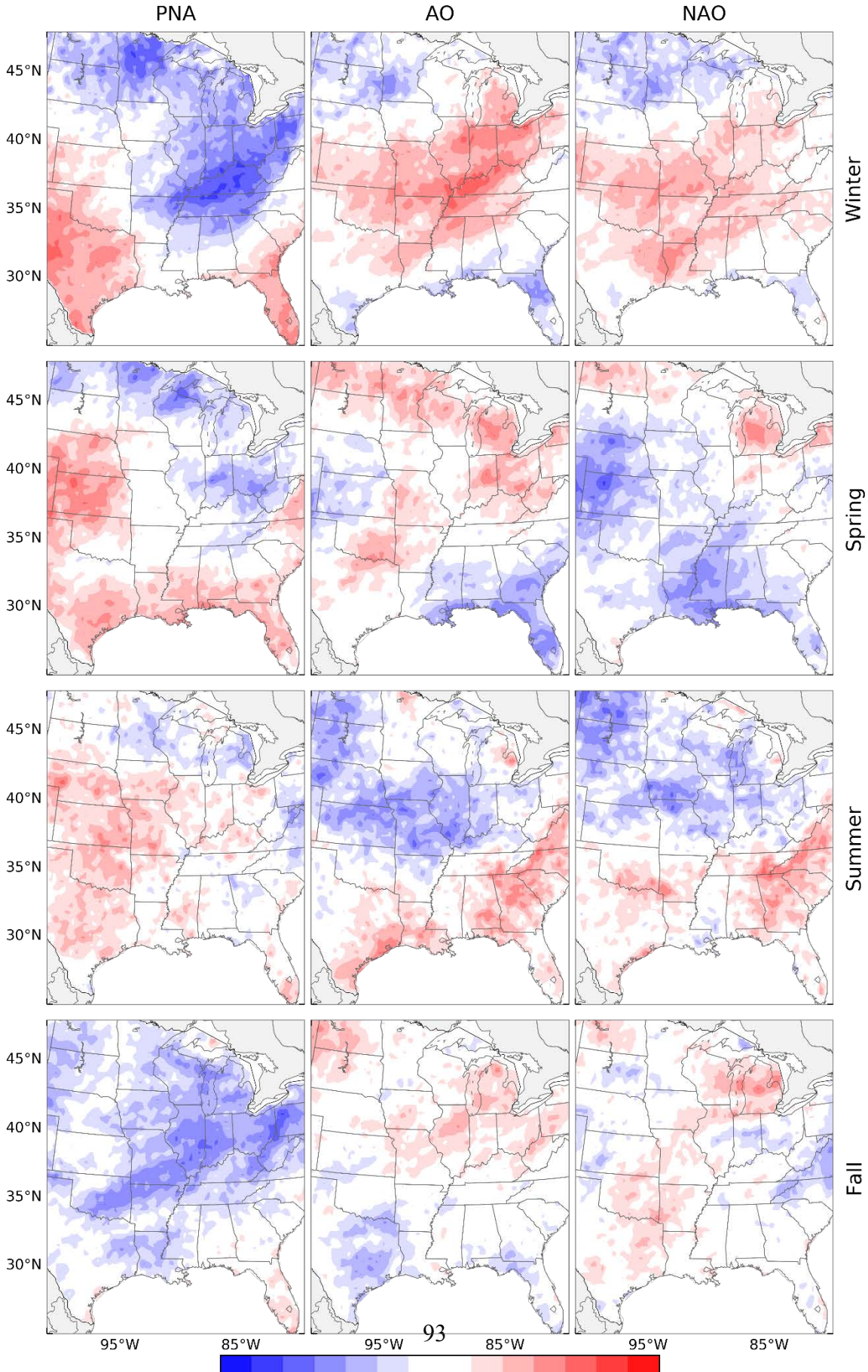
PNA
AO
NAO
Winter
Spring
Summer
Fall
45°N
40°N
35°N
30°N
95°W
85°W
-0.7
-0.5
-0.3
-0.1
0.1
0.3
0.5
0.7

FIG. 4.18: Relation between precipitation and large-scale atmospheric modes for different seasons. The figure shows Pearson's product-moment correlation coefficient of seasonal precipitation with PNA (left column), AO (middle column), and NAO (right column).

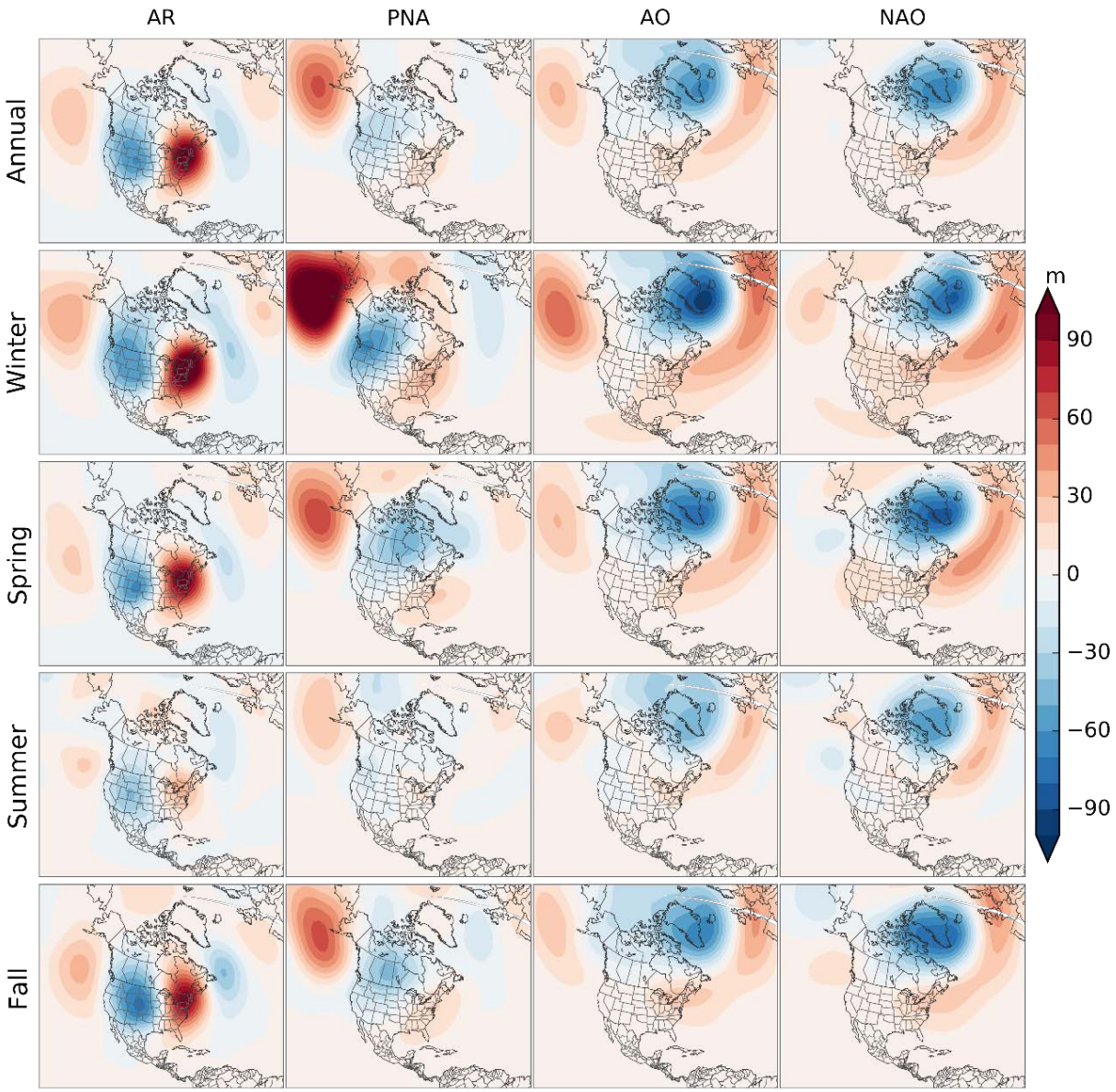

FIG 4.19: Relation between the frequency of ARs and large-scale atmospheric modes for different seasons based on 20CRV2 data from 1950–2012. The panels show the 500hPa geopotential height anomalies during ARs (left column), days with negative PNA (2nd column from the left), days with positive AO (3rd column from the left), and positive NAO (right column). Anomalies are computed from the baseline climatological mean of 1950-2012 data.

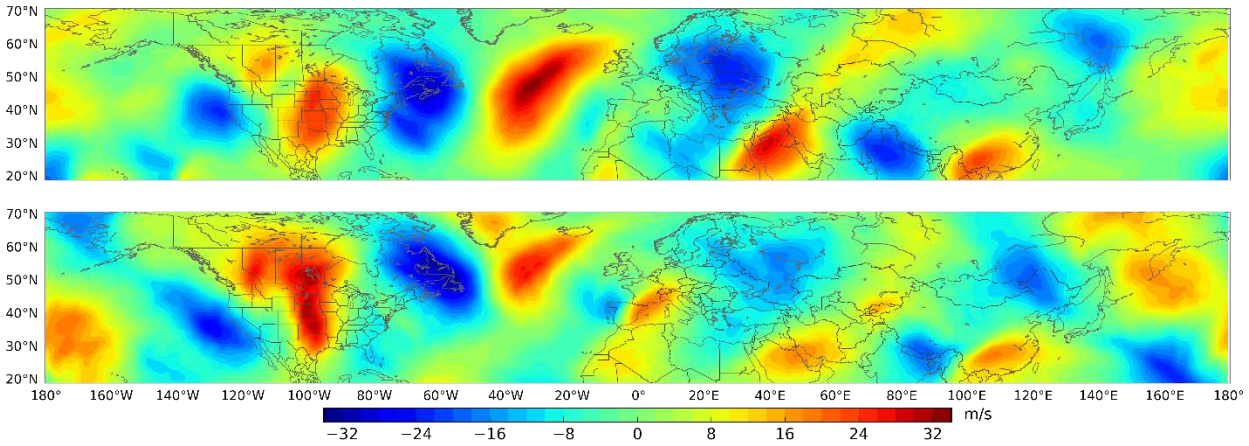

FIG. 4.20: Meridional (v-) wind velocity at 300hPa for the two longest ARs during 8–15 March 1990 AR (top panel), and 17-21 March 2012 AR (bottom panel).

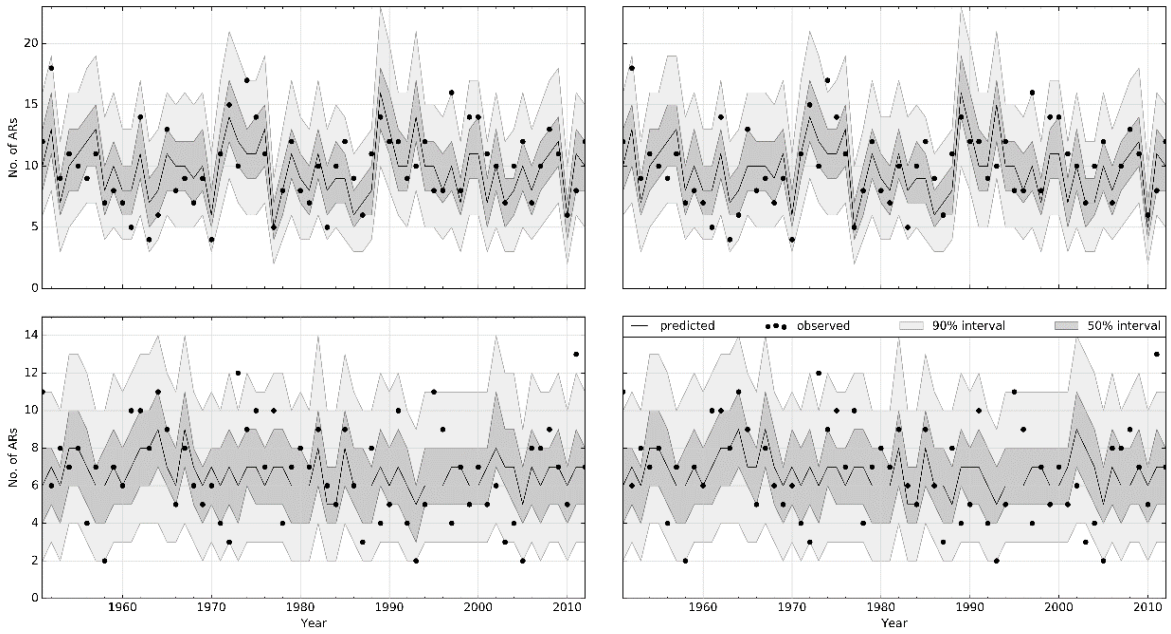

FIG. 4.21: Seasonal modeling of the frequency of ARs based on large-scale atmospheric modes using in-sample (left panels) and out-of-sample (right panels) estimates for different seasons. The top panels are for winter and the bottom panels are for spring. In each panel, the black dots are the observed number of ARs, the black line is the median from best Poisson model for the season (see Table 2), the dark-grey shaded region covers the 25th and 75th percentiles of the fitted Poisson distribution, and the light grey region covers the 5th and 95th percentiles. Monthly standardized PNA and AO indices from CPC are available from 1950 onwards, so the models are based on data from 1950 to 2012.

4.6 Tables Chapter 4

TABLE 4.1: Seasonality of ARs. Mean (Max) is the average (maximum) number of ARs per year (season).

MODEL	ANNUAL		WINTER		SPRING		SUMMER		FALL	
	Mean	*Max*	*Mean*	*Max*	*Mean*	*Max*	*Mean*	*Max*	*Mean*	*Max*
MERRA	26.8	37	11.1	16	7.9	15	1.5	4	6.2	11
ERA-INTERIM	26.6	35	10.7	15	8.3	14	1.4	3	6.1	11
JRA55	25.4	35	10.1	17	8.3	14	1.3	5	5.7	11
20CRV2	22.5	35	10.1	19	6.5	15	1.1	5	4.6	11
NCEP-NCAR	22	31	8.7	17	7.2	14	1.3	4	4.8	9
NCEP-DOE	22.9	31	8.7	12	7.1	13	1.5	5	5.5	8

TABLE 4.2: Poisson regression models relating the frequency of ARs to large-scale atmospheric modes ("α" is the intercept; the "β" values are the coefficients for each of the predictors; "AIC" is the value of the Akaike Information Criterion). Only covariates that are significant at the 0.01 significance level are used. None of the atmospheric indices are significant for the summer season. Note that p-values for PNA and NAO for fall are close to 0.10.

Season	Model	α	β_1	β_2	AIC
Winter	**Intercept Only**	2.29	---	---	317.3
	PNA+AO	2.33	-0.22 (PNA)	0.13 (AO)	287.2
Spring	**Intercept Only**	1.91	---	---	294.2
	PNA	1.90	-0.18	---	289.2

CHAPTER 5

MODELLING THE FREQUENCY OF WINTER HEAVY PRECIPITATION EVENTS OVER THE CENTRAL UNITED STATES USING BAYESIAN HIERARCHICAL MODELS

Precipitation extremes represent a major natural hazard with a high toll in terms of fatalities and economic impacts. This is particularly true for the central United States, which is a region that experiences these events on a yearly basis. Improved understanding and modeling of the drivers responsible for the occurrence of extreme precipitation over this area would provide the basic information to improve preparation and mitigation efforts. Recent studies suggest that specific climatic features can be useful to describe the frequency of heavy precipitation events over the central United States, potentially increasing our skill to forecast such events. For example, Harding and Snyder (2015) showed that a negative PNA pattern can result in persistent and long-wavelength planetary waves (see Figure 4.20) that can prolong the duration of GPLLJ. The increased duration of GPLLJ can be expected to increase the rainfall over the central United States. Mallakpour and Villarini (2016a) evaluated five climate indices to learn their effects on the frequency of extreme events using at-site Poisson regressions with 65 years of data over the contiguous United States. The results revealed that the climate indices can have contrasting effects at different locations within the same season; over much of the central United States, PNA showed a significant negative effect on heavy precipitation frequency (i.e., the more positive the value of the PNA index, the lower the number of heavy precipitation events, on average), particularly during winter. These results are in agreement with Mallakpour and Villarini (2016b) who analyzed the frequency of floods at 774 long-term USGS stream gages across the central United States.

Over the past few years, we have seen several studies employing climate information for nonstationary extreme precipitation and flood frequency analyses, and below I highlight a few of these works to introduce the goals of this chapter. Three climate indices were used by Gregersen et al. (2013) to model the annual frequency of daily and 10-min extreme rainfall events at 70 stations in a Danish rain gage network with record lengths ranging from 10 to 30 years. The results showed that the East Atlantic (EA) climate pattern is able

to explain a significant portion of the variability in the annual frequency of extreme rainfall over the region. Sun et al. (2014) used a measure of El Niño-Southern Oscillation (ENSO) called the Southern Oscillation Index (SOI; it is measured as the mean sea level pressure difference between Tahiti and Darwin) to model the total precipitation and extreme precipitation in summer (December-January-February) at 16 stations in southeast Queensland, Australia, using the lognormal and Generalized Extreme Value (GEV) distributions, respectively. The parameters of the two distributions were treated as a function of the time-varying magnitude of the SOI index averaged during the austral summer. The results showed that a negative value of the SOI index (i.e., El Niño phase) has a significant effect on precipitation over the region; more specifically, the 100-year precipitation event is about 25–50% higher in magnitude than what is expected using a stationary model, which does not condition the parameters of the GEV distribution on the climate index. Renard and Lall (2014) modelled POT-based frequency of autumn (October-November-December) heavy precipitation events at 16 stations in the Mediterranean France using the Poisson distribution whose parameter was conditioned on autumn-averaged 500hPa geopotential height in a region in the North Atlantic. The authors used a spatial Bayesian hierarchical framework for the modeling, and assumed a climate effect that varied with time but remained similar among the stations with the goal of introducing spatial consistency among the different stations. The authors showed that the model with the higher prediction skill was the one in which the climate field was incorporated rather than the baseline model that did not include any climate covariate. The authors further noted that, at many stations, this model performed better than the model that included just the climate indices (e.g., NAO) as opposed to entire climate field. Some other useful references on climate-informed frequency analysis of heavy precipitation events include the works by Cooley et al. (2007), Aryal et al. (2009), Lima et al. (2015), and Sun et al. (2015).

Chapter 4 helped us understand that heavy precipitation events over the central United States are in most cases directly linked to ARs (especially in winter season), and provided a better insight into the associated climate controls. This physical understanding can be further expanded to develop statistical models for the analysis of the frequency of heavy precipitation events, where the seasonal frequency is conditioned on ARs. Previously,

Steinschneider and Lall (2015a) used a similar idea to develop a Bayesian hierarchical model for the frequency and magnitude of winter extreme rainfall over Northern California. In their Bayesian framework, a Poisson distribution was fitted to the frequency of extreme events, with its only parameter conditioned on the average quantity of moisture delivered to the region by TMEs during winter. As in Renard and Lall (2014), the covariate (i.e., quantity of moisture delivered to the region) used by Steinschneider and Lall (2015a) varied only in time and was same for all the stations for a particular year. At all the 39 stations considered in their work, the inclusion of TME-driven moisture considerably improved the predictions of extreme precipitation events compared to the other models that did not include this moisture quantity as a covariate.

With the understanding of the relationship between climate modes, ARs, and extreme precipitation events obtained from the previous chapters, in this chapter I intend to develop different spatio-temporal statistical models for the frequency of heavy precipitation events during the winter season (December-January-February) over the central United States. Here, I focus on the frequency rather than the magnitude of these events because recent studies have shown an increasing trend in the frequency of floods and extreme precipitation events over much of the central United States (Mallakpour and Villarini 2015). In this context, it would be helpful to quantify the effect of prominent climate modes and ARs on the frequency of heavy precipitation events.

Therefore, the specific objectives of this chapter are listed below:

1. to statistically model the frequency of heavy precipitation events conditional on the frequency of ARs, with the aim of quantifying the effect of ARs on heavy precipitation and how this effect varies spatially over the study region.
2. to statistically quantify the spatial effect of PNA and AO on the frequency of heavy precipitation.
3. to develop a hierarchical model in which the frequency of heavy rainfall events is conditional on the frequency of ARs which, in turn, is conditional on magnitudes of PNA and AO. As we have seen in Chapter 4, heavy precipitation is directly linked to ARs, and ARs, in turn, are linked to PNA and AO, especially during winter.

4. to compare and contrast all these different models in terms of model fit and predictive skill.

5.1 Data and Methods

5.1.1 Data

To obtain the frequency of heavy precipitation events, I retrieved daily precipitation data from the Global Historical Climatology Network (GHCN)-Daily dataset (Menne et al. 2012). The GHCN-Daily dataset contains observational weather data at more than 80,000 weather stations worldwide. All the data, regardless of their origin, are subject to the same quality control procedure, which includes checking for data duplication, values beyond limits (i.e., outliers), large differences between adjacent values in the data distribution, and other inconsistencies. For this chapter, I extracted precipitation stations for the central United States covering the region 30°N–45°N and 100°W–80°W and having data available from 1950 through 2014. For meaningful and robust analyses, only those stations that have at least 60 complete years during the period 1950–2014 are selected (I define a "complete year" as a year that has no more than 5 missing daily observations). Based on these criteria, I selected a total of 426 stations.

The frequency of heavy precipitation events at each station is obtained using the POT method, where I used the 90th percentile of the precipitation distribution as the threshold. I then count the number of days exceeding this threshold every winter as my response variable.

A potential issue with this definition of frequency is the temporal dependence in the heavy precipitation days that occur close to each other. This issue is investigated by Cooley et al. (2007) for the daily extremes over the Front Range of Colorado, where they compare the modelling results based on the frequency obtained from de-clustering POTs against the results without de-clustering; the authors reported essentially the same results from both methods. Temporal autocorrelation is expected to be more significant for short-duration events (i.e., sub-daily time scales). A more thorough examination of the potential impact of autocorrelation on my results could be examined in future work.

The variables used to identify ARs, 6-hourly q, u-wind and v-wind are obtained from the most recent version of the 20th century reanalysis dataset 20CRV2C available from

1851 to 2014. This reanalysis product has the same horizontal and vertical resolutions as 20CRV2. The same algorithm used in Chapter 4 is applied to 20CRV2C to identify ARs. I refer to AR-related rainfall as the daily precipitation for a rain gage that is located within 250km of the AR major axis during at least one AR-time step. Based on these criteria, the frequency of winter ARs at a given station is the number of days ARs affected that station during winter.

The two climate indices that I consider are PNA and AO. Even though these indices are available online from CPC (http://www.cpc.ncep.noaa.gov/products/precip/CWlink/daily_ao_index/teleconnections.shtml), I decided to calculate them directly from 20CRV2C so that all the results are consistent with a given reanalysis product. Therefore, I used monthly MSLP and 500hPa geopotential height fields over the Northern Hemisphere from 20ºN to the North Pole from 1950 to 2014 from 20CRV2C.

To calculate the AO index, I adopted the method developed by Thompson and Wallace (1998, 2000), also followed by CPC for operational purposes. In this method, monthly MSLP gridded fields are multiplied by $\sqrt{\cos(lat)}$ to ensure equal weights for equal-area grid cells. At all the grid cells in the dataset, MSLP anomalies are calculated with respect to the period 1976–2005, resulting in a matrix of anomalies (a two dimensional matrix with the first dimension corresponding to the months and the second dimension corresponds to the grid points). From this matrix, I obtain a variance-covariance matrix, giving the covariance of MSLP among the grid cells. I performed EOF analysis on the variance-covariance matrix, and the resulting leading eigenvector (also called the first loading pattern when the eigenvector is multiplied by the square root of the eigenvalue) that corresponds to the highest eigenvalue is taken as the leading EOF of the Northern Hemisphere MSLP. The leading EOF when multiplied by the MSLP anomaly matrix produces the AO index for all the months from 1950–2014.

The PNA index is obtained in a similar way but from rotated-EOF (REOF) analysis using the method by Barnston and Livezey (1987). First I performed the varimax rotation (Kaiser 1958, 1959) on the first 15 un-rotated loading patterns of the EOF analysis that explained more than 87% of the variance in the 500hPa geopotential height data. As shown by Barnston and Livezey (1987), REOF analysis helps to visualize the atmospheric patterns

present in the data better than the (un-rotated) EOF analysis. After the rotation, the resulting rotated loading patterns for December, January and February that resembled (upon visual examination) the PNA pattern for winter by CPC and Barnston and Livezey (1987) were taken as the PNA loadings; then the PNA index was calculated similar to the AO index.

The AO and PNA indices obtained using this methodology matched well the CPC indices; during the period 1950–2014, the correlation coefficients between the indices provided by CPC and the ones I calculated were more than 0.90 for all the three winter months.

5.1.2 Models

Bayesian hierarchical models are becoming a popular approach for frequency analysis in hydrology. The reasons for such popularity lies in their ease of implementation for large and complex models, simple and natural ways of quantifying uncertainties, and simple ways of incorporating any prior knowledge about the parameters into the model. Because my precipitation and AR datasets are relatively large, a Bayesian hierarchical framework appears a perfect candidate for modelling purposes. The models that I develop and evaluate are detailed below.

A Bayesian hierarchical model is generally described in three layers: 1) a data layer which provides the likelihood of the data; 2) a latent process layer, which models the underlying latent (physical) process that drives the model in the data layer; and 3) the prior layer, in which priors are specified for all the unknown parameters.

Data Layer

In the data layer, I assume the response variable *Y* follows a Poisson distribution with its mean parameter varying with location (station) and time (year).

$$Y_{s,t} \sim Pois\left(\mu_{s,t}\right) \qquad 5.1$$

where $Y_{s,t}$ is the number of heavy precipitation days at station *s* (*s* = 1, 2… *S*) and year *t* (*t* = 1, 2, …, *T*); $\mu_{s,t}$ is the mean of the Poisson process at station *s* and at time *t*. Both *Y* and μ are of *S*×*T* dimension.

Latent process layer

I consider different models to represent different underlying physical processes that drive the frequency of heavy precipitation events in the *data layer*.

The simplest model is the base model (M1), which has fixed independent intercept terms for all the stations:

M1: $\log\left(\mu_{s,t}\right) = \beta_s$

Here β_s is the intercept for station *s*. With this model, the occurrences of heavy events at each station are assumed to be independent and identically distributed (iid) Poisson random variates with a mean parameter that is most likely concentrated near the climatological mean frequency of the station.

In the second model (M2), the number of winter ARs is added as a covariate to describe the mean of the Poisson process in the *data layer*, and as such assumes that the frequency of heavy precipitation is directly related to the frequency of ARs at each station:

M2: $\log\left(\mu_{s,t}\right) = \beta_0^{ar} + \beta_1^{ar} * AR_{s,t} + \beta_{s,0}^{ar} + \beta_{s,1}^{ar} * AR_{s,t}$

Here, β_0^{ar} is the fixed overall intercept (i.e., over the entire region), β_1^{ar} is the fixed overall slope coefficient related to the covariate AR, vector $\beta_{-,0}^{ar}$ ($S \times 1$) is the station-wise offset to the intercept, with $\beta_0^{ar} + \beta_{s,0}^{ar}$ as the intercept for station *s*; similarly $\beta_{-,1}^{ar}$ is the station-wise offset to the slope coefficient corresponding to ARs, with $\beta_1^{ar} + \beta_{s,1}^{ar}$ as the slope for station *s*. In this model, the spatial similarity in the frequency of extremes in assumed to be related to the spatial similarity in ARs, and this is introduced by providing random spatial structures on the intercept and slope coefficients: the parameter set $\boldsymbol{\beta}_s^{ar} = [\beta_{s,0}^{ar}, \beta_{s,1}^{ar}]$ is treated as random spatial effects on site *s*. This is discussed in more detail in the *prior layer* later in this section.

The third model (M3) takes PNA and AO indices as covariates, and hence assumes that the frequency of heavy precipitation events are directly related to the two indices:

M3: $\log\left(\mu_{s,t}\right) = \beta_0 + \beta_1 * PNA_t + \beta_2 * AO_t + \beta_{s,0} + \beta_{s,1} * PNA_t + \beta_{s,2} * AO_t$

Similar to M2, β_0 is the overall intercept, β_1 is the overall slope coefficient related to the covariate PNA, and β_2 is the overall slope coefficient related to AO. Vector $\beta_{-,0}$ ($S \times 1$) is the station-wise offset to the intercept, with $\beta_0 + \beta_{s,0}$ being the intercept for station s; $\beta_{-,1}$ is the station-wise offset to the slope coefficient corresponding to PNA, with $\beta_1 + \beta_{s,1}$ being the slope for station s; similarly, $\beta_{-,2}$ is the station-wise slope offset to the coefficient corresponding to AO, with $\beta_2 + \beta_{s,2}$ being the slope for station s. As in M2, the coefficients. $\boldsymbol{\beta}_s = [\beta_{s,0}, \beta_{s,1}, \beta_{s,2}]$ are treated as random effects on site s. As will be shown in the *prior layer* later, a spatial structure is assumed on the parameter set $\boldsymbol{\beta}_- = [\beta_{-,0}, \beta_{-,1}, \beta_{-,2}]$.

The most complex model (M4) that I evaluate is the one where the frequency of heavy precipitation events is directly related to the frequency of ARs, which in turn is directly related to the PNA and AO indices. Hence, an additional level is introduced to describe the frequency of ARs as shown below. As such, the relationship between the frequency of heavy precipitation and the two climate indices is thought to be indirect, with ARs acting as a bridge between the two layers:

$$\log\left(\mu_{s,t}\right) = \beta_0^{ar} + \beta_0^{ar} * LAR_{s,t} + \beta_{s,0}^{ar} + \beta_{s,1}^{ar} * LAR_{s,t}$$

M4: $$AR_{s,t} \sim Pois\left(\log\left(LAR_{s,t}\right)\right)$$

$$\log\left(LAR_{s,t}\right) = \beta_0 + \beta_1 * PNA_t + \beta_2 * AO_t + \beta_{s,0} + \beta_{s,1} * PNA_t + \beta_{s,2} * AO_t$$

In this model, $AR_{s,t}$ is the observed frequency of ARs at station s and at time t; $AR_{s,t}$ is assumed to follow a Poisson distribution with mean $LAR_{s,t}$ at station s and time t. LAR is estimated based on the covariates PNA and AO; β_0 is the overall intercept for the observed AR frequency, β_1 and β_2 are the overall slope coefficients related to the covariates PNA and AO. As earlier, the vectors $\beta_{-,0}$, $\beta_{-,1}$ and $\beta_{-,2}$ are the station-wise offsets to the intercepts, and the two slope coefficients for AR frequency; β_0^{ar} is the overall

intercept for the frequency of heavy precipitation, β_1^{ar} is the overall slope parameter related to the covariate AR, and $\beta_0^{ar} + \beta_{s,0}^{ar}$ and $\beta_1^{ar} + \beta_{s,1}^{ar}$ provide the spatial effects to the intercept and the slope parameters. The spatial structure on the parameter matrices $\boldsymbol{\beta}_{-}^{ar} = [\beta_{-,0}^{ar}, \beta_{-,1}^{ar}, \beta_{-,2}^{ar}]$ and $\boldsymbol{\beta}_{-} = [\beta_{-,0}, \beta_{-,1}]$ is provided in the *prior layer* below.

Prior layer

To complete the hierarchical formulation, for all the unknown parameters in the models I need to assume prior distributions, which may include any prior experience one has about the parameters. For most of the parameters in these models, I will use non-informative and weakly-informative priors, which means that all the information for the posterior distributions of the parameters are provided only by the data. For M1, the intercept parameters β_s are provided with independent weakly-informative Gaussian priors with 0 mean and a large variance (0.001^{-1}); here, independence in the priors that no information is shared among the stations to estimate the parameters. Independent flat priors are adopted for all the fixed parameters that define the overall intercept and slope terms (β_0, β_1, β_2, β_0^{ar} and β_1^{ar}) for the other three models.

For the other parameters of M2, M3 and M4 (i.e., $\boldsymbol{\beta}_{-}^{ar}$ $\boldsymbol{\beta}_{-}$), joint models called multivariate conditionally autoregressive models (MCAR) are assumed as priors. These models provide ways to share information across the neighboring stations, and hence provide spatial structure to the parameter sets. In addition, MCAR is also useful in estimating correlations between different parameters, such as the correlation between β_0 and β_1. MCAR is a multivariate version of the CAR model (Besag 1974; Mardia 1988), and assumes a zero-mean multivariate normal distribution for the parameter sets; specifically:

$$\boldsymbol{\beta}_{-} \sim MCAR\left(\mathbf{0}, \Sigma = \boldsymbol{\tau}^{-1}\right) \qquad 5.2$$

Where, $\boldsymbol{\beta}_{-}$ is an $S \times p$ matrix, with p being the number of parameters (for M2 is 2, intercept and slope), Σ is the variance-covariance matrix and $\boldsymbol{\tau}$ is the precision matrix with size $S*p$

× *S*p*. This results in a conditional multivariate normal distribution for the parameter set for station *s* as:

$$\boldsymbol{\beta}_s \mid \boldsymbol{\beta}_{j:j\in NB(s)} \sim MVN\left(\sum_{j:j\in NB(s)} W_{s,j}\boldsymbol{\beta}_j, \Sigma_s = \tau_s^{-1}\right) \qquad 5.3$$

$$W_{s,j} = \frac{w_{s,j}}{w_s +} I_{p\times p}$$

where $NB(s)$ is a set of neighbors of station s, $w_{s,j}$ is the weight expressing the spatial dependence between stations s and j, and $I_{p\times p}$ is an identity matrix. Here, without any prior knowledge, I set unit weight for each neighboring station and zero weight for the rest:

$$w_{s,j} = 1 \qquad \forall j \in NB(s)$$
$$w_{s,j} = 0 \qquad \forall j \notin NB(s)$$
$$w_{s,s} = 0$$
$$w_s + = \sum_{j:j\in NB(s)} w_{s,j}$$

For the MCAR prior, stations within a distance of 150km were considered as neighbors of each other; based on this spatial criterion, only one station ended up with a lone neighbor, while there are 12 neighbors for each station on average.

The precision matrix is denoted with τ_s, and its inverse (Σ_s) gives the variance-covariance matrix of the site-specific intercept and slope parameters, assumed to be the same for all the stations. The diagonal entries of Σ_s are σ_0^2, σ_1^2, and σ_p^2, where σ_0^2 gives the variance of the intercept parameter, while σ_1^2, σ_p^2 are the variances corresponding to first and pth slope parameters. With this formulation, the correlation between different parameters can be obtained from the off diagonal elements of Σ_s: for example, $\rho_{0,1} = \frac{\Sigma_s[1,1]}{\sqrt{\sigma_0^2\sigma_1^2}}$ is the correlation between the intercept parameter and the first slope parameter, while $\rho_{1,2}$ is the correlation between first and the second slope parameters. The hyperparameter matrix τ_s is the only term without a prior distribution, and its specification needs extra care; this is because we need to ensure that τ_s is positive definite, so that the

precision parameters σ_0^2 and σ_1^2 are non-negative, and the correlation between the parameters is strictly between -1 and 1. A convenient prior in such cases is a multivariate analog of the gamma distribution called the Wishart distribution $Wish(\Omega, \nu)$, where Ω is the scale matrix and ν is the number of degrees of freedom. With this, the prior mean of τ_s is the matrix $\Omega * \nu^{-1}$; when we set ν equal to the number of parameters *p*, the result is the least informative prior from the Wishart family on τ_s. The prior distribution, $Wish(\Omega, \nu = p+1)$, while ensuring positive semidefinitiveness of τ_s has an added advantage that it produces a non-informative uniform prior ranging from -1 to 1 on the correlation parameters. The only drawback with the Wishart prior is that it constrains the variance parameters σ_0^2 and σ_1^2. A tricky solution is the use of the scaled-Wishart distribution as shown in Gelman and Hill (2007); however, I experienced difficulties in achieving the convergence of the scaling parameters of this distribution with these datasets. For this reason, I use $Wish(I_{p\times p}, \nu = p+1)$ as the prior for τ_s.

A few points one may note from the above models and the MCAR prior formulation:

1. The prior mean of the parameters at a station is taken as the weighted average of the neighboring stations.
2. The MCAR model assumes the same correlations among parameters, and the same variances of intercept and slope parameters for all sites. These assumption can be relaxed, albeit at a higher computational cost.
3. Constraints, such as $\sum_{s=1}^{S} \beta_{s,0} = 0$ for the intercept parameters, are necessary on the random spatial effects for their identification along with the respective fixed parameters.

Here, we have used MCAR model instead of geostatistical models, such as the ones where the covariance matrix for stations is powered exponential, because it involves taking the inverse of a large matrix at each iteration in Gibbs sampling, which makes the convergence very slow.

Note that in the above models, I have denoted all the parameters that include ARs as covariate with a superscript (e.g., β_0^{ar} in M2 and M4). Similarly, the correlation terms related to the AR covariate are written as $\rho_{0,1}^{ar}$ for these models.

To obtain the posterior simulations from these models, I used an open source and widely used program OpenBUGS (Bayesian inference using Gibbs sampling; Spiegelhalter et al. 2007) along with the R (Team 2013) package R2OpenBUGS (Sturtz et al. 2005). The programs are run on a 64-bit windows machine with 3.4GHz CPU speed and 16GB RAM.

5.1.3 Convergence

The accuracy of Markov Chains Monte Carlo (MCMC) simulations critically depends on their convergence to a stationary distribution; for this reason, a lot of research has been devoted to this topic in the last few decades, leading to many convergence diagnostics. Each of the diagnostics seems to have some advantages and some disadvantages, and the use of multiple diagnostics for checking the convergence of the MCMC simulations has been recommended (Cowles and Carlin 1996; Brooks and Gelman 1998). A review of some of the most common diagnostics can be found in Cowles and Carlin (1996) and Brooks and Roberts (1998). In addition to the visual examination of trace plots, I use multiple diagnostic methods in this chapter, and all the diagnostics can be readily obtained using the R package CODA (Plummer et al. 2006). The diagnostics that I use in this chapter are briefly described here.

Potential scale reduction factor: Gelman and Rubin (1992) pointed out that diagnostics obtained by running a single MCMC chain are not good enough to claim convergence, and more than one chain with different/overdispersed initial values should be evaluated. On this ground, the authors propose the multi-chain based potential scale reduction factor ($\hat{R}$) to diagnose convergence. This diagnostic was later modified by Brooks and Gelman (1998) and is now perhaps the most commonly used convergence diagnostic in the Bayesian literature. The value of $\hat{R}$ is calculated based on the ratio of within-chain variances and between-chain variances of the parameters of interest, with a value of 1 suggesting unbiasedness of the two variance estimates. To calculate $\hat{R}$, and for all the inferences in this chapter, I ran five MCMC chains with dispersed initial values and saved the sample values from the last 2500 iterations (after burn-in iterations). The value

of $\hat{R}$ is obtained for each parameter individually and as a multivariate version for all the parameters jointly (Brooks and Gelman 1998). An approximate convergence is diagnosed when the upper confidence limits of $\hat{R}$ for all unknown parameters are less than 1.005. Furthermore, for parameters that are known to have difficulty in converging, such as the precision parameters (e.g., σ_0^2), I monitor how $\hat{R}$ changes with the increase in the number of iterations. For this, $\hat{R}$ is calculated at different segments in the MCMC iterations, with the first value of $\hat{R}$ calculated with the first 50 iterations after burn-in, the second one calculated with first 100 iterations, the third one calculated with first 150 iterations and so on. By computing $\hat{R}$ in this way and by plotting its values as a function of iterations, I ensure that the single estimate of $\hat{R}$ using all iterations is not accidently close to 1.

Geweke's score: Geweke (1992) devised a standard score statistic to compare the sample means of the two segments of an MCMC chain. Under the stationarity assumption, the sample means should be normally distributed with equal means and variances. In CODA, Geweke's Z-score is calculated as the difference between two means divided by the standard error of the difference in mean. A score of more than 2 (hence, p value <0.05) does not provide enough evidence that the two means come from the same distribution, hence convergence is not diagnosed. In CODA, it is easy to obtain the Geweke's Z-score based on different segments of the first and second half of a chain (see Plummer et al. (2006) for further details). I tracked the Z-scores of all parameters using ten segments of each of the five chains.

Raftery and Lewis diagnostics: MCMC iterations inherently have autocorrelations that can cause errors in estimating the extreme quantiles and inefficient convergence. Raftery and Lewis (1992) proposed a diagnostic that estimates the minimum number of MCMC iterations required to estimate the posterior distribution of a quantile with a given precision with a given probability. For this diagnostic, CODA provides a measure dependence factor (I) calculated based on the ratio of the required sample size from the data and the minimum required sample size assuming there are zero autocorrelations. For a parameter, values of I larger than 5 suggest that there are large autocorrelations in the samples, possibly affecting the accuracy of the estimated quantiles.

5.1.4 Validation and comparison

In the following, I describe the multiple criteria that I employ to validate and compare the models.

Posterior correlations: Posterior correlations between model predictions and observations are simple and efficient measures of model performance, allowing comparisons among models. At each station, I take the median of the posterior Spearman's correlation coefficient between posterior predictions and the observations over all the calibration years (i.e., 1950–2010). The comparison of the correlations from the models M2 M3 and M4 with the baseline model M1 shows how closely they reproduce the observations at different locations.

Posterior error ratio: For each station, the absolute median posterior error ratio (ER) is calculated as:

$$ER_{M2}^{s} = \frac{\sum_{t=1}^{T} \left| \tilde{y}_{s,t}^{M2} - y_{s,t} \right|}{\sum_{t=1}^{T} \left| \tilde{y}_{s,t}^{M1} - y_{s,t} \right|} \qquad 5.4$$

where $\tilde{y}_{s,t}^{M1}$ and $\tilde{y}_{s,t}^{M2}$ are the posterior median predictions from for station *s* and year *t* from model M1 and M2, respectively. ER_{M2}^{s} compares the absolute error of model M2 with the baseline model M1, and it is calculated for M3 and M4 in a similar way as well. Values of ER_{M2}^{s} less than 1 suggest that M2 performs better than M1 at site *s*. ER is calculated for both the calibration period (T = 61) and for prediction period (T = 4; from 2011 to 2014).

Probabilistic rank skill score: For models that provide probabilistic forecasts on categorical/count outcomes such as the ones in this chapter, point error measurements, such as ER, may not do justice in comparing the models, as the predictions are not a single value, but a range of outcomes that are assigned different likelihoods of occurrence. For such cases, an alternative metric called the ranked probability score (RPS) has been suggested; for a particular observation, it measures the difference between the forecasted cumulative distribution (CDF) and the observed distribution for a certain number of discrete categories (see Weigel et al. (2007) and Gneiting and Raftery (2007) for further information). Specifically, for an observed frequency $y_{s,t}$:

$$RPS_{s,t} = \sum_{k=1}^{K} \left(P_f(Y_{s,t} \le k) - P_o(Y_{s,t} \le k) \right)^2 \quad 5.5$$

where, $P_f(Y_{s,t} \le k)$ and $P_o(Y_{s,t} \le k)$ are the forecasted and observed CDFs of *Y*. For the Poisson counts, $P_o(Y \le k) = 0$ for $k < y_{s,t}$, and 1 for $k \ge y_{s,t}$. Here, I have used k = 0 through 15 categories/counts for the comparison of the CDFs. $RPS_{s,t} = 0$ suggests a perfect forecast, while a forecast with $RPS_{s,t} > 0$ is not a perfect one. For comparing different models, one can develop what is known as ranked probability skill score (RPSS; Wilks 2011) as below.

$$RPSS_s = 1 - \frac{\sum_{t=1}^{T} RPS_{s,t}^{M2}}{\sum_{t=1}^{T} RPS_{s,t}^{M1}} \quad 5.6$$

A positive (negative) value of $RPSS_s$ suggests that M2 provides a superior (inferior) forecast than M1 for site *s*. I calculate RPSS for models M2, M3 and M4, and for both calibration and validation periods.

5.2 Results

Across much of the central United States, winter is an active season both in terms of heavy precipitation and ARs, as shown in Figure 5.1. There is large spatial variability in these frequencies, with heavy precipitation events having a higher frequency over the southeast part of the region and decreasing as we move to the northwestern part of the domain. ARs are the most frequent along the central and northeastern part of the region, resembling the storm track of extratropical cyclones passing over the central United States, with their frequency decreasing as move away from this region. There is a marked resemblance in the spatial pattern of ARs and the heavy precipitation events, in that the frequency of heavy precipitation events is generally higher in the areas where the frequency of ARs is high. Moreover, the two frequencies averaged over the entire region have a high correlation of 0.51 over the 1950-2014 period, suggesting that the frequency of ARs can be a valuable covariate for modelling the frequency of heavy precipitation events. The correlations of PNA and AO with the average frequency of heavy precipitation events over

the region are -0.39 and 0.23, respectively. PNA and AO have a higher correlation with the frequency of ARs, with values of -0.70 and -0.44, respectively. The models discussed above will further enlighten us regarding the relationships among the variables, and how it varies in space across the study region.

5.2.1 Convergence

As discussed earlier, the convergence of all the parameters in a Bayesian model is key to its inferences and predictions; all the parameters of all the four models showed acceptable convergence within reasonable computational times. First, I check $\hat{R}$ for all the parameters and summarize the results in Table 5.1. After observing satisfactory upper credible limits of less than 1.005 for all the parameters, I concentrate on the parameters that had difficulties in converging. I monitor $\hat{R}$ for these parameters of the model M2 in Figure 5.2: these results indicate convergence as the $\hat{R}$ curve approaches a value near 1.0, where it straightens and becomes parallel to x-axis as the number of iterations increase; moreover, the difference between the median of $\hat{R}$ and its upper credible limit is not large, and both remain close to a value of 1.0 along the curve, providing further evidence of satisfactory convergence.

In addition to the satisfactory values of $\hat{R}$, the Geweke's Z-score had p-values larger than 0.05, and the values of the dependence factor I rarely exceeded the limit of 5, again supporting a satisfactory convergence for almost all the parameters of all models in the five chains. I obtain similar results for the parameters of models M3 and M4.

The number of simulations and time taken for the convergence of the four models are provided in Table 5.1. As can be expected, M1 converges relatively quickly as it does not include any covariate, whereas the model M2 with a spatio-temporal covariate (i.e., number of ARs) requires twice as many iterations as M1. Understandably, M4 is the slowest model, requiring the largest number of iterations and about 24 hours to converge. As far as model M3 is concerned, I do not believe the time it takes is much smaller than M2; the two models are comparable, at least for practical implementations.

In addition to a summary of the convergence characteristics, Table 5.1 provides a general assessment of the models in terms the deviance information criterion (DIC; Spiegelhalter et al. 2002; a Bayesian analog of AIC), and effective number of parameters

(pd; Spiegelhalter et al. 2002). DIC is a measure of the out-of-sample predictive ability of the model of interest, and it penalizes the models accordingly to their complexity. Like AIC, DIC is not very useful alone but on a relative scale, it allows comparisons among different models, with the model with the lowest DIC being favored as the best. Models with lower DIC values are expected to provide improved short terms predictions. As can be seen in Table 5.1, models M2, M3, and M4 show improvements with respect to the baseline model M1, with M2 (which has ARs as covariate) showing the best performance. How significant are the differences in DIC values is not very clear, but a general rule of thumb is that a DIC difference of more than 10 can be considered large enough to support a lower DIC model over the other ones (Lunn et al. 2012). I note that the values of DIC are questionable is models such as here where the number of parameters increase as the sample size increases.

OpenBUGS provides an additional output (pd), which is taken as the 'effective number of parameters' in the model. Here, pd is calculated from the DIC for which the deviance is based on the parameters in the lowest level of the hierarchy. That is, if a hierarchical model has a parameter $\theta = f(\eta)$, then $Deviance \propto L(y|\eta)$ is used to calculate pd instead of $Deviance \propto L(y|\theta)$, where $L(y|\theta)$ is the likelihood of the data given θ. Hence, I assumed that the lowest-level parameters determine the complexity of the model, which can be argued about. More useful in random-effects models, where information is shared among the effects, and in Bayesian hierarchical models, where parameters are constrained by priors, pd provides an estimate of the actual number of parameters in a model. As per Table 5.1, M1 has the highest number of effective parameters which is equal to the number of stations *S*, because all the parameters are fixed; hence it is the most complex model. The complexity of the other three models is much lower than M1 and comparable to each other.

5.2.2 Posterior summaries

The posterior summary of the fixed effects parameters of M2, M3 and M4 are provided in Table 5.2. First note that none of the fixed effects parameters' credible intervals includes zero; hence we have strong evidence that heavy precipitation over the entire region is related to the selected covariates (i.e., ARs, PNA and AO). As per M1, the expected frequency of heavy precipitation events over the region without any AR is about

$e^{1.539} = 4.72$; ARs have a positive effect on precipitation extremes, with one additional AR resulting in about $100\left(e^{0.042} - 1\right) \sim 4\%$ increase in the frequency of heavy precipitation events over the region. Based on Figure 5.1, the annual average frequency of ARs across the region ranges from 0 to 10: if five ARs occur in a year, the frequency of heavy precipitation events can be expected to increase by about $100\left(e^{0.042*5} - 1\right)$=23%. From the model M3, the expected frequency of precipitation events is about $e^{1.79} = 6$ when both PNA and AO are zero, and the two indices have decreasing and increasing effects, respectively, on the expected frequency of precipitation extremes. A unit decrease in PNA, keeping AO fixed, increases the frequency of heavy precipitation by about $100\left(e^{.116} - 1\right) = 11\%$. Similarly, a unit increase in AO, keeping PNA fixed, can be expected to result in a 2% increase in heavy precipitation events. In model M4, the effect of the estimated AR frequency is similar to the observed AR frequency using M2 (i.e., compare β_0^{ar} and β_1^{ar} of M2 and M4, respectively). This is encouraging as it suggests that if we can estimate the frequency of ARs precisely from large-scale atmospheric features, we can then estimate heavy precipitation frequency reasonably well, without the need to identify ARs.

In addition to the frequency of precipitation, M4 allows us to measure the effect of PNA and AO on AR frequency. The effects of PNA and AO on ARs are much larger than on precipitation extremes—here, a unit decrease in PNA, keeping AO fixed, can be expected to result in a ~44% increase in ARs, and similarly, a unit increase in AO, keeping PNA fixed, results in a ~10% increase in ARs.

The overall fixed effects parameters have provided valuable information about the effects of the covariates at the regional scale. However, these effects can vary spatially across the region. To better understand this spatial variability, I show the posterior median of the AR slope coefficient at each station (i.e., median of $\beta_1^{ar} + \beta_{s,1}^{ar}$ at station *s*) from model M2 (Figure 5.3). The frequency of ARs has a positive effect at almost all the stations in the central United States, and the effect is stronger along the storm track of extratropical cyclones. Here, an additional AR can result in more than $100\left(e^{0.10} - 1\right) = 10\%$ increase in heavy precipitation events, and the increase could be more than $100\left(e^{0.10*5} - 1\right) = 65\%$ if

five additional ARs occur over these stations. The spatial variations in PNA and AO slope coefficients (i.e., medians of $\beta_1 + \beta_{s,1}$ and $\beta_2 + \beta_{s,2}$ at station s) of models M3 and M4 are shown in Figure 5.4. As described above, these models have spatial structures on the slope coefficients, with the goal of improving upon independent at-station Bayesian models due to the pooling of information across the neighboring stations. I do not intend to extensively compare the M3 slope coefficients with at-station models' coefficients, but a visual comparison in the top two panels of Figure 5.4 shows a smoothing effect on the coefficients in M3 as opposed to at-station models. In these panels, PNA and AO show differing effects across the region; however, the contrasting regions are more clearly delineated in M3, an advantage of providing spatial structure to the slope coefficients.

Focusing on the middle panels, PNA has a negative effect over the central and northeastern parts of the central United States and a positive effect over the south western part of the region. Keeping AO fixed, a unit decrease in PNA magnitude can result in a 22% increase in heavy precipitation events over the northeastern areas, when a similar increase in the frequency can be expected at the southwestern stations. Considering the effects of AO, an increase in its magnitude generally tends to increase the frequency of heavy precipitation events; the increases, however, are larger over the western part of the region, where a unit increase in AO magnitude can result in more than a 10% increase in the frequency of heavy precipitation events.

PNA and AO slope coefficients do not seem to have large spatial variations for AR frequency (Figure 5.4, bottom panels) compared to what is observed for precipitation extremes. The two indices have, respectively, decreasing and increasing effects on the AR frequency over most of the stations, except for the stations south of the Appalachian Mountains, where the two indices have little to no effect on their frequency. The effect of the two indices is stronger on ARs than on precipitation extremes. For a fixed AO, a unit decrease in PNA can increase the frequency of ARs by more than 50% at some stations, while a unit increase in AO (fixing PNA) can result in more than 15% increase in AR frequency.

After understanding the effects of the covariates on heavy precipitation and ARs, I focus on the relationships among different estimated random effects. Table 5.3 presents the posterior correlations of the random parameters in the three models. In model M2, the

correlation between the intercept and the slope parameter corresponding to ARs is negative (median $\rho_{0,1}^{ar}$=-0.349), suggesting that stations that have lower values of the intercept (i.e., lower expected frequency of heavy precipitation events without any AR) tend to have larger AR slopes (i.e., more affected by AR occurrences). On the other hand, stations with higher values of the intercept have lower slope values for ARs (i.e., they are less affected by ARs).

For M3, the correlation of the intercept with the PNA slope coefficient $\rho_{0,1}$ is small (-0.02), while it is larger and positive with AO (0.141) with a high probability. Hence, the stations that have larger intercepts tend to have larger AO slopes. The correlation between AO and PNA (median $\rho_{1,2}$=0.186) suggests that stations generally provide similar response towards PNA and AO. Viewed differently, an increase in the frequency of extremes due to the negative PNA can be, for example, offset by a decrease in AO.

As expected, for M4 the relationship between the intercepts and slopes of the estimated ARs ($\rho_{0,1}^{ar}$) is similar to the one in M2. However, unlike precipitation extremes, the relationship between the intercepts and slopes of PNA is negative (median $\rho_{0,1}$ = -0.2) with a high probability for the AR frequency, which suggests that sites that have higher intercept tend to be less affected by PNA, and vice versa. The other two correlations ($\rho_{0,2}$ and $\rho_{1,2}$) are negligible.

5.2.3 Validation and comparisons

Earlier, I presented the DIC criterion as an important measure that provides information about the overall fit of the models, leading to M2 as the best model. In this section, I expand such analysis using the measures discussed earlier in section 5.1.4. Figure 5.5 provides the posterior correlation between observed and posterior predicted frequency of heavy precipitation at each station. From this figure, model M1 performs poorly, and almost all the stations have near-zero correlations; the reason is that the intercept parameter for each station is concentrated near its climatological value, resulting in poor posterior predictions that do not vary according to the prevailing weather patterns.

The other three models have high correlations over the central and northeast regions of the central United States, which are the areas with the highest frequency of ARs (Figure 5.1). The correlations over the other regions are relatively weak. In comparing the three models, M2 performs better over several stations, especially the stations located along the AR track.

The second measure I discuss for the comparison of the models is ER, shown in Figure 5.6 for both the calibration and prediction periods. In the calibration period, all three models perform better than the baseline model over a region which experiences a high AR frequency; over the other locations, the models perform at least as good as the baseline model. Among the three models, M2 shows the best performance over the region covering Illinois, Indiana, Ohio, Kentucky, Tennessee and the surrounding locations, where the posterior absolute error at some stations is about 30% smaller than the baseline model. In the prediction period, however, the performance is not always better than the baseline model. M2 performs better than the baseline model over many stations, but the performance lacks the regional coherence that was observed in the calibration period. Nevertheless, this model performs better than models M3 and M4.

As discussed earlier, measures based on point estimates may not be the best choice for probabilistic models; therefore I show RPSS for the three models in Figure 5.7. Similar to the above comparisons, all the models show improvement upon the baseline model in the calibration period, and for most of the stations in the prediction period. While M3 performs reasonably well over the northern and northeastern areas of the study domain in the prediction period, its performance is worse than the baseline over regions such as Tennessee and Kentucky, where the performance of these models was good in the calibration period. Among the three models, M2 has the best performance at almost all the stations both in the calibration and prediction periods. For these models, a larger number of stations show better performance in the prediction period, for example over eastern Iowa and Ohio (Figures 5.6-5.7).

5.3 Discussion and conclusions

In this chapter, I modelled the frequency of winter heavy precipitation events at 426 long-term stations over the central United States. In the Bayesian hierarchical modeling

framework employed here, the frequency of heavy precipitation events is conditioned on large-scale atmospheric modes (PNA and AO) and ARs; all the three covariates have high correlations with regional heavy precipitation over the past 65 years of record. Three models were developed and compared with a baseline model with no explanatory variable: all three models showed improved performance over the baseline model. Furthermore, the results of the model comparison showed that the model with ARs as covariate outperformed the other ones, including the one that had PNA and AO as covariates. This indicates that precipitation extremes over the central United States have a more direct relationship with ARs, than with PNA and AO.

PNA and AO have a more direct relationship with ARs as suggested by their correlations, and more thoroughly by model M4 in which I conditioned the AR frequency on PNA and AO magnitudes. These results support my assumption that ARs play a leading role in producing heavy precipitation events over the central United States, whereas PNA and AO patterns play a major role in the development of ARs over the region.

Taking a closer look at the results from M4, the relationship between ARs and heavy precipitation events is well captured, even though the covariate of this model is the *estimated* mean frequency of ARs from PNA and AO; moreover, the relationship between the frequency of ARs and the two climate indices is consistent with physical interpretations—these two points are very encouraging. The only issue with this model is the computational time it takes to converge, but this can be greatly improved with a simple and a reasonable assumption. Instead of having station-wise AR frequency, one can use regional AR frequency as the covariate, which significantly reduces the dimensionality of the model, and as such should lead to significantly faster convergence. This model, I believe, will compare favorably with the model with the *observed* ARs as covariate, especially over the region where AR frequency is high. For the prediction of the frequency of winter ARs and heavy precipitation events, this has important implications. There is no need to predict the seasonal AR frequency using global climate models (a challenging task) and there is no need to identify ARs (which is again computationally intensive). The major challenge, however, is to make skillful seasonal predictions of PNA and AO.

For future studies, it is possible to improve the statistical models for heavy precipitation events such as the ones here. Additional parameters that capture the variability in heavy

precipitation events, not explained by any systematic variations, need to be examined, such as unstructured random error terms $H(s,t) \sim N(0,\sigma^2)$. However, from my experience with the data, for the variance parameter of this term σ^2, Gibbs sampling convergence is very inefficient and the parameter does not converge easily. A potential solution to this problem is the introduction of an annually varying variance term (i.e., $H(s,t) \sim N(0,\sigma_t^2)$) as used by Waller et al. (1997) in disease mapping. Further improvements are possible from improved understanding of the physical mechanisms that cause heavy precipitation over the region. For example, in addition to ARs and large-scale atmospheric patterns, some measures of other heavy precipitation mechanisms, such as convective available potential energy (CAPE) for convective precipitation, can be added as covariates.

5.4 Figures Chapter 5

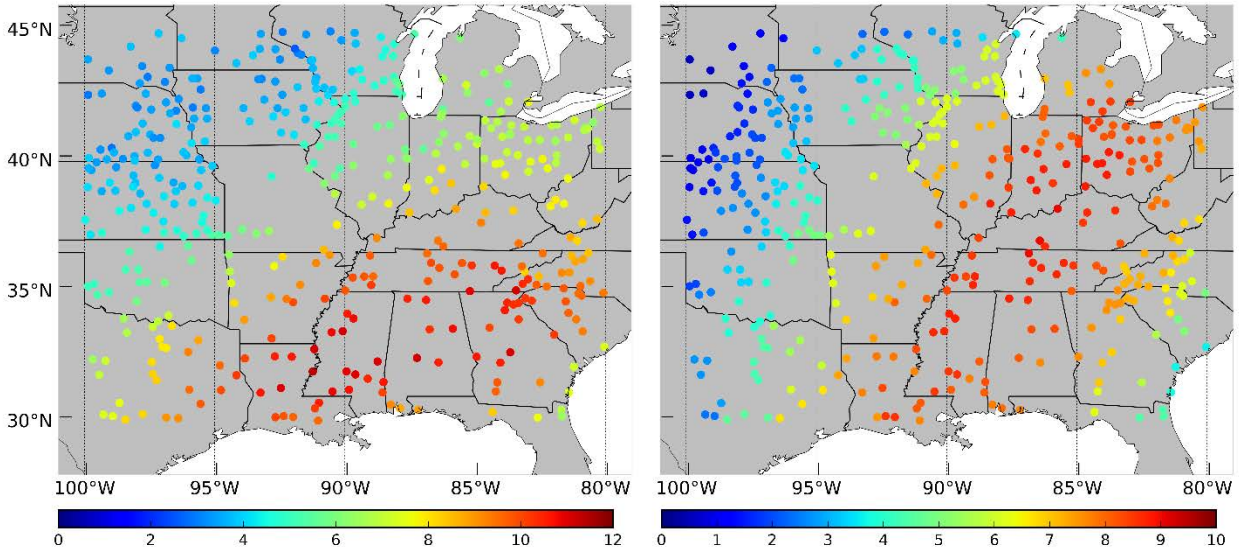

FIG. 5.1: Average frequency of heavy precipitation events (left panel) and ARs (right panel) across the central United States during winter for the period 1950–2014.

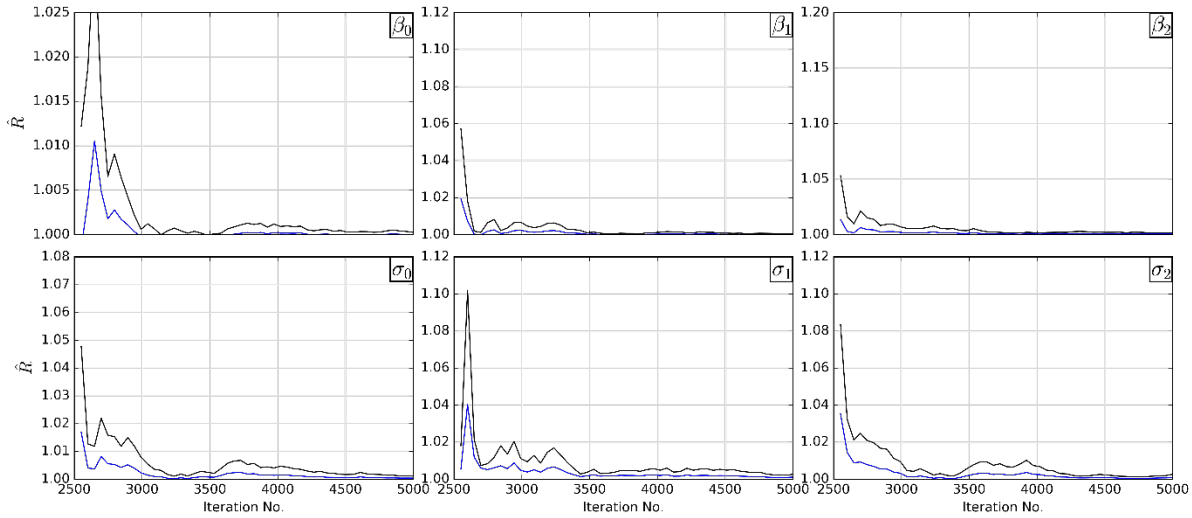

FIG. 5.2: Gelman and Rubin shrink reduction Factor $\hat{R}$ for model M3. The blue line shows the median of $\hat{R}$ and the black line shows the upper credible limit (97.5%).

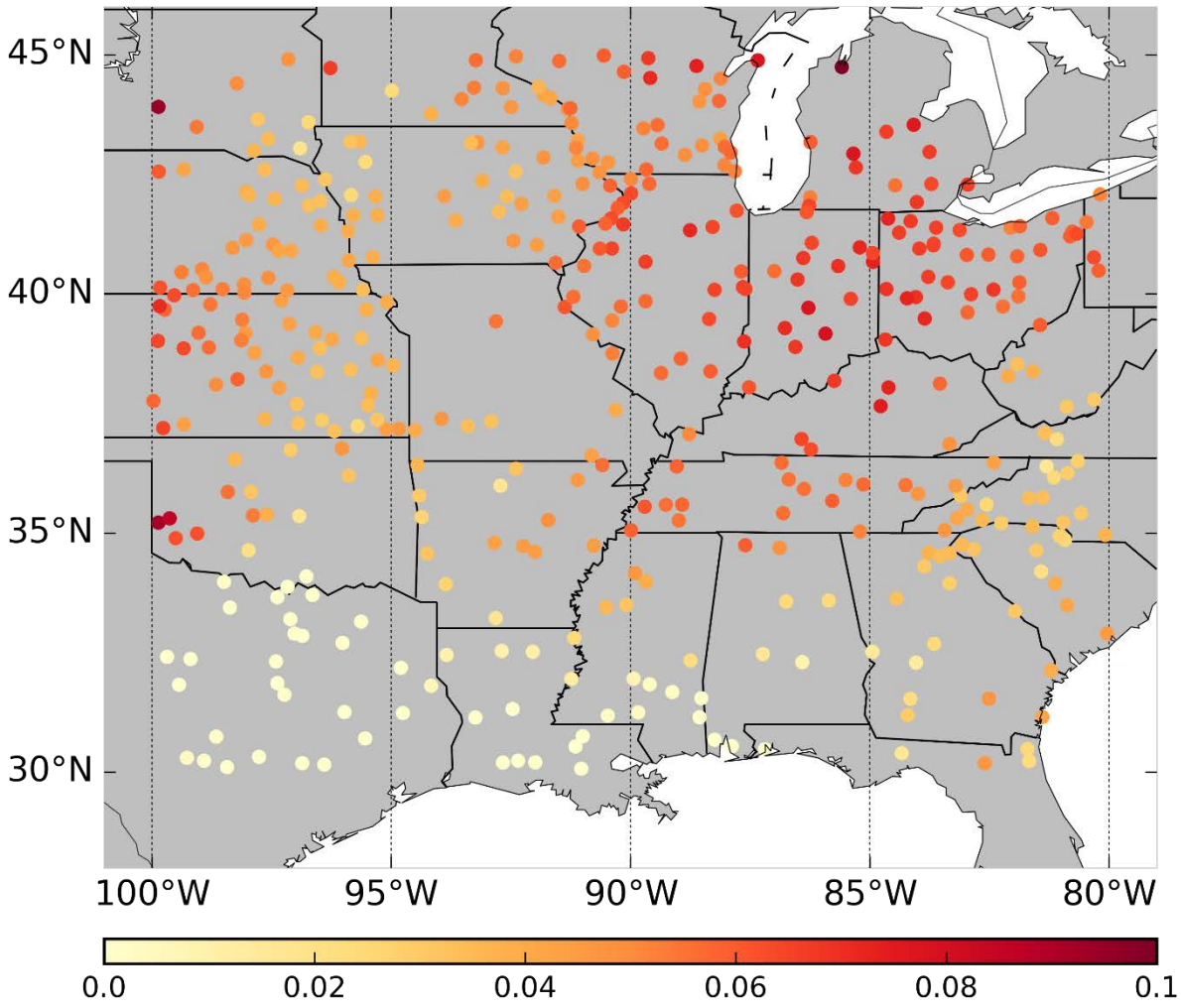

FIG. 5.3: Posterior median slopes of the covariate AR for modelling the frequency of heavy precipitation events in model M2.

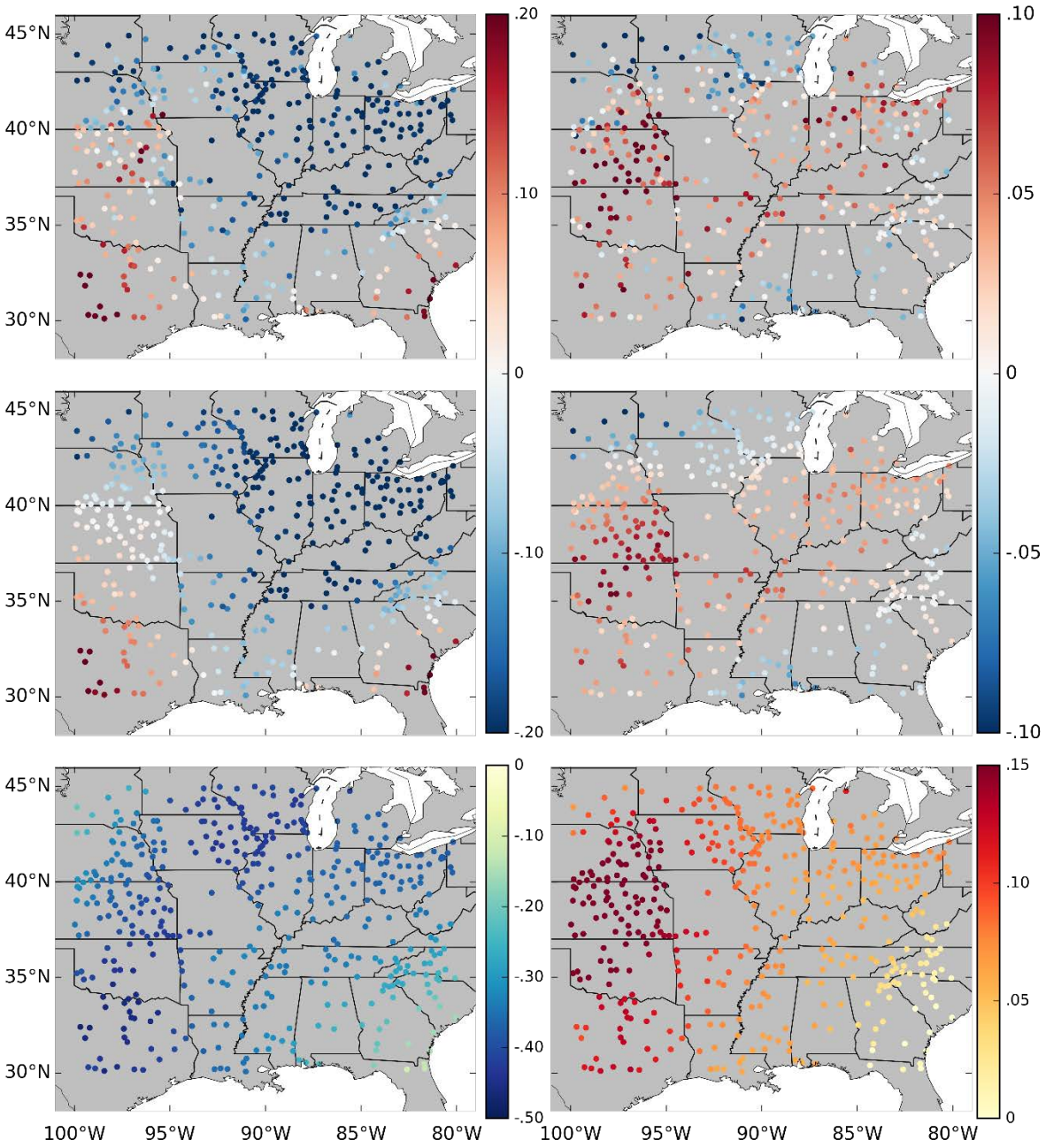

FIG. 5.4: Posterior slopes of PNA (left panels) and AO (right panels). The top panels show the slopes based on the independent at-station Bayesian models for the frequency of heavy precipitation, the middle panels are the slopes based on model M3, while the bottom panels are the slopes for the frequency of ARs using model M4.

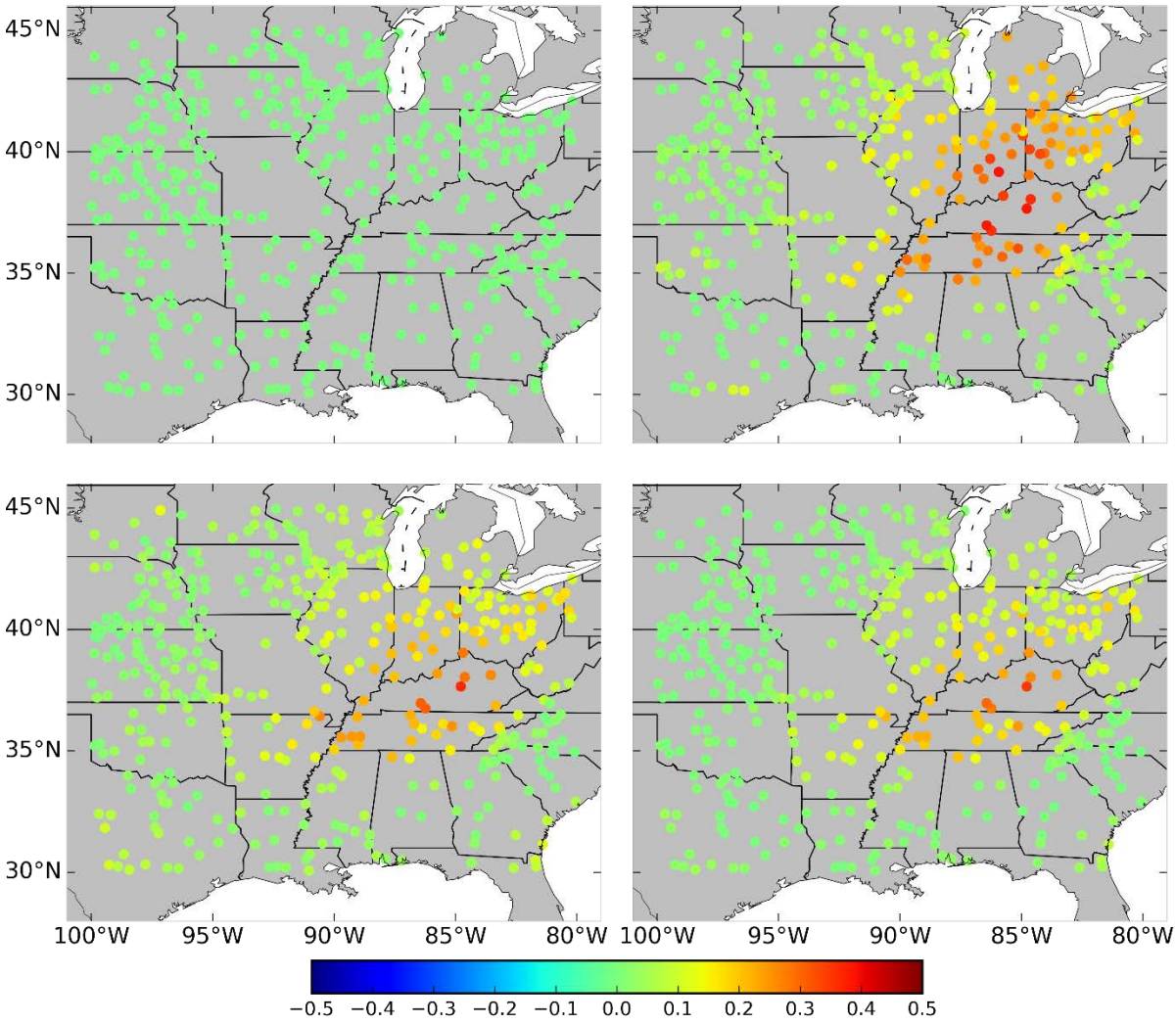

FIG. 5.5: Posterior correlations between the observed and posterior predicted frequency of heavy precipitation using models M1 (top-left panel), M2 (top-right panel), M3 (bottom-left panel), and M4 (bottom-right panel)

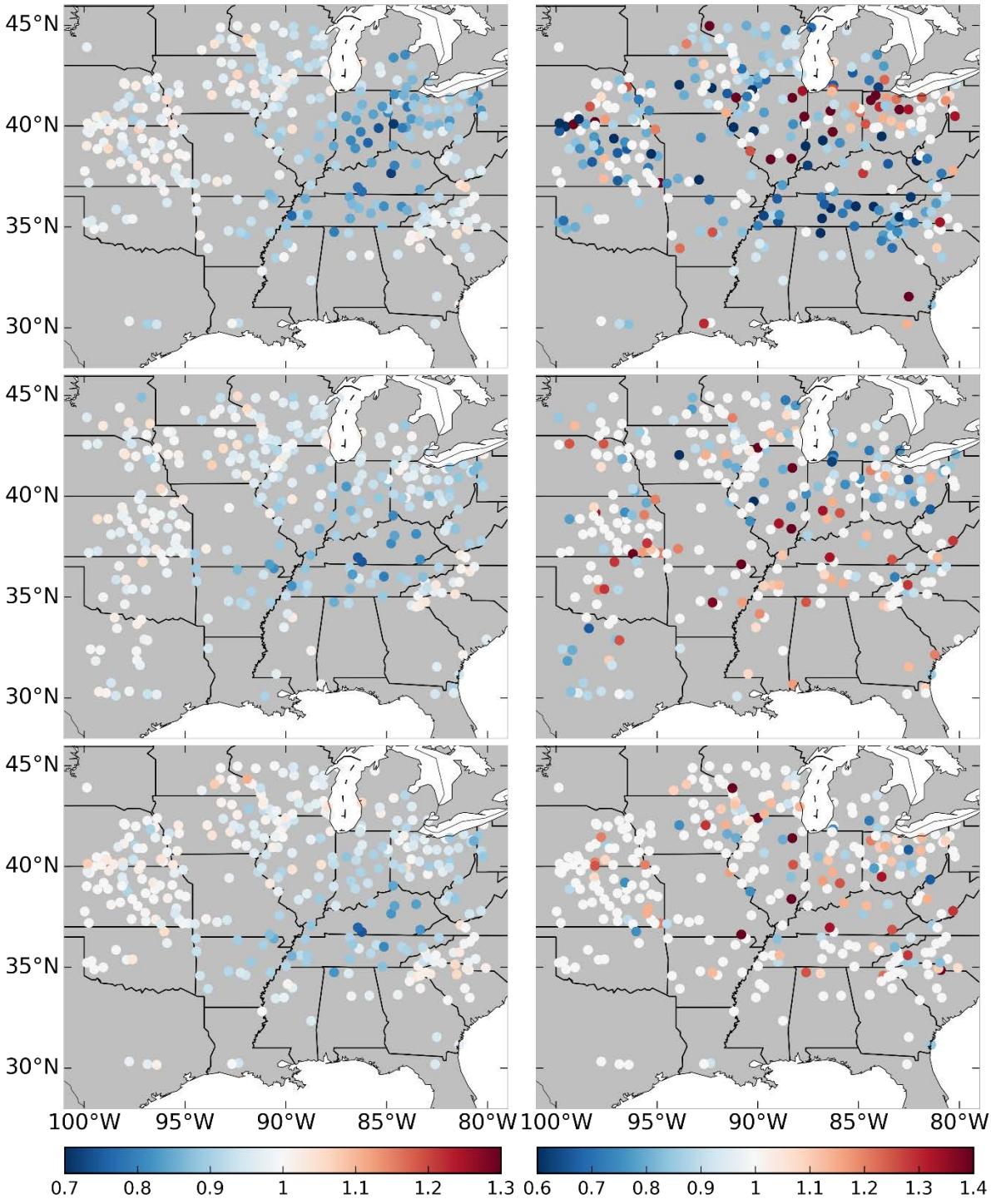

FIG. 5.6: Posterior error ratio (ER) for the calibration period (left panels) and the prediction period (right panels). Top panels correspond to model M2, the middle panels to model M3, and the bottom panels to model M4. For M2 and M4, only stations for which the posterior

95% credible intervals of the AR slope parameters do not include zeros are plotted; for M3, only the stations for which the credible interval of either PNA or AO slopes do not include zeros are plotted.

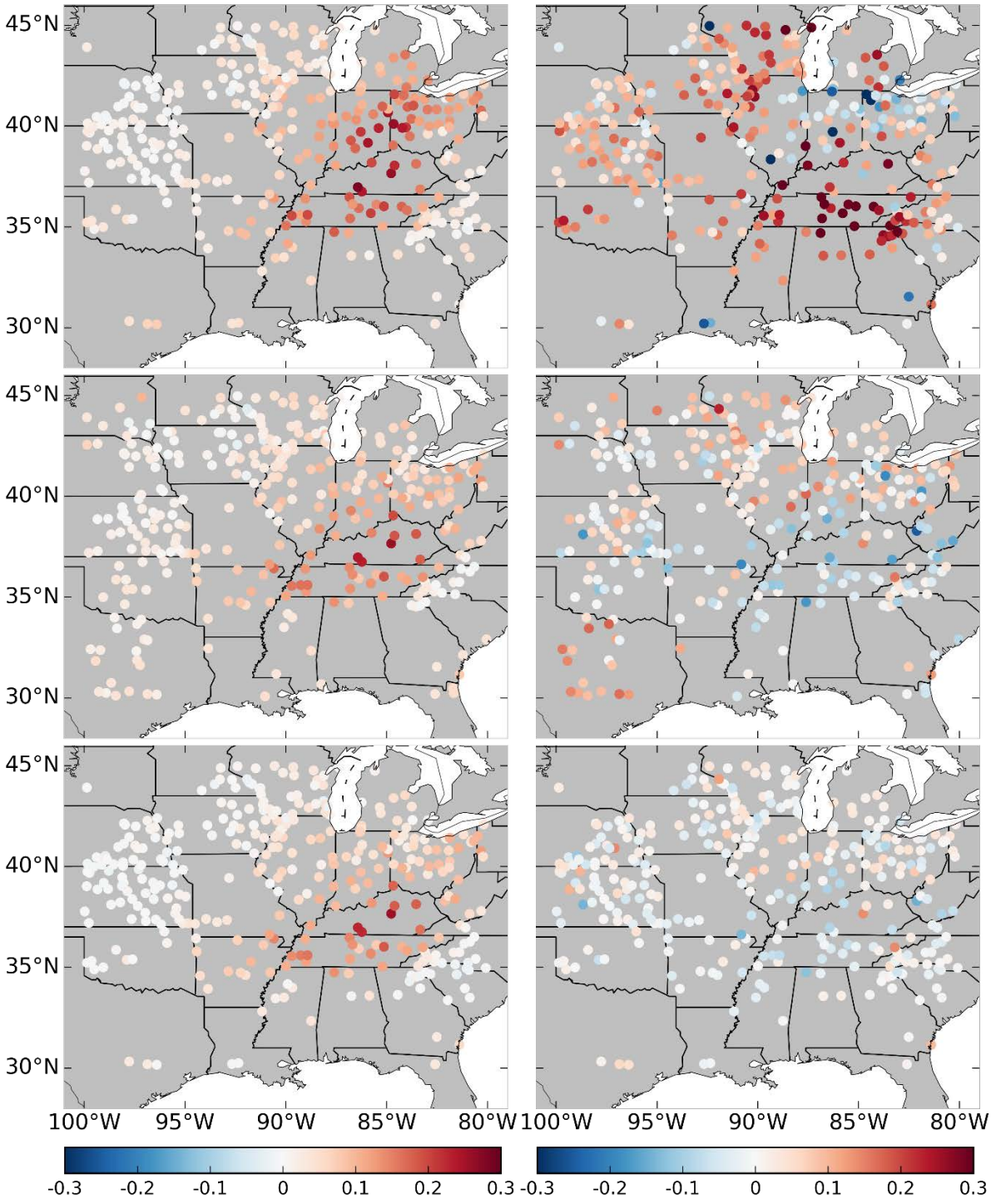

FIG. 5.7: Similar to Figure 5.6, but for the Ranked probability skill score (RPSS). Positive (red) values indicate better performance than the baseline model.

5.5 Tables Chapter 5

TABLE 5.1: Characteristics of the model calibration. The terms "DIC" and "pd" are the deviance information criterion and the effective number of parameters in the model, respectively. For this table, the total number of valid observations in the response matrix is Y426×61 = 25053 and in the prediction period Y426×4 = 1560. For all the models, five chains with different initial values of all the parameters are run. See text for details.

Model	MCMC Iterations		Time taken (minutes)	Max. $\hat{R}$	pd	DIC
	Total	Burn-in				
M1	5000	2500	18.39	1.003	425.7	121500
M2	10000	7500	116.07	1.02	32.31	118100
M3	5000	2500	94.85	1.005	22.09	118600
M4	30000	27500	1416.67	1.02	26.10	119200

TABLE 5.2: Posterior credible intervals of the fixed overall parameters of models M2, M3 and M4.

Parameter	2.5%	25%	50%	75%	97.5%
M2					
β_0^{ar}	1.539	1.547	1.552	1.556	1.564
β_1^{ar}	0.039	0.041	0.042	0.043	0.044
M3					
β_0	1.79	1.793	1.795	1.797	1.8
β_1	-0.116	-0.110	-0.107	-0.104	-0.010
β_2	0.014	0.018	0.019	0.021	0.024
M4					
β_0	1.563	1.567	1.569	1.571	1.575
β_0^{ar}	1.531	1.544	1.551	1.558	1.572
β_1	-0.371	-0.378	-0.362	-0.358	-0.352
β_1^{ar}	0.033	0.036	0.038	0.040	0.042
β_2	0.085	0.090	0.090	0.093	0.096

TABLE 5.3: Posterior credible intervals of the posterior correlations among the random intercepts and slopes of the three models M2, M3 and M4.

Parameter	2.5%	25%	50%	75%	97.5%
M2					
$\rho_{0,1}^{ar}$	-0.452	-0.386	-0.349	-0.311	-0.239
M3					
$\rho_{0,1}$	-0.169	-0.072	-0.020	0.033	0.130
$\rho_{0,2}$	0.002	0.094	0.141	0.187	0.275
$\rho_{1,2}$	0.026	0.132	0.186	0.238	0.332
M4					
$\rho_{0,1}^{ar}$	-0.541	-0.476	-0.440	-0.402	-0.325
$\rho_{0,1}$	-0.354	-0.255	-0.200	-0.140	-0.018
$\rho_{0,2}$	-0.183	-0.080	-0.022	0.033	0.143
$\rho_{1,2}$	-0.106	-0.003	0.051	0.103	0.203

CHAPTER 6

ON THE SKILL OF NUMERICAL WEATHER PREDICTION MODELS TO FORECAST ATMOSPHERIC RIVERS OVER THE CENTRAL UNITED STATES[4]

Given the significant role ARs play in the regional and global water cycle, it is clear from the previous chapters that accurate forecasts of these events can be beneficial to forecast precipitation, improve preparedness against potential floods and to plan optimal policies in case of prevailing droughts. In Chapters 5 and 6, I focused on the statistical modelling of ARs and extreme precipitation over the central United States at the seasonal and sub-seasonal scales. However, advances in scientific computing and atmospheric science have made it possible to increase the temporal resolution and to provide short-term forecasts based on numerical weather prediction (NWP) models. NWP models provide sub-seasonal forecasts of many important atmospheric variables at uniform spatial and temporal resolutions over the entire globe. These variables include q, u- and v-wind, which are used to calculate IVT (hence forecasts of ARs), and IWV as direct outputs. This chapter focuses on evaluating the skill of NWP models in forecasting ARs over the central United States using IVT and IWV. IWV observations are obtained from satellite measurements and are also a product of global atmospheric reanalysis datasets. IWV's ready availability and direct applicability have made it an attractive option for studying these events. The primary reason to evaluate AR forecasts based on IWV, in addition to IVT, is to compare the two variables in terms of AR identification skills.

By examining the skill of the state-of-the-art NWP models in forecasting AR occurrences, I will provide basic information on model outputs at different lead times. Specifically, I am concerned with the accuracy of the forecasting of AR occurrences, the location of the forecasted ARs, and how far into the future the NWP models can skillfully forecast these events. In addition to the examination of how predictable these events currently are, the results from this chapter could lead to a new paradigm in the evaluation

[4] Chapter adopted from Nayak, M. A., G. Villarini, and D. A. Lavers, 2014: On the skill of numerical weather prediction models to forecast atmospheric rivers over the central United States, Geophysical Research Letters, 41, 4354–4362, doi:10.1002/2014GL060299.

of rainfall forecasts over the central United States by examining the skill of NWP models in forecasting precipitation depending on whether an AR is forecasted or not. To my knowledge, only Wick et al. (2013) evaluated the skill of five NWP models in forecasting AR activity over the northeastern Pacific Ocean and west coast of North America up to a 10-day lead time. They focused on three cold seasons and found a decrease in model skill in forecasting AR activity and location with increasing lead time. The accuracy of AR forecasts is unknown over other areas including the central United States, where ARs represent an important flood agent.

6.6 Data and Methods

6.6.1 Data

I use IVT and IWV fields from MERRA to create the AR reference datasets. For forecast verification, I focus on the period from 2007 to 2013 and consider the control forecasts of NWP models from five modeling agencies. The modeling agencies are (in brackets is the period for which these data were available at the time these analyses were performed): 1. ECMWF (2007–2013); 2. United Kingdom Met Office (UKMO) (2008–2013); 3. NCEP (2008–2013); 4. China Meteorological Administration (CMA) (2008–2013); and 5. Canadian Meteorological Center (CMC) (2008–2013). The datasets are obtained from the Observing System Research and Predictability Experiment (THORPEX) Interactive Grand Global Ensemble (TIGGE, Bougeault et al. 2010) archive (http://apps.ecmwf.int/datasets/data/tigge/). Most of the models provide forecasts at 0000UTC and 1200UTC; only forecasts made at these times are used for verification. ECMWF and UKMO provide forecasts up to a lead-time of 360 hours, CMC and NCEP up to 384 hours, and CMA up to 240 hours. All models provide forecasts in six-hourly steps and I retrieved the data interpolated onto a horizontal grid resolution of $0.5^{\circ} \times 0.5^{\circ}$.

As an example, Figure 6.1 compares IVT and IWV for 0000UTC June 06, 2008 from MERRA with ECMWF forecasts (analysis time, 5-day and 10-day lead times). MERRA shows a large plume of moisture over the central United States, with IWV values exceeding 4cm, and IVT values larger than $1000 kgm^{-1}s^{-1}$. We can observe that an AR is better defined using IVT than IWV, with the cyclonic flow around the low pressure system over South Dakota/Nebraska clearly visible. The analysis time step captures well the features in

MERRA, even though the IVT and IWV values tend to be larger than in MERRA. As the lead time increases to five and ten days, the AR structure is not captured in the IWV or IVT.

6.6.2 AR identification

The AR detection follows the algorithm described in Chapter 3, with a minor simplifications that the search is made only southwards from 40°N. For MERRA, a daily IWV/IVT threshold is calculated by taking the average daily IWV/IVT at all grid points between 85° and 100°W at 40°N, and then finding the 85th percentile of the distribution of daily maximum values in the longitude band. Because of the limited sample size, the 85th percentile for a given day of the year is computed using a 31-day window of the maximum IVT/IWV (along 100°W–85°W at 40°N) centered on the day of interest (e.g., for March 1st, I compute the 85th percentile of all the IVT/IWV values between February 14th and March 16th). For seven years of data, this means computing the 85th percentile out of 217 values. I computed the threshold for the models using two different approaches: one in which I find the lead-dependent threshold for all the models, and one in which I use the threshold values from MERRA. The results related to the forecast verification using these two different methods will allow an assessment of how critical the threshold selection is. The IWV and IVT thresholds for MERRA are 3.2cm and 431.5$kgm^{-1}s^{-1}$, respectively. After removing the tropical cyclones (a tropical-cyclone day is considered a day in which the center of circulation of an identified tropical cyclone is within the domain 25°–50°N and 70°–110°W), 762 and 625 ARs are identified in MERRA from 2007–2013 using IWV and IVT, respectively. Figure 6.2 shows the IWV and IVT threshold variations with lead time for all the models. An evident feature of IWV and IVT thresholds is the decrease in threshold value with forecast lead time, pointing to a drying out of the models at longer forecast lead times. With the exception of CMA, all the models tend to exhibit a similar pattern up to about the ten-day forecast lead time, and then start diverging. The threshold values of CMA are much lower than in the other models after about one-day lead time. Having a threshold varying with forecast lead time is in essence a simple way of accounting for biases inherent in models.

Given the thresholds, the AR identification algorithm is run on MERRA and on all the forecast lead times of all the models. Unlike in the earlier chapters, when defining ARs I

do not include a temporal persistence criterion, but rather focus just on AR time steps. I consider ARs of length 17 grid points down from 40°N, approximately equal to 950km, or more. After the identification step, a catalog of the time of AR occurrences in both MERRA and each of the models is obtained and saved along with the location of AR major axis, defined here as the latitude and longitude of maximum IWV/IVT value along the AR.

6.6.3 Verification measures

I am interested in estimating the skill of the models in terms of the occurrences and non-occurrences of AR events in the models' forecasts and reference data, and the location difference of ARs forecasted in the models and in MERRA. The occurrences and non-occurrences of AR events can be considered as a deterministic binary process, the verification of which is usually performed with the help of a contingency table (see for example, Jolliffe and Stephenson (2012)). In a contingency table, the hit rate a is the number of events that were forecasted as well as observed (because of the use of a reanalysis dataset like MERRA, here "observation" is intended as "reference") during the period of analysis (e.g., 2007 to 2013 for ECMWF); false alarms b is the number of events that were forecasted but not observed; misses c is the number of events that were not forecasted but actually did happen, and correct rejections d is the number of events that were not forecasted and did not happen. Some of the simplest measures of skill verification are Hit rate (H) and False alarm rate (F):

$$H = \frac{a}{a+c} \tag{6.1}$$

$$F = \frac{b}{b+d} \tag{6.2}$$

where H is ratio of the number of ARs forecasted to the total number of ARs observed; F is the ratio of incorrect forecasts to the total number of non-AR instances. H and range F range from 0 to 1.

In practice, verification measures need to have certain desirable properties. These properties include equitability (Gandin and Murphy 1992) , propriety, and non-degeneracy, among others. An equitable score is one that gives all random forecasting systems and constant forecasting systems the same expected score, thereby making it possible to distinguish them from good forecasting systems. This also prevents other undesirable

properties such as bias due to constant forecasting of certain events. Propriety is a property of a verification measure that attempts to avoid the possible hedging by the forecaster i.e. providing a forecast different from the actual forecast in order to increase the expected score (Jolliffe 2008). Non-degeneracy of verification measures for rare events is desirable as otherwise the score goes to zero as the rarity of the event increases giving a wrong impression of model performance (Stephenson et al. 2008). Hit rate and false alarm rate lack most of the desirable properties; hence I consider a more apt verification measure called symmetric extremal dependence index or *SEDI* (Ferro and Stephenson 2011). *SEDI* is calculated as:

$$SEDI = \frac{\ln F - \ln H + \ln(1-H) - \ln(1-F)}{\ln F + \ln H + \ln(1-H) + \ln(1-F)} \qquad 6.3$$

It possesses most of the desirable properties (see Table 3.4 in Jolliffe and Stephenson (2012)). *SEDI* ranges from -1 to 1, with 0 being the expected score for a random forecasting system and negative being the score of forecasts worse than random. For the case of ECMWF at the analysis time step using IWV to identify ARs, a = 180, b = 206, c = 196, and d = 1975. We calculate H = 0.479, F = 0.094, and the corresponding *SEDI* = 0.566. For more discussion about verification measures, and their meta-verification, consult Gandin and Murphy (1992), Jolliffe (2008), Stephenson et al. (2008), and Jolliffe and Stephenson (2012), among others.

The skill of models in terms of location error is here defined as the average root mean squared error (*RMSE*) between the location of the AR major axis forecasted by the models and MERRA's AR major axis over all the forecasted as well as MERRA-based ARs. MERRA and the models have the same latitudinal resolution, so the difference in location of the AR major axes comes only from the differences in longitudes. I compute the location error *LE* as follows:

$$LE = \frac{\sum_{a}\left(\sum_{i=0}^{17}\left(LO_i - LM_i\right)^2 / 18\right)^{\frac{1}{2}}}{a} \qquad 6.4$$

where *LE* is the location error, a is the number of ARs from MERRA as well as forecasted, LO_i and LM_i are respectively the longitude of the AR in MERRA and in the

models for the i^{th} latitude point below 40°N. Because of the requirements in terms of AR lengths, comparison is performed only for the 18 grid points.

6.7 Results

The evaluation of the NWP models provides some useful results and interesting insights. To concisely present the results, I take advantage of the relative operating characteristic (ROC), a plot of hit rate against false alarm rate. On this plot, I overlie contours of *SEDI* which essentially represent the skill score. Figure 6.3 presents the verification results for all the models, both in terms of AR occurrence (left panels) and location errors (right panels) when using a lead-dependent threshold. Top and bottom panels of the figure are based on IWV and IVT, respectively. All the models tend to perform equally at initial forecast lead times. The skill score of the models using IVT (*SEDI* about 0.80) is much higher than using IWV (*SEDI* about 0.60). This is a result of high hit rate and small false alarm rates in IVT. The inclusion of the transport component in the identification of ARs helps to precisely confine the structure of ARs to narrow bands, which does not happen as clearly in IWV (compare also Figure 6.1, panels a and e). The implication is a higher skill of models when detecting ARs based on IVT, with a recommendation to use IVT to identify ARs from NWP models.

The skill of the models decreases with the increase in forecast lead time, with an increase in false alarm rate and a decrease in hit rate (overall decrease in *SEDI*). The forecast skill is better retained for increasing lead time when using IVT, and it becomes worse than random systems for lead times more than ten days. On the other hand, when using the IWV all the models tend to behave like random forecasting systems after seven/eight days. The points are much more tightly distributed on the ROC when using IVT and it is difficult to identify a model that stands out consistently from the others. Conversely, when the identification is based on IWV there is a much larger scatter and some ranking is possible. Overall, the ECMWF has the highest hit rate and the smallest false alarm rate, while CMC has a lower performance.

After examining the skill of these models in forecasting AR occurrences, I focus on whether the models place ARs in the correct location once they are identified (Figure 6.3, right panels). At short lead times, the models tend to forecast the major axis of the ARs

with an average error of about 1.2 decimal degrees (about 90km). The longitudinal resolution of MERRA and the models differ by about 0.167 degrees; this amount of location error may be regarded as zero error. Considering that here I focus on the AR major axis, and that the width of these events is of the order of a few hundred kilometers, these location errors do not hinder significantly the capability of these models in forecasting AR impacts. The ECMWF model tends to perform better than other models at shorter lead times, both in IWV and IVT. The location errors based on IVT at shorter lead times are slightly smaller than for IWV; the location errors increase significantly after a few days forecast lead time and go beyond 3 decimal degrees for a forecast lead time of about a week.

In addition to examining the results obtained using a lead-varying threshold, I consider the case in which the MERRA threshold values are used to identify ARs in the models. I summarize these results in Figure 6.4. As expected based on Figure 6.2 (see how the thresholds for the models cross the ones from MERRA around one week), at short lead times I observe a higher hit rate and higher false alarm rate, and vice versa is the case for longer lead times. There is no major change in the *SEDI* skill score, with a small increase for IVT at short lead times. I notice a tendency towards an increasing scatter in the results. As far as the location error, there is not much difference, primarily because it is based only on those events that are identified in MERRA as well as forecasted, which mostly remain the same.

Wick et al. (2013) examined the skill of NWP models in forecasting AR activity over the U.S. West Coast. Using IWV for the identification, they found that the hit rate of the models at forecast lead times of one day and ten days are 0.8 and 0.6, respectively; the respective false alarm rates are 0.27 and 0.45. These values correspond to *SEDI* 0.69 and 0.21 for one-day and 10-day forecast lead times, respectively. These *SEDI* values are higher than those in this study (about 0.55 and 0 for one-day and ten-day lead times, respectively). While here I cannot confirm why our results differ, I suggest that a possible reason is the more complicated atmosphere—land surface processes over the U.S. Midwest. Moreover, I am focusing on AR identification over the entire year, rather than only the cold season. The performance of all the models in Wick et al. (2013) is similar,

which is not the case in this study as far as IWV is concerned (models perform similar to each other when using IVT).

6.8 Discussion and Conclusions

This study examines the skill of five state-of-the -art NWP models in forecasting ARs over the central United States over the period 2007–2013. I found that NWP models are skillful at forecasting AR occurrences at short lead times (on the order of a few days). They also perform better and retain skill for longer lead times when AR identification is based on IVT rather than on IWV. Therefore, I recommend using IVT rather than IWV for identifying ARs, as also suggested by Rutz et al. (2014).

The location errors of the ARs' major axes are about 100km at short forecast lead times, increasing up to 400–500km for forecast lead times longer than ten days. Given the width of these events (on the order of few hundred kilometers), a location error of about 100km would still make these forecasts of potential use for flood forecasting. All the models performed similarly when using IVT which makes it difficult to rank them. Overall, these models can be used with some degree of reliability for a forecast lead time up to about a week or less. Their performance becomes worse than a random forecasting system after a forecast lead time of about ten days. Based on these results, the use of a model-specific lead-dependent threshold is not critical for the identification of ARs based on IVT. This holds true for this region and over the study period. It is important, however, to select a threshold that is a reflection of the climatology of the moisture transport in the region. Moreover, because of seasonal variability in atmospheric moisture and transport, resorting to a seasonally-varying threshold could be beneficial but would require a larger sample size to obtain more robust results.

6.9 Figures Chapter 6

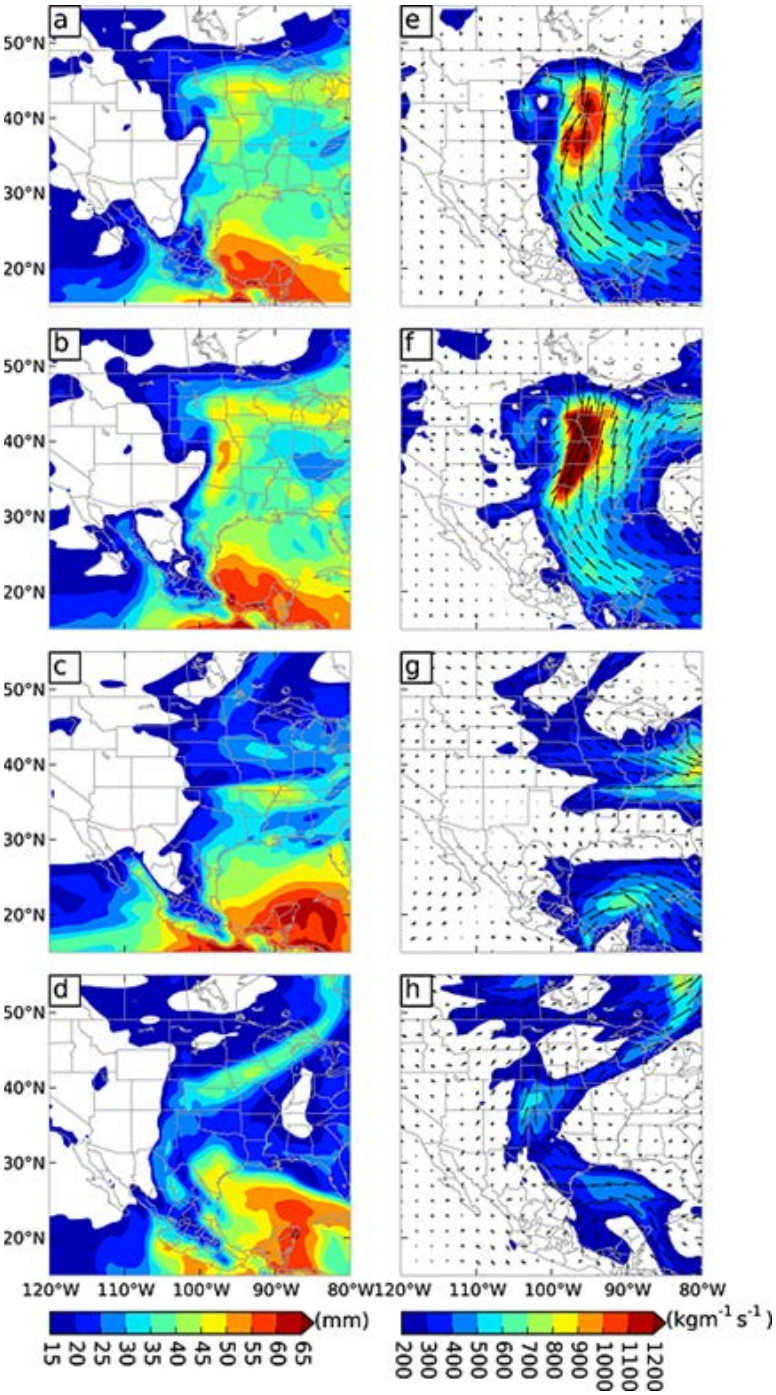

FIG. 6.1: Comparison of MERRA and ECMWF forecasts of IWV (left panels) and IVT (right panels) at 0000UTC 6 June 2008. The results for MERRA are in the top-panels. The ECMWF results are for the same time as MERRA but forecasted at different lead times.

Panels b and f refer to the analysis time step for the ECMWF model run; the 5-day forecasts are shown in panels c and g, while the 10-day forecasts are in panels d and h. The arrows in right panels represent the IVT vectors, the size of arrows depicts the magnitude of IVT as represented in the colormaps.

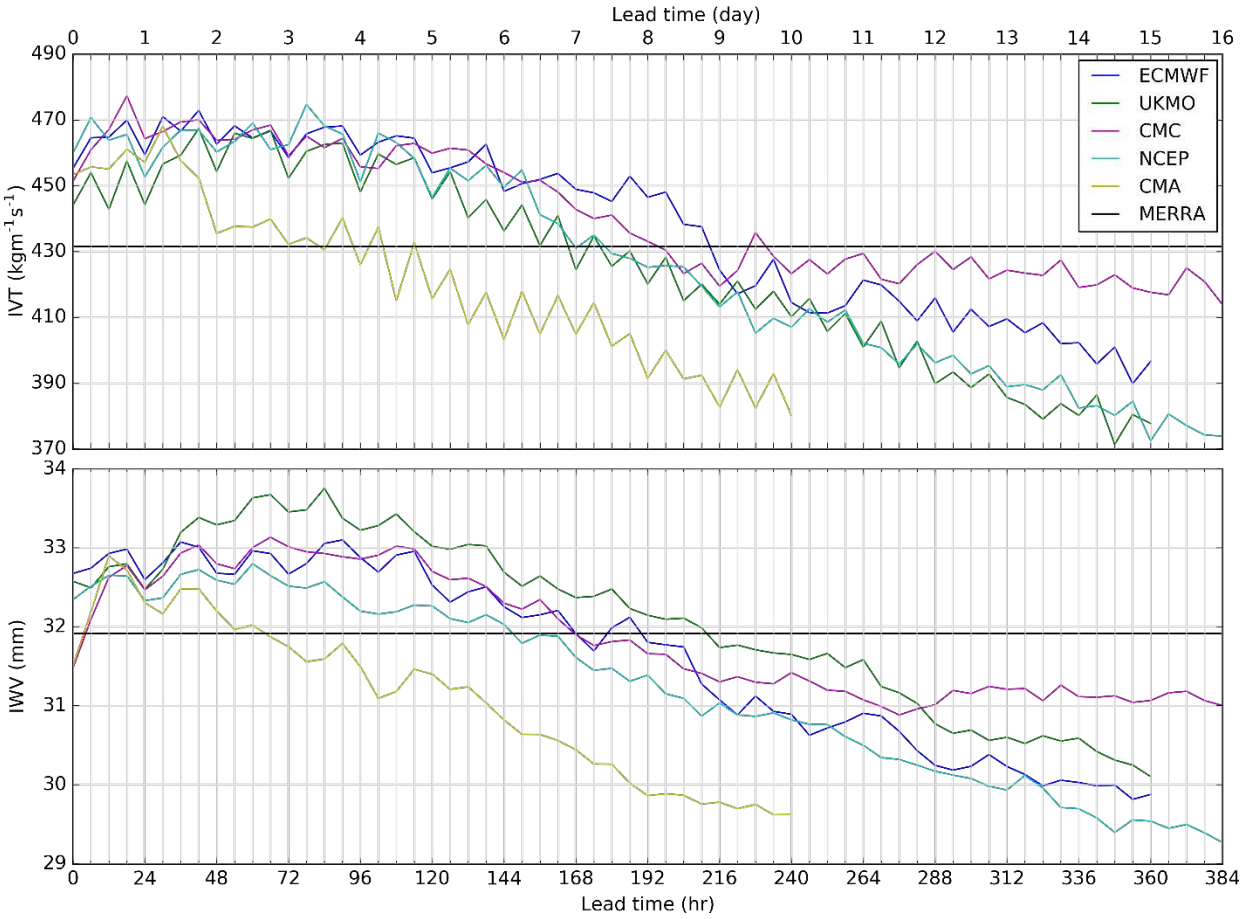

FIG. 6.2: IVT (top panel) and IWV (bottom panel) threshold variation with lead time for all the models and MERRA.

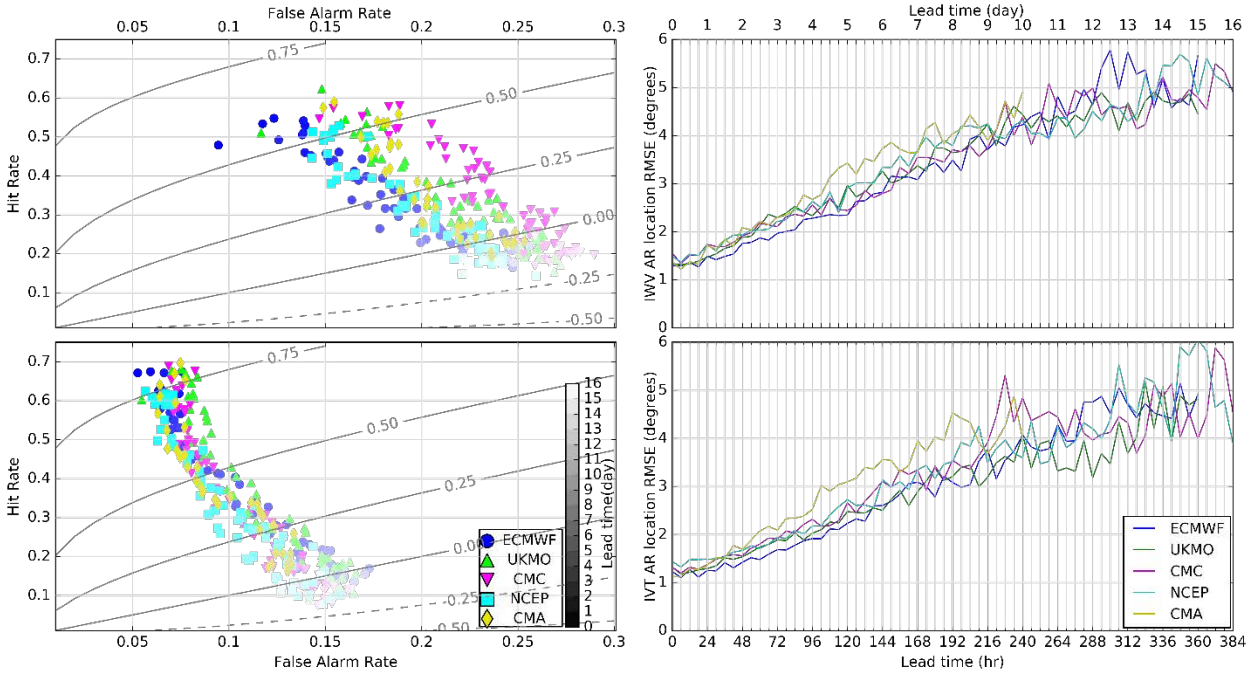

FIG. 6.3: Verification results based on IWV (top panels) and IVT (bottom panels). The left panels are the ROCs, while the right panels show the location errors. The identification is based on the lead-dependent thresholds in Figure 6.2.

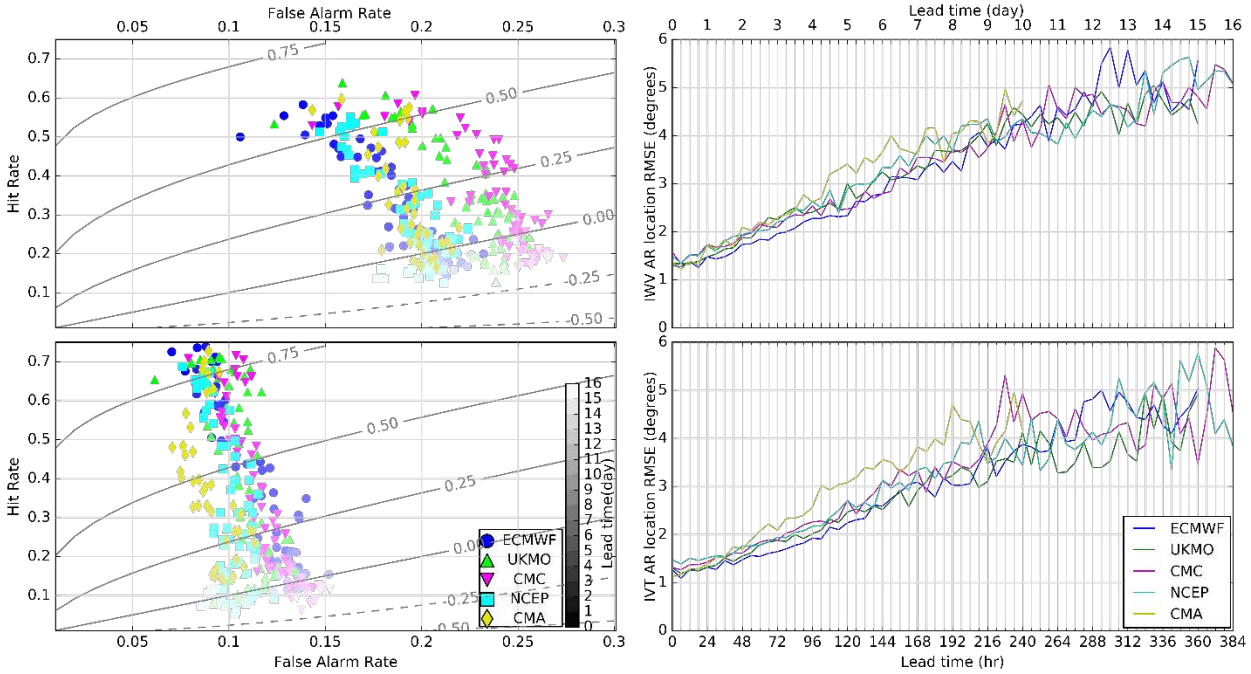

FIG. 6.4: Same as Figure 6.3 but using the MERRA threshold to identify the ARs for all the models and lead times.

CHAPTER 7

CONCLUSIONS

Atmospheric rivers (ARs) are long and narrow river-like features in the lower troposphere that carry most of the atmospheric water vapor fluxes from the tropics to the midlatitudes. While much of the research related to these storms has focused on the U.S. West Coast, little is known about their hydrometeorological effects over the central United States. This thesis fills this gap by providing detailed understanding of the AR climatology and their impacts on the hydrology of the central United States. Below, I highlight the main findings from the thesis.

The study of three ARs during the Iowa Flood Studies campaign (IFloodS; April-June 2013) provided many insights regarding the atmospheric mechanisms associated with these storms. The atmospheric pressure patterns during the three ARs depicted a subtropical ridge over the western North Atlantic Ocean accompanied by a lee trough over the Great Plains. This pressure pattern is conducive to the advection of water vapor from the Gulf of Mexico and the surrounding oceanic regions into the central United States. Lagrangian trajectory analysis of the AR air parcels advancing over the central United States showed that the sources of water vapor within these storms were located in the tropical and subtropical oceanic regions, and some additional water vapor was added by the inland evaporation along the AR trajectories. In terms of hydrologic impacts, unstable atmospheric conditions resulted in intense precipitation along the AR major axis, defined by the locations where the vapor transport is the highest. Moreover, the most intense precipitation occurs within the first 150km around the major axis, and it decreases as we move away from the major axis.

The follow-up work using ARs identified over a longer period of 12 years and based on precipitation estimates from remote-sensing based products corroborated these results. I found that the vapor transport and the associated rainfall within the first 150km region is higher than in the surrounding regions, with the largest values in the mid-latitude band 32ºN–36ºN; in this band, rainfall intensity has a pronounced positive relationship with the magnitude of the water vapor transport. Further, I observed that duration (or persistence)

of ARs is an important factor that governs the total rainfall during these storms. Rainfall intensity is smaller during the first 18 hours of AR conditions, followed by a consistent increase in precipitation intensity with duration—the intensity does not decrease until the AR conditions are over. This suggests that it may be reasonable to consider only storms that satisfy the 18-hour persistence criteria when focusing on hydrologic impacts over the central United States. Furthermore, it is imperative to understand the atmospheric mechanisms related to the long-lived ARs, as these are the ones that are more likely to cause persistent heavy rainfall and flooding.

Previous studies found significant diurnal variations in extreme precipitation events during the warm season over the central United States. I did not observe such characteristic in AR-related rainfall, likely because most of these storms occur in cold seasons (i.e., winter and spring), and AR-related rainfall is mechanistically different from summer extreme rainfall.

By focusing on several different reanalysis products to build a long-term AR climatology, I found that there are large seasonal differences in the occurrence of these events, with higher frequencies in winter and spring and relatively rare occurrences in the summer. On average, 26 ARs occur every year over the central United States. Comparing different reanalysis products, those with the higher spatial resolution were also the ones with the highest AR frequency and duration. In all the products, most of the storms were shorter than three days but longer lasting ones were also observed. The investigation of the two longest lasting ARs showed that they are associated with planetary longwave patterns in the northern hemisphere that are known to cause severe weather phenomena over many regions.

The AR effects on precipitation varies with location and season and, on average, about 30% of the annual precipitation over the central United States is associated with these storms. During the winter, areas along the extratropical cyclone storm track receive the largest contributions, while the smallest effects are in the summer. When we consider the impact of ARs on precipitation extremes, their contribution is even higher, exceeding 60% on an annual scale at some locations. The AR contribution to winter extreme precipitation is larger than 70% over a large part of the central United States. Higher spatial resolution reanalysis products show larger contributions than the lower resolution ones.

Considering annual maximum and POT floods, I found that ARs have a large impact at many long-term stream gaging stations; this is especially true in winter and spring, when more than 90% of these flood events are tied to the occurrence of ARs at several locations.

By visually examining the atmospheric pressure patterns during these storms, I find there is a resemblance with the patterns of large-scale atmospheric modes (PNA, NAO, and AO). Further investigation revealed that the resemblance is the most prominent in winter, hence the frequency of ARs can be related to the magnitudes of PNA and AO. These results are used to develop Bayesian hierarchical models in which PNA and AO magnitudes are used to describe winter AR frequency; in addition, the AR frequency itself is used to describe the frequency of heavy precipitation events in winter at a large number of rain gauges across the central United States. All the models in which PNA and AO or ARs are included as predictors performed better than the baseline model that did not have an explanatory variable. The best performance in both calibration and prediction periods was achieved by the model that involved a direct relationship between heavy precipitation and the frequency of ARs. The results corroborated my viewpoint that the magnitudes of PNA and AO has a direct impact on the frequency of ARs, and ARs in turn have a direct impact on extreme precipitation events.

Over a large area of the central United States, smaller PNA values have an increasing effect on the frequency of ARs, more so at stations located along the AR storm track: here a unit decrease in PNA can be expected to increase the frequency of ARs by more than 50%. Decreasing AO, on the other hand, is associated with a decrease in the frequency of these storms, albeit the effect is smaller than what is observed for PNA. The effect of ARs on heavy precipitation is almost always positive, and the occurrence of an additional AR can be expected to increase the frequency of heavy precipitation by about 10% at many stations. These modeling results suggest a promising future for the application of the low-dimensional atmospheric modes and ARs in predicting the frequency of extreme events at a seasonal scale.

The final chapter of my thesis focused on the verification of the occurrence and location of ARs from numerical weather prediction (NWP) models that provide forecasts up to a lead-time of 15 days. While an obvious ranking of these models is difficult based on their skill in forecasting ARs, all the models performed reasonably well at short lead-times of

up to seven days. The skill, however, decreased as the lead-time increased further, and after a lead-time of 10 days, a random forecasting system could possibly show better performance than the NWP models.

REFERENCES

AghaKouchak, A., A. Behrangi, S. Sorooshian, K. Hsu, and E. Amitai, 2011: Evaluation of satellite-retrieved extreme precipitation rates across the central United States. *Journal of Geophysical Research: Atmospheres*, **116,** n/a-n/a.

Akaike, H., 1974: A new look at the statistical model identification. *IEEE Transactions on Automatic Control*, **19,** 716-723.

Arritt, R. W., T. D. Rink, M. Segal, D. P. Todey, C. A. Clark, M. J. Mitchell, and K. M. Labas, 1997: The Great Plains Low-Level Jet during the Warm Season of 1993. *Monthly Weather Review*, **125,** 2176-2192.

Aryal, S. K., B. C. Bates, E. P. Campbell, Y. Li, M. J. Palmer, and N. R. Viney, 2009: Characterizing and Modeling Temporal and Spatial Trends in Rainfall Extremes. *Journal of Hydrometeorology*, **10,** 241-253.

Bao, J. W., S. A. Michelson, P. J. Neiman, F. M. Ralph, and J. M. Wilczak, 2006: Interpretation of enhanced integrated water vapor bands associated with extratropical cyclones: their formation and connection to tropical moisture. *Monthly Weather Review*, **134,** 1063-1080.

Barnston, A. G., and R. E. Livezey, 1987: Classification, Seasonality and Persistence of Low-Frequency Atmospheric Circulation Patterns. *Monthly Weather Review*, **115,** 1083-1126.

Besag, J., 1974: Spatial Interaction and the Statistical Analysis of Lattice Systems. *Journal of the Royal Statistical Society, Series B*, **36** 192-236.

Bonner, W. D., 1968: Climatology of the low level jet. *Monthly Weather Review*, **96,** 833-850.

Bougeault, P., and Coauthors, 2010: The THORPEX Interactive Grand Global Ensemble. *Bulletin of the American Meteorological Society*, **91,** 1059-1072.

Brooks, S. P., and A. Gelman, 1998: General Methods for Monitoring Convergence of Iterative Simulations. *Journal of Computational and Graphical Statistics*, **7,** 434-455.

Brooks, S. P., and G. O. Roberts, 1998: Convergence assessment techniques for Markov chain Monte Carlo. *Statistics and Computing*, **8,** 319-335.

Browning, K. A., 1986: Conceptual models of precipitation systems. *Weather and Forecasting*, **1,** 23-41.

——, 1990: Organization of clouds and precipitation in extratropical cyclones. *Extratropical Cyclones: The Erik Palmén Memorial Volume***,** 129-153.

Browning, K. A., 1997: The dry intrusion perspective of extra-tropical cyclone development. *Meteorological Applications*, **4,** 317-324.

Browning, K. A., and C. W. Pardoe, 1973: Structure of low-level jet streams ahead of mid-latitude cold fronts. *Quarterly Journal of the Royal Meteorological Society*, **99,** 619-638.

Budikova, D., J. S. M. Coleman, S. A. Strope, and A. Austin, 2010: Hydroclimatology of the 2008 Midwest floods. *Water Resources Research*, **46,** W12524.

Cai, Y., C. Jin, A. Wang, D. Guan, J. Wu, F. Yuan, and L. Xu, 2015: Spatio-Temporal Analysis of the Accuracy of Tropical Multisatellite Precipitation Analysis 3B42 Precipitation Data in Mid-High Latitudes of China. *PLoS ONE*, **10,** e0120026.

Carlson, T. N., 1980: Airflow through midlatitude cyclones and the comma cloud pattern. *Monthly Weather Review*, **108,** 1498-1509.

Catto, J. L., L. C. Shaffrey, and K. I. Hodges, 2009: Can Climate Models Capture the Structure of Extratropical Cyclones? *Journal of Climate*, **23,** 1621-1635.
Chen, S., and Coauthors, 2013: Evaluation of the successive V6 and V7 TRMM multisatellite precipitation analysis over the Continental United States. *Water Resources Research*, **49,** 8174-8186.
Coleman, J. S. M., and D. Budikova, 2010: Atmospheric aspects of the 2008 Midwest floods: a repeat of 1993? *International Journal of Climatology*, **30,** 1645-1667.
Compo, G. P., and Coauthors, 2011: The Twentieth Century Reanalysis Project. *Quarterly Journal of the Royal Meteorological Society*, **137,** 1-28.
Cooley, D., D. Nychka, and P. Naveau, 2007: Bayesian Spatial Modeling of Extreme Precipitation Return Levels. *Journal of the American Statistical Association*, **102,** 824-840.
Cowles, M. K., and B. P. Carlin, 1996: Markov Chain Monte Carlo Convergence Diagnostics: A Comparative Review. *Journal of the American Statistical Association*, **91,** 883-904.
Dacre, H. F., P. A. Clark, O. Martinez-Alvarado, M. A. Stringer, and D. A. Lavers, 2015: How do Atmospheric Rivers form? *Bulletin of the American Meteorological Society*, **96,** 1243-1255.
Dai, A., F. Giorgi, and K. E. Trenberth, 1999: Observed and model-simulated diurnal cycles of precipitation over the contiguous United States. *Journal of Geophysical Research: Atmospheres*, **104,** 6377-6402.
Dee, D. P., and Coauthors, 2011: The ERA-Interim reanalysis: Configuration and performance of the data assimilation system. *Quarterly Journal of the Royal Meteorological Society*, **137,** 553-597.
Derin, Y., and K. K. Yilmaz, 2014: Evaluation of Multiple Satellite-Based Precipitation Products over Complex Topography. *Journal of Hydrometeorology*, **15,** 1498-1516.
Dettinger, M. D., 2013: Atmospheric rivers as drought busters on the U.S. West Coast. *Journal of Hydrometeorology*, **14,** 1721-1732.
Dettinger, M. D., F. M. Ralph, T. Das, P. J. Neiman, and D. R. Cayan, 2011: Atmospheric rivers, floods and the water resources of California. *Water*, **3,** 445-478.
Dirmeyer, P. A., and J. L. Kinter, 2009: The "Maya Express": Floods in the U.S. Midwest. *Eos, Transactions American Geophysical Union*, **90,** 101-102.
——, 2010: Floods over the U.S. Midwest: A regional water cycle perspective. *Journal of Hydrometeorology*, **11,** 1172-1181.
Dirmeyer, P. A., J. Wei, M. G. Bosilovich, and D. M. Mocko, 2014: Comparing evaporative sources of terrestrial precipitation and their extremes in MERRA using relative entropy. *Journal of Hydrometeorology*, **15,** 102-116.
Draxler, R. R., and G. D. Rolph, cited 2015: HYSPLIT: Hybrid Single- Particle Lagrangian Integrated Trajectory Model. NOAA ARLREADY. [Available online at http://www.arl.noaa.gov/HYSPLIT.php. Accessed on 07-15-2015]
Ferguson, C. R., and G. Villarini, 2012: Detecting inhomogeneities in the Twentieth Century Reanalysis over the central United States. *Journal of Geophysical Research: Atmospheres*, **117,** n/a-n/a.
Ferro, C. A. T., and D. B. Stephenson, 2011: Extremal Dependence Indices: Improved Verification Measures for Deterministic Forecasts of Rare Binary Events. *Weather and Forecasting*, **26,** 699-713.

Gandin, L. S., and A. H. Murphy, 1992: Equitable Skill Scores for Categorical Forecasts. *Monthly Weather Review*, **120,** 361-370.
Gelman, A., and D. B. Rubin, 1992: Inference from Iterative Simulation Using Multiple Sequences**,** 457-472.
Gelman, A., and J. Hill, 2007: *Data analysis using regression and multilevel/hierarchical models.* Cambridge University Pressm New York.
Geweke, J., 1992: Evaluating the accuracy of sampling-based approaches to calculating posterior moments. *Bayesian Statistics 4*, J. M. Bernardo, J. Berger, A. P. Dawid, and J. F. M. Smith, Eds., Oxford University Press, 169-193.
Gneiting, T., and A. E. Raftery, 2007: Strictly Proper Scoring Rules, Prediction, and Estimation. *Journal of the American Statistical Association*, **102,** 359-378.
Gregersen, I. B., H. Madsen, D. Rosbjerg, and K. Arnbjerg-Nielsen, 2013: A spatial and nonstationary model for the frequency of extreme rainfall events. *Water Resources Research*, **49,** 127-136.
Guan, B., N. P. Molotch, D. E. Waliser, E. J. Fetzer, and P. J. Neiman, 2010: Extreme snowfall events linked to atmospheric rivers and surface air temperature via satellite measurements. *Geophysical Research Letters*, **37,** n/a-n/a.
Harding, K. J., and P. K. Snyder, 2015: The relationship between the Pacific–North American Teleconnection Pattern, the Great Plains Low-Level Jet, and North central U.S. heavy rainfall events. *Journal of Climate*, **28,** 6729-6742.
Harrold, T. W., 1973: Mechanisms influencing the distribution of precipitation within baroclinic disturbances. *Quarterly Journal of the Royal Meteorological Society*, **99,** 232-251.
Higgins, R. W., W. Shi, E. Yarosh, and R. J. Joyce, 2000: Improved United States precipitation quality control system and analysis.
Hou, D., and Coauthors, 2014: Climatology-Calibrated Precipitation Analysis at Fine Scales: Statistical Adjustment of Stage IV toward CPC Gauge-Based Analysis. *Journal of Hydrometeorology*, **15,** 2542-2557.
Houze, R. A., 2014: *Cloud dynamics.* 2 ed. Vol. 104, Academic Press/Elsevier B.V.
Huffman, G. J., and Coauthors, 2007: The TRMM Multisatellite Precipitation Analysis (TMPA): Quasi-Global, Multiyear, Combined-Sensor Precipitation Estimates at Fine Scales. *Journal of Hydrometeorology*, **8,** 38-55.
Hughes, M., K. M. Mahoney, P. J. Neiman, B. J. Moore, M. Alexander, and F. M. Ralph, 2014: The Landfall and Inland Penetration of a Flood-Producing Atmospheric River in Arizona. Part II: Sensitivity of Modeled Precipitation to Terrain Height and Atmospheric River Orientation. *Journal of Hydrometeorology*, **15,** 1954-1974.
Jolliffe, I. T., 2008: The impenetrable hedge: a note on propriety, equitability and consistency. *Meteorological Applications*, **15,** 25-29.
Jolliffe, I. T., and D. B. Stephenson, 2012: *Forecast Verification: A Practitioner's Guide in Atmospheric Science.* 2nd ed. John Wiley, Chichester, U. K.
Joyce, R. J., J. E. Janowiak, P. A. Arkin, and P. Xie, 2004: CMORPH: A method that produces global precipitation estimates from passive microwave and infrared data at high spatial and temporal resolution. *Journal of Hydrometeorology*, **5,** 487-503.
Kaiser, H. F., 1958: The varimax criterion for analytic rotation in factor analysis. *Psychometrika*, **23,** 187-200.

——, 1959: Computer Program for Varimax Rotation in Factor Analysis. *Educational and Psychological Measurement*, **19,** 413-420.
Kalnay, E., and Coauthors, 1996: The NCEP/NCAR 40-Year Reanalysis Project. *Bulletin of the American Meteorological Society*, **77,** 437-471.
Kanamitsu, M., W. Ebisuzaki, J. Woollen, S.-K. Yang, J. J. Hnilo, M. Fiorino, and G. L. Potter, 2002: NCEP–DOE AMIP-II Reanalysis (R-2). *Bulletin of the American Meteorological Society*, **83,** 1631-1643.
Knippertz, P., and H. Wernli, 2010: A lagrangian climatology of tropical moisture exports to the Northern hemispheric extratropics. *Journal of Climate*, **23,** 987-1003.
Knippertz, P., H. Wernli, and G. Gläser, 2013: A global climatology of tropical moisture exports. *Journal of Climate*, **26,** 3031-3045.
Kobayashi, S., and Coauthors, 2015: The JRA-55 Reanalysis: General specifications and basic characteristics. *Journal of the Meteorological Society of Japan. Ser. II*, **93,** 5-48.
Kuhnel, I., 1989: Tropical-extratropical cloudband climatology based on satellite data. *International Journal of Climatology*, **9,** 441-463.
Kunkel, K. E., S. A. Changnon, and J. R. Angel, 1994: Climatic aspects of the 1993 upper Mississippi river basin flood. *Bulletin of the American Meteorological Society*, **75,** 811-822.
Kunkel, K. E., D. R. Easterling, D. A. R. Kristovich, B. Gleason, L. Stoecker, and R. Smith, 2012: Meteorological causes of the secular variations in observed extreme precipitation events for the conterminous United States. *Journal of Hydrometeorology*, **13,** 1131-1141.
Lavers, D. A., and G. Villarini, 2013a: The nexus between atmospheric rivers and extreme precipitation across Europe. *Geophysical Research Letters*, **40,** 3259-3264.
——, 2013b: Atmospheric rivers and flooding over the central United States. *Journal of Climate*, **26,** 7829-7836.
——, 2015a: The contribution of atmospheric rivers to precipitation in Europe and the United States. *Journal of Hydrology*, **522,** 382-390.
——, 2015b: The relationship between daily European precipitation and measures of atmospheric water vapour transport. *International Journal of Climatology*, **35,** 2187-2192.
Lavers, D. A., G. Villarini, R. P. Allan, E. F. Wood, and A. J. Wade, 2012: The detection of atmospheric rivers in atmospheric reanalyses and their links to British winter floods and the large-scale climatic circulation. *Journal of Geophysical Research: Atmospheres*, **117,** D20106.
Lavers, D. A., F. M. Ralph, D. E. Waliser, A. Gershunov, and M. D. Dettinger, 2015: Climate change intensification of horizontal water vapor transport in CMIP5. *Geophysical Research Letters*, **42,** 5617-5625.
Lavers, D. A., R. P. Allan, E. F. Wood, G. Villarini, D. J. Brayshaw, and A. J. Wade, 2011: Winter floods in Britain are connected to atmospheric rivers. *Geophysical Research Letters*, **38,** L23803.
Leung, L. R., and Y. Qian, 2009: Atmospheric rivers induced heavy precipitation and flooding in the western U.S. simulated by the WRF regional climate model. *Geophysical Research Letters*, **36,** n/a-n/a.
Li, L., W. Li, and Y. Kushnir, 2012: Variation of the North Atlantic subtropical high western ridge and its implication to Southeastern US summer precipitation. *Climate Dynamics*, **39,** 1401-1412.

Li, W., L. Li, R. Fu, Y. Deng, and H. Wang, 2010: Changes to the North Atlantic Subtropical High and Its Role in the Intensification of Summer Rainfall Variability in the Southeastern United States. *Journal of Climate*, **24,** 1499-1506.
Lima, C. H. R., U. Lall, T. J. Troy, and N. Devineni, 2015: A climate informed model for nonstationary flood risk prediction: Application to Negro River at Manaus, Amazonia. *Journal of Hydrology*, **522,** 594-602.
Lin, Y., and K. E. Mitchell, 2005: The NCEP Stage II/IV hourly precipitation analyses: development and applications. *American Meteorological Society*, San Diego, CA, Citeseer, Paper 1.2.
Lombard, F., 1987: Rank tests for changepoint problems. *Biometrika*, **74,** 615-624.
Lunn, D., C. Jackson, N. Best, A. Thomas, and D. Spiegelhalter, 2012: *The BUGS book: A practical introduction to Bayesian analysis.* CRC press.
Maddox, R. A., C. F. Chappell, and L. R. Hoxit, 1979: Synoptic and Meso-α scale aspects of flash flood events. *Bulletin of the American Meteorological Society*, **60,** 115-123.
Mahoney, K., and Coauthors, 2016: Understanding the Role of Atmospheric Rivers in Heavy Precipitation in the Southeast United States. *Monthly Weather Review*, **144,** 1617-1632.
Mallakpour, I., and G. Villarini, 2015: The changing nature of flooding across the central United States. *Nature Clim. Change*, **5,** 250-254.
——, 2016a: Analysis of changes in the magnitude, frequency, and seasonality of heavy precipitation over the contiguous USA. *Theoretical and Applied Climatology***,** 1-19.
——, 2016b: Investigating the relationship between the frequency of flooding over the central United States and large-scale climate. *submitted to Advances in Water Resources*.
Mardia, K. V., 1988: Multi-dimensional multivariate Gaussian Markov random fields with application to image processing. *Journal of Multivariate Analysis*, **24,** 265-284.
McGuirk, J. P., A. H. Thompson, and N. R. Smith, 1987: Moisture bursts over the tropical Pacific ocean. *Monthly Weather Review*, **115,** 787-798.
McMurdie, W. L., and R. A. Houze, 2006: 8 - Weather Systems. *Atmospheric Science (Second Edition)*, J. M. Wallace, and P. V. Hobbs, Eds., Academic Press, 313-373.
Menne, M. J., I. Durre, R. S. Vose, B. E. Gleason, and T. G. Houston, 2012: An Overview of the Global Historical Climatology Network-Daily Database. *Journal of Atmospheric and Oceanic Technology*, **29,** 897-910.
Mitchell, M. J., R. W. Arritt, and K. Labas, 1995: A Climatology of the Warm Season Great Plains Low-Level Jet Using Wind Profiler Observations. *Weather and Forecasting*, **10,** 576-591.
Mo, K. C., J. N. Paegle, and R. W. Higgins, 1997: Atmospheric processes associated with summer floods and droughts in the central United States. *Journal of Climate*, **10,** 3028-3046.
Moore, B. J., P. J. Neiman, F. M. Ralph, and F. E. Barthold, 2012: Physical processes associated with heavy flooding rainfall in Nashville, Tennessee, and vicinity during 1–2 May 2010: The role of an atmospheric river and mesoscale convective systems*. *Monthly Weather Review*, **140,** 358-378.
Nakamura, J., U. Lall, Y. Kushnir, A. W. Robertson, and R. Seager, 2012: Dynamical structure of extreme floods in the U.S. Midwest and the United Kingdom. *Journal of Hydrometeorology*, **14,** 485-504.

Nayak, M. A., and G. Villarini, 2016: Evaluation of the capability of the Lombard test in detecting abrupt changes in variance. *Journal of Hydrology*, **534,** 451-465.
Neiman, P. J., F. M. Ralph, G. A. Wick, J. D. Lundquist, and M. D. Dettinger, 2008: Meteorological characteristics and overland precipitation impacts of atmospheric rivers affecting the west coast of North America based on eight years of SSM/I satellite observations. *Journal of Hydrometeorology*, **9,** 22-47.
Neiman, P. J., L. J. Schick, F. M. Ralph, M. Hughes, and G. A. Wick, 2011: Flooding in Western Washington: The connection to atmospheric rivers*. *Journal of Hydrometeorology*, **12,** 1337-1358.
Neiman, P. J., G. A. Wick, B. J. Moore, F. M. Ralph, J. R. Spackman, and B. Ward, 2014: An Airborne Study of an Atmospheric River over the Subtropical Pacific during WISPAR: Dropsonde Budget-Box Diagnostics and Precipitation Impacts in Hawaii. *Monthly Weather Review*, **142,** 3199-3223.
Neiman, P. J., F. M. Ralph, B. J. Moore, M. Hughes, K. M. Mahoney, J. M. Cordeira, and M. D. Dettinger, 2013: The Landfall and Inland Penetration of a Flood-Producing Atmospheric River in Arizona. Part I: Observed Synoptic-Scale, Orographic, and Hydrometeorological Characteristics. *Journal of Hydrometeorology*, **14,** 460-484.
Newell, R. E., and Y. Zhu, 1994: Tropospheric rivers: A one-year record and a possible application to ice core data. *Geophysical Research Letters*, **21,** 113-116.
Newell, R. E., N. E. Newell, Y. Zhu, and C. Scott, 1992: Tropospheric rivers? – A pilot study. *Geophysical Research Letters*, **19,** 2401-2404.
Petoukhov, V., S. Rahmstorf, S. Petri, and H. J. Schellnhuber, 2013: Quasiresonant amplification of planetary waves and recent Northern Hemisphere weather extremes. *Proceedings of the National Academy of Sciences*, **110,** 5336-5341.
Plummer, M., N. Best, K. Cowles, and K. Vines, 2006: CODA: Convergence diagnosis and output analysis for MCMC. *R news*, **6,** 7-11.
Portis, D. H., J. E. Walsh, M. El Hamly, and P. J. Lamb, 2001: Seasonality of the North Atlantic Oscillation. *Journal of Climate*, **14,** 2069-2078.
Prat, O. P., and B. R. Nelson, 2015: Evaluation of precipitation estimates over CONUS derived from satellite, radar, and rain gauge data sets at daily to annual scales (2002–2012). *Hydrol. Earth Syst. Sci.*, **19,** 2037-2056.
Puca, S., and Coauthors, 2014: The validation service of the hydrological SAF geostationary and polar satellite precipitation products. *Nat. Hazards Earth Syst. Sci.*, **14,** 871-889.
Raftery, A., and S. Lewis, 1992: How many iterations in the Gibbs sampler. *In Bayesian Statistics 4*, 763-773.
Ralph, F. M., and M. D. Dettinger, 2012: Historical and national perspectives on extreme West Coast precipitation associated with atmospheric rivers during December 2010. *Bulletin of the American Meteorological Society*, **93,** 783-790.
Ralph, F. M., P. J. Neiman, and G. A. Wick, 2004: Satellite and CALJET aircraft observations of atmospheric rivers over the eastern North Pacific ocean during the winter of 1997/98. *Monthly Weather Review*, **132,** 1721-1745.
Ralph, F. M., T. Coleman, P. J. Neiman, R. J. Zamora, and M. D. Dettinger, 2013: Observed impacts of duration and seasonality of stmospheric-river landfalls on soil moisture and runoff in coastal Northern California. *Journal of Hydrometeorology*, **14,** 443-459.

Ralph, M. F., P. J. Neiman, G. Wick, A., S. I. Gutman, M. D. Dettinger, D. R. Cayan, and A. B. White, 2006: Flooding on California's Russian River: Role of atmospheric rivers. *Geophysical Research Letters*, **33,** L13801.
Renard, B., and U. Lall, 2014: Regional frequency analysis conditioned on large-scale atmospheric or oceanic fields. *Water Resources Research*, **50,** 9536-9554.
Rienecker, M. M., and Coauthors, 2011: MERRA: NASA's Modern-Era Retrospective Analysis for Research and Applications. *Journal of Climate*, **24,** 3624-3648.
Rudolf, B., 1993: *Management and analysis of precipitation data on a routine basis.* Global Precipitation Climatology Centre.
Rutz, J. J., W. J. Steenburgh, and F. M. Ralph, 2014: Climatological characteristics of atmospheric rivers and their inland penetration over the western United States. *Monthly Weather Review*, **142,** 905-921.
——, 2015: The Inland Penetration of Atmospheric Rivers over Western North America: A Lagrangian Analysis. *Monthly Weather Review*, **143,** 1924-1944.
Schultz, D. M., 2001: Reexamining the Cold Conveyor Belt. *Monthly Weather Review*, **129,** 2205-2225.
Smith, J. A., and M. L. Baeck, 2015: "Prophetic vision, vivid imagination": The 1927 Mississippi River flood. *Water Resources Research*, **51,** 9964-9994.
Smith, J. A., M. L. Baeck, G. Villarini, D. B. Wright, and W. Krajewski, 2013: Extreme Flood Response: The June 2008 Flooding in Iowa. *Journal of Hydrometeorology*, **14,** 1810-1825.
Sorooshian, S., K.-L. Hsu, X. Gao, H. V. Gupta, B. Imam, and D. Braithwaite, 2000: Evaluation of PERSIANN system satellite–based estimates of tropical rainfall. *Bulletin of the American Meteorological Society*, **81,** 2035-2046.
Spiegelhalter, D., A. Thomas, N. Best, and D. Lunn, 2007: OpenBUGS user manual, version 3.0. 2. *MRC Biostatistics Unit, Cambridge*.
Spiegelhalter, D. J., N. G. Best, B. P. Carlin, and A. Van Der Linde, 2002: Bayesian measures of model complexity and fit. *Journal of the Royal Statistical Society: Series B (Statistical Methodology)*, **64,** 583-639.
Steinschneider, S., and U. Lall, 2015a: A hierarchical Bayesian regional model for nonstationary precipitation extremes in Northern California conditioned on tropical moisture exports. *Water Resources Research*, **51,** 1472-1492.
——, 2015b: Daily Precipitation and Tropical Moisture Exports across the Eastern United States: An Application of Archetypal Analysis to Identify Spatiotemporal Structure. *Journal of Climate*, **28,** 8585-8602.
——, 2016: Spatiotemporal structure of precipitation related to tropical moisture exports over the eastern United States and its relation to climate teleconnections. *Journal of Hydrometeorology*, **17,** 897-913.
Stephenson, D. B., B. Casati, C. A. T. Ferro, and C. A. Wilson, 2008: The extreme dependency score: a non-vanishing measure for forecasts of rare events. *Meteorological Applications*, **15,** 41-50.
Stevenson, S. N., and R. S. Schumacher, 2014: A 10-year survey of extreme rainfall events in the central and eastern United States using gridded multisensor precipitation analyses. *Monthly Weather Review*, **142,** 3147-3162.

Stohl, A., C. Forster, and H. Sodemann, 2008: Remote sources of water vapor forming precipitation on the Norwegian west coast at 60°N–a tale of hurricanes and an atmospheric river. *Journal of Geophysical Research: Atmospheres*, **113,** n/a-n/a.
Sturtz, S., U. Ligges, and A. Gelman, 2005: R2WinBUGS: a package for running WinBUGS from R. *Journal of Statistical software*, **12,** 1-16.
Sun, X., M. Thyer, B. Renard, and M. Lang, 2014: A general regional frequency analysis framework for quantifying local-scale climate effects: A case study of ENSO effects on Southeast Queensland rainfall. *Journal of Hydrology*, **512,** 53-68.
Sun, X., U. Lall, B. Merz, and N. V. Dung, 2015: Hierarchical Bayesian clustering for nonstationary flood frequency analysis: Application to trends of annual maximum flow in Germany. *Water Resources Research*, **51,** 6586-6601.
Team, R. C., 2013: R: A language and environment for statistical computing.
Thompson, D. W. J., and J. M. Wallace, 1998: The Arctic oscillation signature in the wintertime geopotential height and temperature fields. *Geophysical Research Letters*, **25,** 1297-1300.
——, 2000: Annular Modes in the Extratropical Circulation. Part I: Month-to-Month Variability. *Journal of Climate*, **13,** 1000-1016.
Viale, M., and M. N. Nuñez, 2011: Climatology of winter orographic precipitation over the subtropical central Andes and associated synoptic and regional characteristics. *Journal of Hydrometeorology*, **12,** 481-507.
Vila, D. A., L. G. G. de Goncalves, D. L. Toll, and J. R. Rozante, 2009: Statistical Evaluation of Combined Daily Gauge Observations and Rainfall Satellite Estimates over Continental South America. *Journal of Hydrometeorology*, **10,** 533-543.
Villarini, G., 2016: On the seasonality of flooding across the continental United States. *Advances in Water Resources*, **87,** 80-91.
Villarini, G., and W. F. Krajewski, 2007: Evaluation of the research version TMPA three-hourly 0.25° × 0.25° rainfall estimates over Oklahoma. *Geophysical Research Letters*, **34,** n/a-n/a.
Villarini, G., and J. A. Smith, 2010: Flood peak distributions for the eastern United States. *Water Resources Research*, **46,** n/a-n/a.
Villarini, G., W. F. Krajewski, and J. A. Smith, 2009: New paradigm for statistical validation of satellite precipitation estimates: Application to a large sample of the TMPA 0.25° 3-hourly estimates over Oklahoma. *Journal of Geophysical Research: Atmospheres*, **114,** n/a-n/a.
Villarini, G., J. A. Smith, M. L. Baeck, and W. F. Krajewski, 2011: Examining Flood Frequency Distributions in the Midwest U.S. *JAWRA Journal of the American Water Resources Association*, **47,** 447-463.
Wallace, J. M., 1975: Diurnal Variations in Precipitation and Thunderstorm Frequency over the Conterminous United States. *Monthly Weather Review*, **103,** 406-419.
Wallace, J. M., and D. S. Gutzler, 1981: Teleconnections in the geopotential height field during the Northern hemisphere winter. *Monthly Weather Review*, **109,** 784-812.
Waller, L. A., B. P. Carlin, H. Xia, and A. E. Gelfand, 1997: Hierarchical Spatio-Temporal Mapping of Disease Rates. *Journal of the American Statistical Association*, **92,** 607-617.
Weigel, A. P., M. A. Liniger, and C. Appenzeller, 2007: The Discrete Brier and Ranked Probability Skill Scores. *Monthly Weather Review*, **135,** 118-124.

Wick, G. A., P. J. Neiman, F. M. Ralph, and T. M. Hamill, 2013: Evaluation of Forecasts of the Water Vapor Signature of Atmospheric Rivers in Operational Numerical Weather Prediction Models. *Weather and Forecasting*, **28,** 1337-1352.
Wilks, D. S., 2011: *Statistical methods in the atmospheric sciences.* 3rd ed. Vol. 100, Academic press.
Xie, P., B. Rudolf, U. Schneider, and P. A. Arkin, 1996: Gauge-based monthly analysis of global land precipitation from 1971 to 1994. *Journal of Geophysical Research: Atmospheres*, **101,** 19023-19034.
Zhang, Y., and Coauthors, 2015: Hydrometeorological Analysis and Remote Sensing of Extremes: Was the July 2012 Beijing Flood Event Detectable and Predictable by Global Satellite Observing and Global Weather Modeling Systems? *Journal of Hydrometeorology*, **16,** 381-395.
Zhu, Y., and R. E. Newell, 1994: Atmospheric rivers and bombs. *Geophysical Research Letters*, **21,** 1999-2002.
——, 1998: A proposed algorithm for moisture fluxes from atmospheric rivers. *Monthly Weather Review*, **126,** 725-735.